Variations in biological doses to cognitive brain structures following pediatric proton therapy by using different models for the relative biological effectiveness

Ole Marius Otterlei

Supervisors: Camilla Hanquist Stokkevåg, Kristian S. Ytre-Hauge, and Laura Toussaint

Master thesis in medical physics
Department of Physics and Technology
University of Bergen

November 2019

2019

Variations in biological doses to cognitive brain structures following pediatric proton therapy by using different models for the relative biological effectiveness

Ole Marius Otterlei

https://bora.uib.no/

Abstract

Purpose and objective: In clinical practice, a constant value of 1.1 is used for the relative biological effectiveness (RBE) of protons, whereas in reality, the RBE is known to vary with the physical dose level, tissue type and biological endpoint. In order to investigate the heterogeneity of biological doses to structures associated with cognition in pediatric brain tumor patients, we included a wide selection of published models accounting for variable RBE. We also aimed to identify the most suitable RBE models for this endpoint and patient group through a criteria-based approach, and further use the identified models to estimate risk of cognitive impairment.

Material and methods: Intensity modulated proton therapy (IMPT) treatment plans for ten anonymized pediatric patients with craniopharyngioma were re-calculated using using eleven published phenomenological models as well as two plan-based variable RBE models. Physical dose and linear energy transfer (LET) distributions were calculated on the planning Computed Tomography (CT) by using the FLUKA Monte Carlo code. Thirty brain structures associated with cognition (BSCs) were investigated in terms of RBE and dose/volume parameters associated with white matter damage (%V40Gy) and reduction of neural stem cell number (%V10Gy). The RBE models considered as most relevant for the studied endpoint were selected based on LET, tissue dependence and the number of data points used to fit the RBE models. The selected models were further used to estimate potential cognitive impairment, including change in intelligence quotient (IQ) and risk of memory impairment. To reflect the range of radiation fractionation sensitivity in the brain, $(\alpha/\beta)_x$ values of both 2 Gy and 3 Gy were applied for the tissue dependent models.

Results: Across all RBE models, wide variations in RBE were seen for the studied brain structures. In terms of model selection, the models by Rørvik et al., McNamara et al. and Jones et al. fulfilled the defined selection criteria. The median [and range] of the dose-weighted mean RBE (RBE_d) across all structures and models applied to one patient was 1.19 [0.81 – 2.61]. Across the full patient cohort, the model by Jones et al. estimated the highest median RBE_d of the selected set of models at 1.30 [1.15 – 3.31] across all structures, whereas the models by Rørvik et al. and McNamara et al. resulted in median values of 1.22 [1.12 – 2.46] and 1.23 [1.11 – 2.62] including both input parameters of $(\alpha/\beta)_x$. In terms of change in IQ score, the median

across all IQ models was -1.9 [-9.3, 0.0] for the model by Jones et al., whereas the models by Rørvik et al. and McNamara et al. resulted in median values of 1.8 [-9.9, 0] and -1.8 [-10, 0.0], respectively. With a constant RBE of 1.1, the median IQ score change was -1.6 [-9.5, 0.0].

Conclusion: There was a large and systematic model-dependent variation in RBE and dose/volume parameters across the cognitive structures, also reflected in the estimated cognitive impairment. Through the criteria-based method, it was possible to select a set of endpoint-specific models that may give a more precise estimate of relevant RBE-weighted dose ranges and potential cognitive impairment for this patient group.

Acknowledgments

I would like to express my very profound gratitude to my main supervisor, Camilla Hanquist Stokkevåg, for her patient guidance, encouragement and support throughout the entire project. Your help has been invaluable. Furthermore, I would like to thank the co-supervisors, Kristian S. Ytre-Hauge and Laura Toussaint. Thank you, Kristian, for helpful guidance throughout this project and for introducing me to the topic. Thank you, Laura, for all the feedback and for providing me with the treatment plans. In addition, I also wish to thank Sara Pilskog for valuable advice.

I would like to acknowledge the Ph.D. students at the University, Helge Henjum, Lars Fredrik Fjæra, Tordis Dahle and Eivind Rørvik, who always kept their door open and gladly helped whenever I asked for assistance. To my fellow students: Hanne, Alise, Michel, Håkon and Olve; thank you for our companionship during our five years at UiB.

A special thanks to my parents and my two sisters for the endless support. I am highly thankful for everything you have done for me. Last but not least, I would like to express my deepest gratitude to Cathrine. Thank you, Cathrine, for being so patient and encouraging for the last few months.

Contents

List of Figures

List of Tables

List of Abbreviations

BSC	**B**rain **S**tructure associated with **C**ognition
CNS	**C**entral **N**ervous **S**ystem
CT	**C**omputed **T**omography
CTV	**C**linical **T**arget **V**olume
DSB	**D**ouble **S**trand-**B**reak
DVH	**D**ose **V**olume **H**istogram
FSIQ	**F**ull-**S**cale **I**ntelligence **Q**uotient
GTV	**G**ross **T**umor **V**olume
ICRU	**I**nternational **C**ommission on **R**adiation **U**nits & Measurements
IMPT	**I**ntensity **M**odulated **P**roton **T**herapy
IM	**I**nternal **M**argin
IQ	**I**ntelligence **Q**uotient
ITV	**I**nternal **T**arget **V**olume
LET	**L**inear **E**nergy **T**ransfer
LQ	**L**inear **Q**uadratic
MC	**M**onte **C**arlo
MRI	**M**agnetic **R**esonance **I**maging
NTCP	**N**ormal **T**issue **C**omplication **P**robability
PET	**P**ositron **E**mission **T**omography
PTV	**P**lanning **T**arget **V**olume
RBE	**R**elative **B**iological **E**ffectiveness
TCP	**T**umor **C**ontrol **P**robability
TPS	**T**reatment **P**lanning **S**ystem
SOBP	**S**pread **O**ut **B**ragg **P**eak
SSB	**S**ingle-**S**trand **B**reak

1 Introduction

In 2018, more than 34 000 new cancer cases were reported in Norway [1]. In the case of pediatric patients, central nervous system (CNS) brain tumors account for one-fifth of cancer occurrences and are the most common solid tumor in children [2]. Of these occurrences, approximately 6 – 9% are craniopharyngiomas [3]. Craniopharyngioma is a benign tumor located in the central part of the brain in close proximity to critical structures. Craniopharyngioma patients are therefore often vulnerable to toxicity, including cognitive impairment, despite a survival rate exceeding 85 % [4, 5]. An average loss of 18 intelligence quotient (IQ) points have been found in pediatric patients with brain tumors receiving radiation therapy, which illustrates the risk of cognitive impairment [6]. Due to the increased ongoing brain development compared to adults, pediatrics are of particular risk of developing neurocognitive impairment following radiation therapy.

About 50 % of cancer patients will receive radiation therapy, either as a supplement to other treatment methods or as an independent treatment modality. Radiation therapy aims to deposit dose restricted to the tumor while sparing the surrounding healthy tissue. Protons in radiation therapy were first suggested by Robert Wilson in 1946 [7]. The rationale behind this suggestion was that protons deposit most of their energy at the end of their range, resulting in a sharp peak, known as the Bragg Peak. Compared to photons, protons result in better dose conformity with lower integral dose and no “exit” dose [8, 9]. Proton beam therapy may, therefore, better spare healthy tissues, including brain substructures associated with cognition (BSCs), potentially preserving cognitive function and IQ points [10]. Radiation therapy using photons is to date much more common than proton beam therapy; however, proton beam therapy is increasingly being used for treatment of craniopharyngiomas, and the clinical results are promising when compared with photons [11-14]. However, there are uncertainties regarding radiation therapy with protons. For instance, the relative biological effectiveness (RBE) of protons compared to photons is still, to a certain degree, unknown. In clinical practice, a constant RBE value of 1.1 is being used, although the RBE has been shown to vary with both biological and physical factors [15]. The enhanced linear energy transfer (LET) at the distal end of the beams is of particular clinical concern, as this may lead to elevated RBE in healthy brain tissue [16].

1.1 Objectives

The overall objective of this thesis was to evaluate how the RBE-weighted dose to brain structures associated with cognition differs when using a constant RBE of 1.1 and so-called variable RBE models. A recent study by Toussaint et al. demonstrated that cognitive functions might be better preserved with protons compared with photons for children with craniopharyngioma [13]. There have been several studies reporting less cognitive impairment following proton therapy treatment than photon therapy; however, most of these studies neglect the potential increased biological effectiveness of protons [11, 12]. The constant value of 1.1 used for the RBE of protons may lead to an under- or overestimation of the deposited dose, and therefore may influence the risk of side-effects.

Phenomenological and so-called plan-based variable proton RBE models have endeavored to account for the physical and biological variations in RBE estimation. None of the published models are to this day in clinical use; however, they might contribute to relevant material in clinical outcome interpretation [17, 18]. Recently, Rørvik et al. showed that both the input data and estimations varied considerably between the models, highlighting the complexity in interpretations of the RBE.

For this thesis, it was of interest to investigate a large number of BSCs. Most studies in the field of cognitive impairment in pediatric brain tumor patients have tended to focus on large brain structures and brain regions, such as the supratentorial brain or temporal lobes [10, 19-22]. However, recent research has suggested that smaller substructures may have a substantial impact on cognitive function outcomes following radiation therapy [23-25].

The overall goal of this thesis can be split into two separate aims, which are closely related. First, we aimed to identify a set of variable proton RBE models well suited for the patient group (pediatric craniopharyngiomas), combined with the specific endpoint (cognitive impairment). Secondly, we aimed to estimate the possible range of RBE-weighted doses, RBE, and dose/volume parameters to the BSCs, which eventually could be used to estimate cognitive impairment for the patient group. Results from this thesis will hopefully provide information to advance the understanding of variable RBE doses related to cognitive impairment for pediatric brain tumor patients receiving proton therapy.

2 Radiation therapy

Radiation therapy has been used in cancer treatment for more than a century. The life expectancy for cancer patients has been significantly improved over the last decades [26]. Enhanced imaging techniques and improvement of radiation treatment have been a critical source in the improvement of survival rates. Today, about 45-50% of all cancer patients will receive radiation therapy either as a supplement to surgery and chemotherapy or as an individual treatment modality [27]. The aim of all types of radiation therapy is to deposit sufficient dose to control the tumor while sparing healthy tissue.

Treatment with highly energetic photons is to date the most frequently used form of radiation therapy. Radiation therapy with protons as an alternative to photons are increasingly being used worldwide. The rationale for radiation treatment with protons compared to photons is the favorable depth-dose distribution, which reduces radiation dose to normal tissue. As of 2018, more than 180 000 patients were treated with proton therapy, of which approximately 10% of these were children [9, 28].

2.1 Physics of photon therapy

This project mainly focuses on proton therapy; however, due to the large extent of photons in radiation therapy some of the basic physics of photon radiation therapy will be presented briefly in the current sub-chapter. A photon is a neutrally charged and massless particle. Photons (also x- and ɣ-rays depending on energy) interacts with matter primarily by three processes, which contribute to energy absorption; photoelectric effect, Compton scattering and pair production [29]. These interactions are dependent on the photon energy (typically 4 – 25 MeV), the density and the atomic number, Z, of the absorbing material.

When photons interacts with a medium, they transfer their energy to electrons, which in turn will impart energy to surrounding tissue by producing ionization and excitation of atoms [29]. Photons are therefore considered indirectly ionizing. The intensity of the initial photon beam will be continuously reduced with depth when traversing matter, and the change in intensity can be found by the following exponential equation:

$$I(x) = I_0 e^{-\mu x}, \tag{2.1}$$

where I(x) is the intensity transmitted by a thickness x, I_o is the initial photon beam intensity and μ is the linear attenuation coefficient of the given material. The linear attenuation coefficient is closely related to the sum of contribution from each interaction process [30], commonly known as the total cross section, σ_{tot} . The equation for the total cross section is shown below:

$$\sigma_{tot} = \frac{\mu A}{\rho N_A}, \tag{2.2}$$

where N_A is Avogadro's constant, A is the atomic mass and μ/ρ is the mass attenuation coefficient.

As seen in Figure 2.1, the photon dose deposition increases with depths in tissue towards a maximum. This region is commonly referred to as the build-up region and is due to the range of high-speed electrons produces by the photon beam at the surface of the patients [29]. This maximum is positioned within a few cm inside the tissue, dependent on the initial beam energy and treatment field size. Beyond the point of maximum, the dose deposition decreases exponentially due to photon attenuation.

2.2 Physics of proton therapy

This chapter aims to describe the essentials of proton therapy physics. Firstly, the capability to deposit energy through ionization of the tissue is shared by all types of radiation. However, the interactions which lead to deposition of energy in tissue differ between charged particles and neutrally charged particles, as e.g. photons. Charged particles have the potential to directly ionize material, whereas photons have to experience an indirect interaction with particles capable of direct ionization [29].

Protons, as seen in Figure 2.1, deposit most of the dose near the end of the range of the proton beam, followed by a sharp dose fall-off. As the range of the protons is highly dependent on the primary beam energy, the position of the maximum dose deposition can be placed within the target volume. Compared to photon therapy, these physical characteristics can lead to a lower integral dose and no exit dose while still delivering a uniform dose to the target volume. Proton therapy, therefore, can spare normal tissue, which is an important aim when treating tumors with radiation therapy.

2.2.1 Stopping power

The stopping power for a charged particle is the average loss of energy *dE* per unit length *dx* in a medium, generally given in units of keV/μm. This rate of energy loss is mathematically described by the Bethe-Bloch formula [31]:

$$-\frac{dE}{dx} = 2\pi N_a r_e^2 m_e c^2 \rho \frac{Z}{A}\frac{z^2}{\beta}\left[\ln\left(\frac{2m_e\gamma v^2 W_{max}}{I^2}\right) - 2\beta^2 - \delta - 2\frac{C}{Z}\right] \quad (2.3)$$

Table 2.1: Description of parameters used in the Bethe-Bloch equation.

Variable	Definition	Unit and value to the variables
$\mathbf{N_a}$	Avogrado's constant	6.022×10^{23} mol^{-1}
$\mathbf{m_e}$	Electron rest mass	$0.511 \frac{MeV}{c^2}$
c	Speed of light in vacuum	2.998×10^{8} ms^{-1}
Z	Atomic number of absorbing material	
A	Atomic weight of absorbing material	g mol^{-1}
z	Charge of incident particle	
β	Relative particle velocity to the speed of light	
v	Projectile velocity	ms^{-1}
$\mathbf{r_e}$	Electron radius	2.818×10^{-15} m
I	Mean excitation potential	eV
ρ	Density of the absorbing material	g cm^{-3}
$\mathbf{W_{max}}$	Maximum energy transfer from a single collision	
γ	Lorentz factor	
δ	Density correction	
C	Shell correction	

Table 2.1 presents a description of the parameters in the Bethe-Bloch equation. As seen by equation (2.3), the deposited energy is inversely proportional to the square of the velocity of the particle. In other words, protons deposit more dose at low velocity and less dose at high velocity [32]. This leads to a maximum dose deposition at the end of the path, commonly referred to as Bragg Peak [33] (Fig 2.1). The characteristic of the Bragg peak is shared by all heavy charged particles. However, the sharpness and relative height of the peak increases with increasing mass [32].

The initial beam energy for a proton beam is typically from 70 – 230 MeV [29]. The range of the particles is defined as the depth at which half of the particles in the material have come to rest [34]. The penetration depth of the charged particles is determined by the initial energy, material composition and density of the material. However, as the particles will endure different interactions as they travel through the material, the range of each particle differs. This determines the width of the Bragg peak and is known as range straggling. To accomplish the same depth in material as lighter ions, e.g., protons, heavier ions need higher energy, which can be seen from the particle charge, z, in the Bethe-Bloch equation (Eq. 2.3). The monoenergetic proton beam reaching the head of the treatment delivery system creates a narrow peak, called the pristine peak. In order to cover the entire target volume, multiple pristine peaks of different energies and ranges are added together to create a flat dose plateau, which is known as a spread-out Bragg Peak (SOBP) [29].

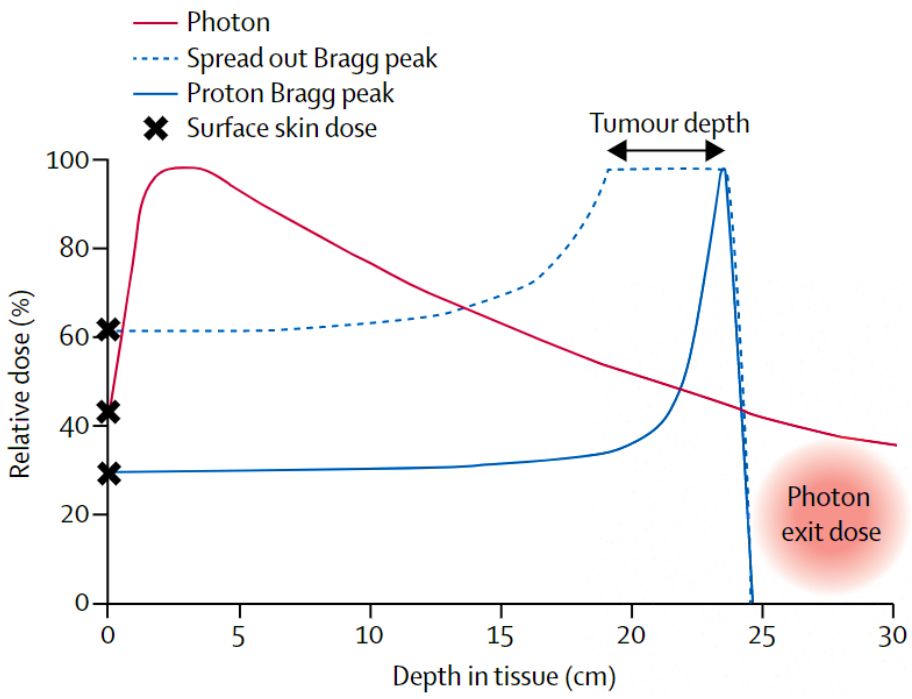

Figure 2.1: Comparison of the longitudinal depth dose distribution of protons (solid blue line) and photons (solid red line). The SOBP is shown by the dashed blue line [35]. Photons have a maximum dose deposition within a few centimeters before the dose exponentially decreases. Protons deposits a large fraction of the dose at the end of the beam range.

2.3 Interactions of charged particles in matter

The deposition of energy from protons is highly energy dependent. At therapeutic proton beam energies, protons interact with human tissue mainly through three interactions; coulomb interaction with atomic electrons or the atomic nucleus, or nuclear interaction [27].

2.3.1 Coulomb interactions with atomic electron

Particles with mass greater than the rest mass of an electron are considered heavy charged particles [29]. Coulomb interaction with an orbiting atomic electron is the leading cause of energy loss of heavy particles traversing through a medium. In these interactions, protons lose some of their kinetic energy by ionization and excitation of atoms. When a bounded electron is raised to higher energy levels, the process is called excitation. The process is determined as ionization if the radiation has adequate energy to eject an electron from the atom [36]. This causes an electron to be ejected from the atomic orbit. The electron will further deposit the dose locally due to the short range of the electron.

2.3.2 Multiple Coulomb scattering

When a proton passes a nucleus with a distance smaller than the atomic radius, the repulsive force of the nuclei changes the trajectory of the protons [26]. The repulsive force causing the deflection away from the original trajectory is due to the positive charge for both the proton and nuclei. The scattering angle is dependent on the material. These interactions do not result in the loss of energy of the protons. However, the sum of multiple scattering processes leads to the deflection of the original path, causing a lateral broadening of the original beam.

2.3.3 Inelastic nuclear interactions

Nuclear interactions, often referred to as non-elastic collisions, occurs when a proton is absorbed by an atomic nucleus. Compared to interaction processes causing ionization and excitation, non-elastic collisions are less likely to occur. In these interactions, the incoming protons knock secondary particles, i.e., protons, neutrons or ion clusters, out of the atomic nuclei [37]. In most cases, the secondary particles have relatively low energy compared to the incoming proton. Despite the low probability of occurrence compared to interactions with

electrons and Coulomb scattering, non-elastic collisions are accounted for when planning proton radiation therapy [37].

2.4 Dosimetry

2.4.1 Absorbed dose

The absorbed dose, which is the most common quantity used in dosimetry, is defined as the radiation energy imparted per unit mass of an irradiated body [29]. The quantity absorbed dose, D, is a function of the mean energy, ΔE, imparted to the material of mass Δm by ionizing radiation,

$$D = \frac{\Delta E}{\Delta m}, \tag{2.4}$$

where the dose, D, is measured in Gray (Gy), which is equivalent to J/kg.

3 Treatment planning and delivery

Treatment planning refers to a multi-step process that typically starts with image acquisition and defining volumes of interest. Further, the radiation dose deposition needs to be prepared using dedicated software. This process also includes selection of treatment delivery technique and choice of beam angles and energies [29]. The intention of treatment planning is to deposit dose restricted to the tumor while sparing healthy tissue. To achieve successful treatment, thorough planning prior to radiation therapy treatment and accurate execution is a necessity. The following chapter will introduce some important concepts of radiation therapy planning and delivery.

3.1 Volume definitions

The International Commission of Radiation Units (ICRU) Report 50 labeled various dose and volume specifications in radiation therapy. These specifications are presented in Figure 3.1. In ICRU report 50, the gross tumor volume (GTV) was defined as the gross demonstrable extent and location of the tumor [38]. This tumor volume usually consists of the primary tumor and metastasis (spread of cancer cells) [29, 39]. The clinical tumor volume (CTV) is an extension of the GTV and represents the assumed tumor volume. To successfully achieve the therapeutic aim, the prescribed dose should cover the CTV [29]. In order to account for deviations in the CTV due to anatomical motion, an internal margin (IM) is added to the CTV [38]. The volume which contains the CTV and the IM is the internal target volume (ITV).

The PTV is, as stated by the ICRU Report 50, a statistical concept which accounts for all possible geometrical deviations and inaccuracies [39]. This volume contains the CTV and accounts for all uncertainties, e.g. patient motion and setup error, by adding a margin of error to make sure that the prescribed dose is delivered to the CTV. Most of the defined volumes holds for both photon and proton therapy. A later report dedicated to proton therapy from the ICRU, Report 78, suggested that the traditional concept of PTV was not feasible in proton therapy [40]. Due to the range uncertainties of a particle beam, an additional margin should be added to the PTV at the distal end of the beam when planning proton therapy treatment.

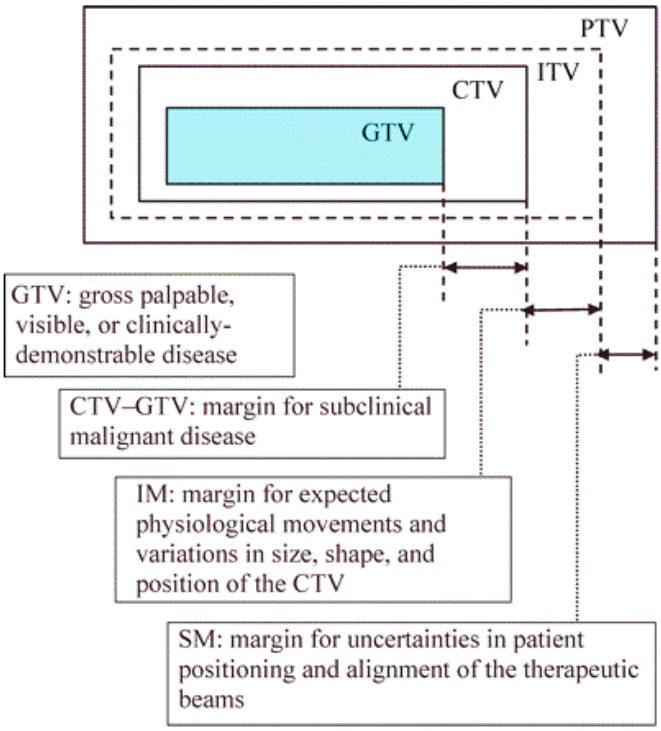

Figure 3.1: Schematic illustration of volumes and margins related to radiation therapy as defined by the ICRU [38]. The internal margin, IM, compensates for anatomical variations in the CTV. The GTV and CTV is modality independent, whereas the margin between the CTV and PTV differs between photon- and proton therapy.

3.2 Plan evaluation

An important tool in evaluating treatment plans is the Dose Volume Histograms (DVH). The DVH displays the dose as a function of volume in either percent or absolute value within a volume of interest. Therefore, the DVHs are an essential tool to reduce the dose in healthy tissue as much as possible.

When assessing the effect of radiation on the tumor volume and the normal tissues, the tumor control probability (TCP) and normal tissue complication probability (NTCP) are commonly evaluated. These sigmoid-shaped dose-response curves (Fig. 3.2) are grounded on the assumption that increased dose will increase the tumor response and damage to normal tissue [41]. The distance between the two dose-response curves, known as the therapeutic ratio or therapeutic window, describes the likely difference between TCP and NTCP and is thereby a measure of the quality of a radiation treatment plan. An important aspect of radiation treatment planning is to widen the gap between the TCP and NTCP as much as possible.

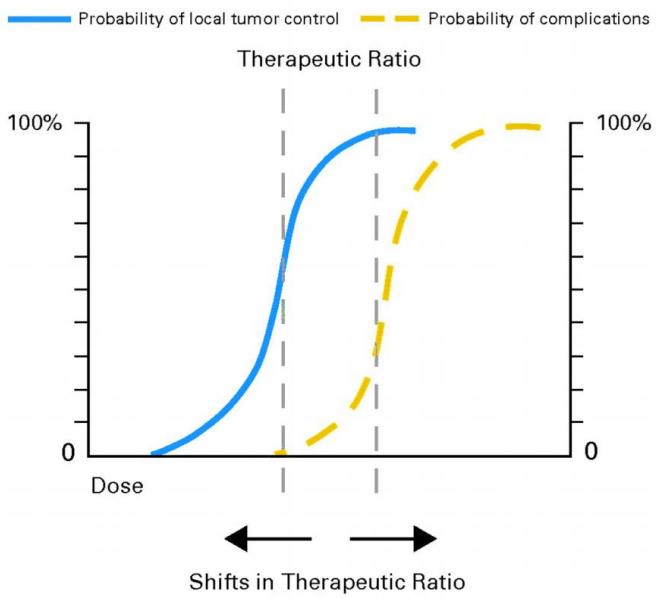

Figure 3.2: Illustration of the sigmoid-shaped dose-response curve for TCP (blue) and NTCP (yellow) [42]. The distance between the two curves, the therapeutic ratio, should preferably be as wide as possible.

3.3 Medical imaging in radiation therapy

In order to deliver the dose accurately to the patient, precise reconstruction of the patient anatomy is a necessity. Typically, a 3D anatomical model is created by the use of Computed Tomography (CT). Also, magnetic resonance imaging (MRI) and positron emission tomography (PET) are used to complement additional anatomical data to construct a precise anatomical model of the patient. Pediatric CNS tumors MRI offer more soft tissue contrast, allowing for more accurate normal tissues and tumor volume definition, whereas PET offers functional information, mostly used for target volume definition. The CT data provides a 3D electron density map of the patient, which is used in the delineation of the target volume and critical structures, in addition to the calculation of the dose distribution within the patient [43].

3.4 Dose calculation algorithms

CT images of the patients anatomy, including delineated structures and volumes, are imported to treatment planning software, known as treatment planning systems (TPS). TPS gives an estimate of how the dose is delivered to the patient by using pencil-beam algorithms. The

pencil-beam algorithms are based on mathematical models that simulate individual protons through a volume represented by a rectangular 3D grid of voxels [37]. The pencil-beam algorithms are considered to be highly accurate; however, in low-dose regions, the algorithm is less sensitive to density variations when compared to the Monte Carlo (MC) method [37], which is currently more widespread within research.

The Monte Carlo (MC) technique is acknowledged as the superior method of simulating particle interactions and dose depositions. In a study that compared pencil-beam algorithms and the MC method, Ma et al. found a difference in dose distribution near tissue inhomogeneities of 5 % [44]. MC simulations are widely being used to validate and support TPS, and are expected to be more implemented in treatment planning in the years to come [29, 45, 46]. Overall, TPS generally rely on the pencil-beam algorithms as this method has favorable computation time and provides reasonable accuracy.

3.5 Treatment delivery

3.5.1 Particle accelerators

Two types of accelerators are used to generate protons with adequate energy for therapeutic purposes; synchrotrons and cyclotrons. Cyclotrons operate at fixed-energies up to 250 MeV, which has a range of approximately 38 cm in water [24]. A strong magnetic field bends the constant particle beam trajectory into a spiral path. In the spiral path, the particles gradually gets accelerated, which increases the radius throughout the spiral-shaped motion. When the particles are accelerated to maximum energies, the particles can be steered to a beam transport system [47]. A material with adjustable thickness, commonly known as an energy degrader, is used to develop an SOBP by varying the beam energy.

In synchrotrons, the particle beam is steered in a circular motion by magnets inside a ring-shaped vacuum tube [29]. As opposite to cyclotrons, synchrotrons can adjust the particle beam energy to desired levels without using energy degraders.

3.5.2 Beam delivery techniques

The accelerated protons are delivered to the patient by one of two methods; passive scattering or active scanning. The two delivery techniques are shown in Figure 3.3. In the case of active

beam shaping, often referred to as Pencil Beam Scanning (PBS), the treatment delivery system guides a narrow beam to three-dimensional grids (voxels) using dipole magnets [29]. The particle beam is steered magnetically both horizontally and vertically, while the beam energy determines the depth of the Bragg peaks. Intensity modulated proton therapy (IMPT) is increasingly being used as a scanning technique. In IMPT, the dose distribution is constructed by multiple fields with non-uniform dose distribution, which when combined delivers a homogenous dose to the target volume. Compared to passive scattering, active scanning results in a favorable integral dose. This delivery technique is, however, sensitive to organ motion [29].

In passive scattering, the primary proton beam is scattered by placing materials of low-atomic number in front of the monoenergetic beam [29]. Dependent on the field size, the beam is scattered by one or two (double-scattering) materials. In order to deliver the dose restricted to the target volume, the scattered beam is shaped by collimators. In passive scattering, rotating filters are used as range modulators to achieve the desired SOBP within the target volume. The rotating filters vary in thickness, which allows the beam to be attenuated to a preferable energy. Due to interactions between the particle beam and nuclei in the collimators, nuclear fragments from these interactions will cause an elevated dose deposition which might harm normal tissue.

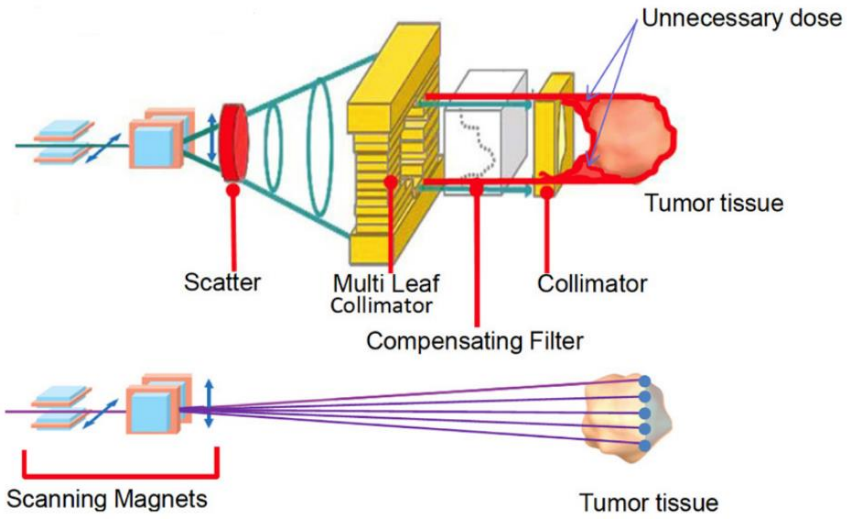

Figure 3.3: Illustration of proton delivery techniques [9]. In passive scattering (upper), the beam is scattered by a low Z material placed in front of the initial beam. Collimators and compensating filters are further used to adjust the beams shape and energy distribution. The active scanning technique (lower) controls a narrow beam into voxels inside the target volume using dipole magnets.

4 The biological effect of ionizing radiation

Radiobiology involves the study of ionizing radiation interaction with living cells or tissues, and includes both physical and biological aspects. The physical aspect involves interactions between charged particles and atoms or molecules within the tissue [41]. These interactions cause damages, or *lesions*, within the cells and produce biological damage.

The physics of charged particles is well understood. However, the biological impact of charged particles is not yet fully exploited [48]. To completely take advantage of the superior physical characteristics of particles compared to photons in radiation therapy, a better understanding of particle radiobiology is needed. The following chapter will summarize the main reasons for the differences in biological impact for protons compared to photons.

Radiation-induced damage is caused by either direct- or indirect action, as illustrated in Figure 4.1. In high LET-radiation, direct actions are dominant. In direct action, the secondary electron affects the DNA directly. In terms of indirect action, the biological damage is done when the radiation is absorbed in the material and releases charged particles [36]. The radiation interacts with atoms or molecules and produces free radicals (unstable atoms), which in turn will produce biological damage. The indirect action mainly occurs by ionization of water molecules due to the high concentration of water (approximately 80 %) in cells. The ionized water molecules produce highly reactive radicals called hydroxyls (OH), which causes biological damage. In terms of photon radiation, approximately two-thirds of the damage to the DNA is caused by OH [49].

DNA is the main target for radiation-induced cell killing [41]. The DNA consists of two strands in a helix-shaped structure which hold genetic information. Ionizing radiation produces lesions within the DNA, either through a single-strand break (SSB) or a double-strand break (DSB). In general, indirect action causes more SSB in comparison to direct action. Due to DNA repair mechanisms, the DNA is more likely to be repaired after SSB.

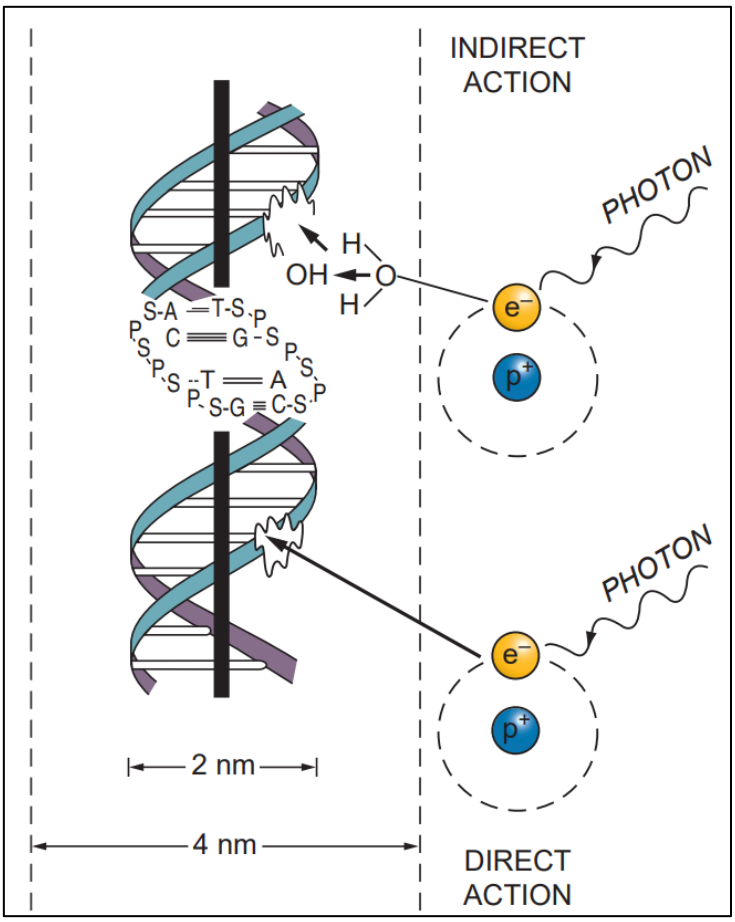

Figure 4.1: Illustration of direct and indirect action. In indirect action (top of the figure), the secondary electron interacts with a water molecule and produces a hydroxyl radical which will damage the DNA. In direct action (bottom of the figure), the secondary electron damages the DNA directly. The illustration is transferable to proton interactions [49].

4.1 Linear quadratic model

A plot of the surviving cell fraction against radiation dose, as illustrated in Figure 4.2, is known as a cell survival curve [41]. The biological response of cells to radiation is mathematically described by the linear-quadratic (LQ) model. In this model, the surviving fraction is given as

$$S(d) = e^{-\alpha d - \beta d^2}, \tag{4.1}$$

where d is the dose, and α and β are tissue parameters. The linear component of the equation, exp(-αd), is suggested to describe lethal single-track events as double-strand breaks in the DNA. The quadratic component, $\exp(-\beta d^2)$, represents the probability of two-track events causing lethal damage [41]. In a cell survival curve, the two tissue-specific parameters α and β represents the initial and final slope, respectively.

The two tissue-specific parameters, α and β, have dimensions Gy^{-1} and Gy^{-2}, respectively. The ratio of these two parameters, α/β, is often used to quantify the radiation fractionation of tissues [41]. For early responding tissue, e.g., tumors and skin, the range of α/β ratio values are between 7 - 20 Gy [41]. In the case of late responding tissue, such as brain structures and the spinal cord, values of the α/β ratio are typically between 0.5 to 6 Gy [41]. The reference radiation fractionation sensitivity is commonly given as $(\alpha/\beta)_x$ for photons.

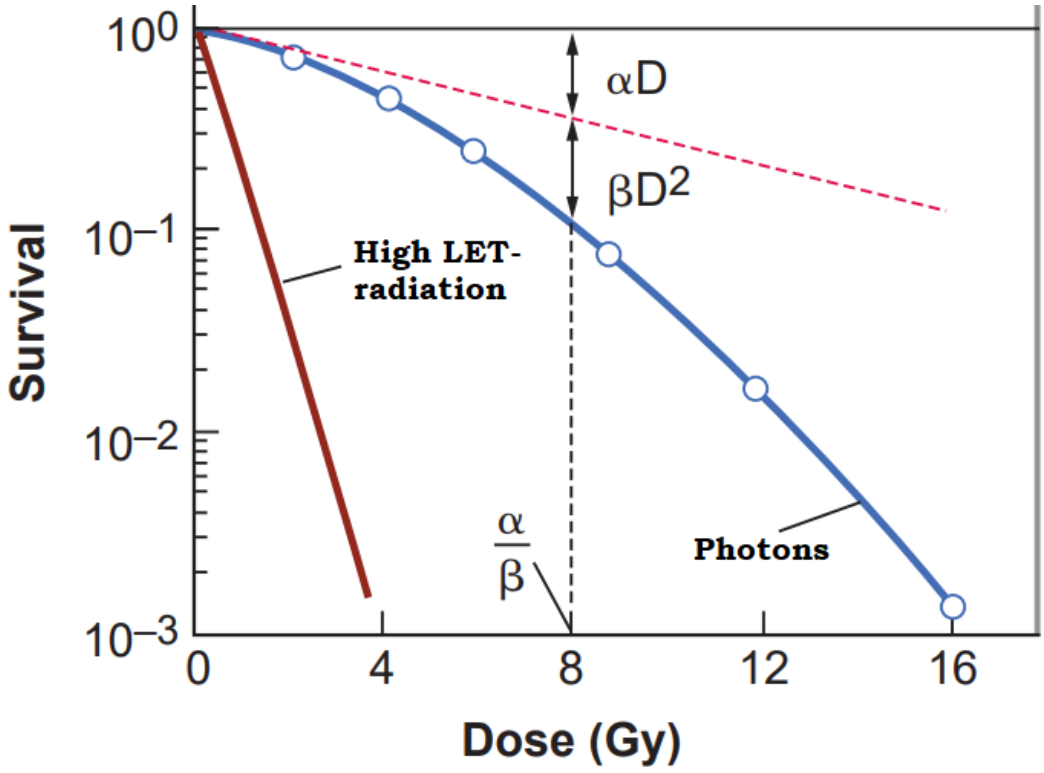

Figure 4.2: Illustration of dose-response curves for mammalian cells high LET-radiation and photons. Modified from Hall (2012) [49].

Cell survival is usually quantified as a function of dose from either *in vivo* or *in vitro* experiments. *In vitro* experiments are defined as experiments conducted outside of a living organism, whereas *in vivo* experiments are performed inside living organisms [41]. The most frequently used cell lines for *in vitro* experiments are Chinese hamster lung fibroblast cells (V79), in addition to HeLa cells (human cancer cells) and CHO cells (Chinese hamster ovary cells) [30]. The most commonly used cell lines, V79 cells, are characterized by a low $(\alpha/\beta)_x$ ratio and have a lower number of chromosomes when compared with human cell lines [50]. Clonogenic cells, or colony-forming cells, are defined as cells that are able to proliferate indefinitely and form colonies within a defined growth environment [41, 49]. Clonogenic cell survival is the most studied endpoint.

4.2 Linear energy transfer

The term Linear Energy Transfer (LET) was first introduced by Zirkle et al. in 1952 [51]. This term describes the ionization density along a particle trajectory and is commonly given in units of keV/μm. ICRU report 60 defines restricted LET, L_Δ, by the following equation [52]:

$$L_\Delta = \frac{dE_\Delta}{dl}, \tag{4.2}$$

where dE_Δ is the mean energy lost by charged particles due to electronic interactions, dl is the traversed distance and the Δ is the energy cut-off. If no energy cut-off is considered, i.e. $\Delta = \infty$, the LET is equal to the stopping power and is referred to as unrestricted LET (LET_∞) [53]. Proton beams are typically referred to as "low-LET"-radiation compared to heavier ions for clinically relevant energies, and LET values from 1 – 10 KeV/μm are common in therapeutic beams [27].

Both restricted and unrestricted LET applies to mononergetic beams only, whereas in reality, proton beams consist of particles with a wide range of different LET values. For simplicity when studying the biological outcome, the unrestricted dose-averaged LET (LET_d) value is commonly used [54]. This concept, given in equation (4.3), accounts for both LET and dose [54].

$$LET_d(z) = \frac{\int_0^\infty S_{el}(E)D(E,z)dE}{\int_0^\infty D(E,z)dE} \tag{4.3}$$

In this equation, the term $S_{el}(E)$ is the electronic stopping power of a proton with kinetic energy E, and D(E,z) is the absorbed dose by a proton with kinetic energy E in the tissue at location z [54].

The LET is a measure of the quality and efficiency of a beam. An increase in LET will, in general, produce more cell killing per Gray [41]. This can be seen by the steepness of the survival curve, which was presented in the previous chapter (4.1). Also, the survival curve becomes straighter with a less distinct shoulder with high LET-radiation. The latter is suggested to be explained by less probability for the cell to repair from high LET-radiation as compared to photons [41].

4.3 Relative biological effectiveness

The deposited dose from different types of radiation does not result in equal biological effect. The relative biological effectiveness (RBE) serves as a link between the vast knowledge on the biological effect of photon radiation and transfers to proton radiation. In general, a lower absorbed dose with proton therapy is needed to achieve the same biological effect compared with photons. In the context of proton therapy, the RBE is defined as the ratio between photon reference dose, D_x, and proton dose, D, achieving the same biological effect. The relationship for the RBE is shown below:

$$\mathrm{RBE} = \frac{D_x}{D} \tag{4.4}$$

The RBE-weighted dose is commonly used to quantify treatment expectations [55]. The RBE-weighted dose is given as the RBE multiplied with the dose, and is measured in Gy(RBE). In clinical practice, patients treated with protons are typically prescribed with doses where the photon-equivalent RBE-weighted dose matches the photon physical dose [56]. In this manner, the RBE-weighted dose to the patient is equivalent to the physical photon dose divided by the RBE.

A generic value of 1.1 is recommended for RBE in clinical use by ICRU [57]. This value was adopted based on *in vitro* and *in vivo* experiments [58]. On average, RBE can be considered between 1.1 and 1.15 from the entrance to the center of an SOBP, then increases to ~ 1.35 at the distal edge, and increases to ~1.65 in the distal fall-off [59]. The value of 1.1 was suggested as an average over various endpoints, fractionation over 2 Gy, and at the center of the target volume [59]. An assumption of an average over various endpoints may not be sufficient as recent studies have shown RBE to vary depending on the endpoint. An RBE at the center of an SOBP was found to be 1.22 ± 0.02 of *in vitro* experiments, while *in vivo* experiments provided a value of 1.10 ± 0.01 [59].

4.3.1 Dependencies of relative biological effectiveness

The RBE is dependent on several factors, including the quality of radiation, dose, and the biological endpoint. The different RBE dependencies will be explained in the following sub-

chapter. Firstly, the LET has a central role in estimates of the RBE. Most experiments show an approximately linear increase in RBE with increasing LET [59].

High LET radiation has increased biological effectiveness compared to photons, due to higher production of non-reparable lesions with increased ionization density [60]. As shown in section 4.2, the LET is dependent on beam energy and will increase as the protons slow down. The RBE has been shown to increase along the track of the protons and result in the highest value in the distal end. This is also where the LET value is at its highest. In the center of an SOBP, the LET value is potentially ~ 5 keV μm^{-1}, and in the sharp fall-off at the distal end of the peak, the LET value may be ~ 20 keV μm^{-1} [59].

The biological effectiveness reaches its maximum at LET values of approximately 100 keV/µm and decreases beyond this point [41]. Radiation with LET above 100 keV/µm deposits more energy than what is required to kill the cell [41]. This overkill effect is illustrated in Figure 4.3. In the clinical use of protons, LET values over 30 keV μm^{-1} are not common, even though LET-hotspots may occur.

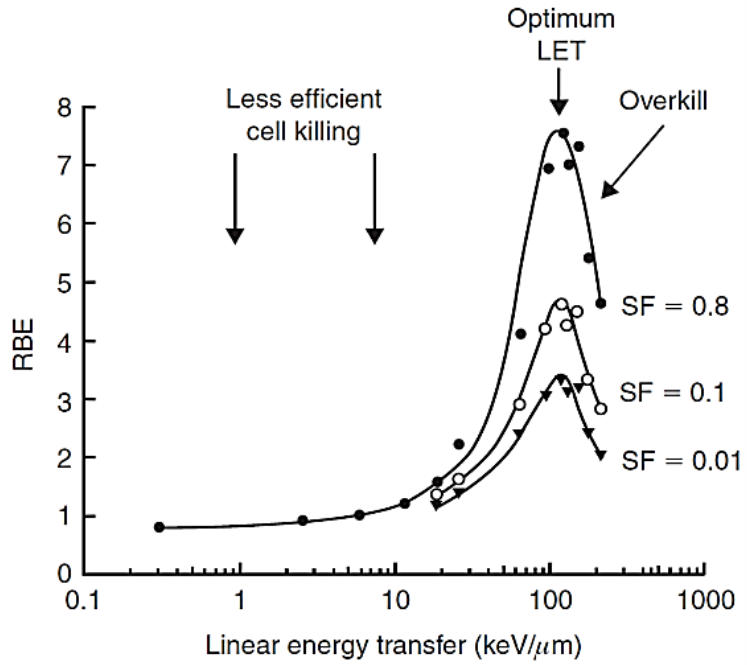

Figure 4.3: Illustration of the RBE dependence on LET, also explaining the phenomenon of cell overkill from high LET radiation [61]. The survival fraction (SF) levels are shown right in the figure.

In addition to the LET dependency, the RBE is also tissue-dependent. Experimental data have shown a clear trend of increased RBE with decreasing $(\alpha/\beta)_x$ [58]. The current value of 1.1 is suggested to underestimate RBE at low $(\alpha/\beta)_x$ and overestimate the RBE at high $(\alpha/\beta)_x$ [59], and especially organs at risk with low $(\alpha/\beta)_x$ within proximity of high LET_d values may be

underestimated in terms of RBE [62]. In terms of dose dependency, experimental in vitro and in vivo data show higher RBE as the dose decreases [58].

4.3.2 Published models accounting for the variable relative biological effectiveness

Several phenomenological models have been developed to include variations in the physical and biological parameters in the estimation of variable RBE [63-75]. Recently, Rørvik et al. compared eleven phenomenological models as well as two plan-based variable RBE models [76]. The two plan-based variable RBE models, Frese et al. (FRE) and Unkelbach et al. (UNK), are mainly models for LET optimization and are not fitted to *in vitro* data but based on information from treatment plans [63, 72]. These models assume an RBE linearly dependent on LET_d and that the average RBE inside the target volume is 1.1.

The phenomenological models explored by Rørvik et al. are derived from fits to existing experimental in vitro data and grounded on the LQ model. This is also the case for the suggested variable proton RBE model by Chaudary et al. [64]. In the context of the LQ model, a general expression for the RBE can be written as a function of physical dose deposited per fraction, D_P, and the biological tissue-parameters α and β, and α_x and β_x for protons and photons, respectively. The general expression is shown in equation (4.6).

$$\mathrm{RBE}(D, \alpha, a_x, \beta, \beta_x) = \frac{D_x}{D} = \frac{1}{2D}\left(\sqrt{\left(\frac{a_x}{\beta_x}\right)^2 + 4D\frac{\alpha_x}{\beta_x}\frac{\alpha}{\alpha_x} + 4D^2\frac{\beta}{\beta_x}} - \frac{\alpha_x}{\beta_x}\right) \tag{4.5}$$

The RBE at the lower and upper limit of the physical dose, i.e. lower and upper limit of surviving fraction, is commonly given as RBE_{min} and RBE_{max}, respectively [77, 78]. The two terms are quantified by the following equations:

$$\lim_{D\to 0} \mathrm{RBE} = \mathrm{RBE}_{max} = \frac{\alpha}{\alpha_x} \tag{4.6}$$

$$\lim_{D\to \infty} \mathrm{RBE} = \mathrm{RBE}_{min} = \sqrt{\beta/\beta_x} \tag{4.7}$$

From these equations, equation (4.5) can be rewritten as:

$$\mathrm{RBE}\left(\mathrm{D},\left(\frac{\alpha}{\beta}\right)_{\mathrm{x}},\mathrm{RBE}_{\max},\mathrm{RBE}_{\min}\right)=\frac{1}{2\mathrm{D}}\left(\sqrt{\left(\frac{\alpha}{\beta}\right)_{\mathrm{x}}^{2}+4\mathrm{D}\left(\frac{\alpha}{\beta}\right)_{\mathrm{x}}\mathrm{RBE}_{\max}+4\mathrm{D}^{2}\left(\frac{\alpha}{\beta}\right)_{\mathrm{x}}\mathrm{RBE}_{\min}}-\left(\frac{\alpha}{\beta}\right)_{\mathrm{x}}\right) \quad (4.8)$$

Equation (4.8) is shared by all variable RBE models based on the LQ model [76]. The dissimilarities between models based on the LQ model in terms of the equations are the definition of the RBE_{max} and RBE_{min}. In addition to the difference in the formalism of the RBE_{min} and RBE_{max}, the variable RBE models are based on different experimental data and utilized different regression techniques in model fitting. Experimental RBE values have been shown to vary both across and within different cell lines [59].

Most models are based on experimental *in vitro* databases. The models by Chen and Ahmad (CHE), Wilkens and Oelfke (WIL), and Carabe et al. (CAR) are all exclusively based on the V79 cell line. As these models only are derived from one cell line, the range of $(\alpha/\beta)_x$ values is constricted, which can be observed in the right panel in Figure 4.4. These models may be inapplicable to some patient cases where the radiation fractionation sensitivity is higher or lower than in the studied cell line. Experimental data from various *in vitro* studies based on the survival of V79 cells indicate a higher RBE compared with other cell lines [27]. The V79 cell may, however, be more relevant for low $(\alpha/\beta)_x$ values in brain tissue.

By the use of multiple cell lines, a greater range of $(\alpha/\beta)_x$ values is achieved by some of the models. The models by Peeler (PLR), Tilly et al. (TIL), Wedenberg et al. (WED), Jones (JON), Mairani et al. (MAI), McNamara et al. (MCN), Chaudary et al. (CHD) and Rørvik et al. (ROR) use multiple cell lines and therefore have a broader range in terms of $(\alpha/\beta)_x$ values.

CHD and PLR use human cell lines. The analyzed cells in the PLR model are H460 and H1437, whereas the cell lines used in the CHD model are AG01522 and U87. The CHD model and all variable RBE models explored by Rørvik et al. besides WIL, CHE and UNK are tissue dependent, i.e. dependent on $(\alpha/\beta)_x$. The JON and FRE models utilizes α_x and β_x separately instead of the ratio between the two tissue-specific parameters.

Of the eleven phenomenological models explored by Rørvik et al., all models with the exception of CHE, ROR and PLR assume a linear relationship of RBE as a function of LET_d. This assumption also applies to the CHD model. Rørvik et al. developed two variable RBE models, using different statistical weighting for the two suggested models [66].

As seen in the left panel of Figure 4.4, there is a considerable variation in LET_d values of data points in databases across all models. CHE, TIL, MAI and WED have no LET_d data points below 7.7 keV μm^{-1}. For these models, the lack of datapoints is accounted for by extrapolation from high LET_d data

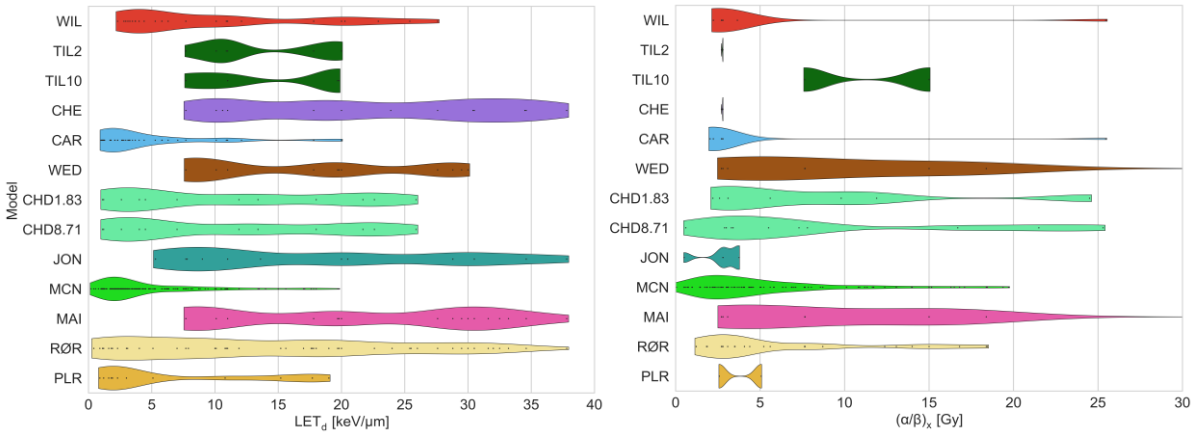

Figure 4.4: Distribution of LET_d (left) and $(\alpha/\beta)_x$ (right) values from the databases of each model. The plot has been modified from Rørvik et al. [66] by adding values for Chaudhary et al. [64] and removing values for the model by Belli et al. [79]. As seen in the right panel, a broader range of $(\alpha/\beta)_x$ values is achieved by models based on multiple cell lines.

5 Cognitive impairment of pediatric CNS tumor patients after radiation therapy

Despite being a vital treatment technique when curing cancer, radiation therapy treatment might damage healthy tissue and affect cognitive domains. Preservation of healthy tissue is one of the primary concerns when treating with radiation therapy. Quality of life is considered second in importance, only surpassed by survival [80]. Learning, attention and memory are all cognitive functions that might be affected, which potentially could influence the patient's quality of life. Pediatric patients are of particular risk of suffering from cognitive impairment as their brain develops rapidly at young age. Also, pediatrics have a greater degree of so-called myelination of white matter tracts and a higher degree of neurogenesis compared to adults which may play a role [81]. Both the radiation dose and volume of irradiation are suggested to have an impact on cognitive outcomes [82, 83]. The comparative physical advantages of protons over photons might limit the cognitive side effects, due to less damage to normal tissue.

5.1 Radiation-induced cognitive brain damage

The brain tissue can be divided into two components; grey and white matter. Structural brain changes in these two components have been related to a broad variety of neurocognitive outcomes [84]. White matter is vital in linking several elements of grey matter together. Myelin, which is produced in the oligodendrocytes, is essential in signaling transmission. Oligodendrocytes form and preserve myelin, which surrounds white matter axons, as seen in Figure 5.1 [85]. Radiation causes oligodendrocytes depletion, which results in demyelinated axons. In addition, impairment in white matter microvessels might damage the astrocytes, which provides functional support to neurons [85]. The demyelination and impairment in white matter microvessels are presumed to be roots of white matter damage. Peiffer et al. suggested a neuroanatomical target theory based on the assumption that selective damage to specific targets may result in cognitive impairment [86]. The neural stem cell number is considerably reduced at 10 Gy. At 40 Gy, white matter damage is likely to occur.

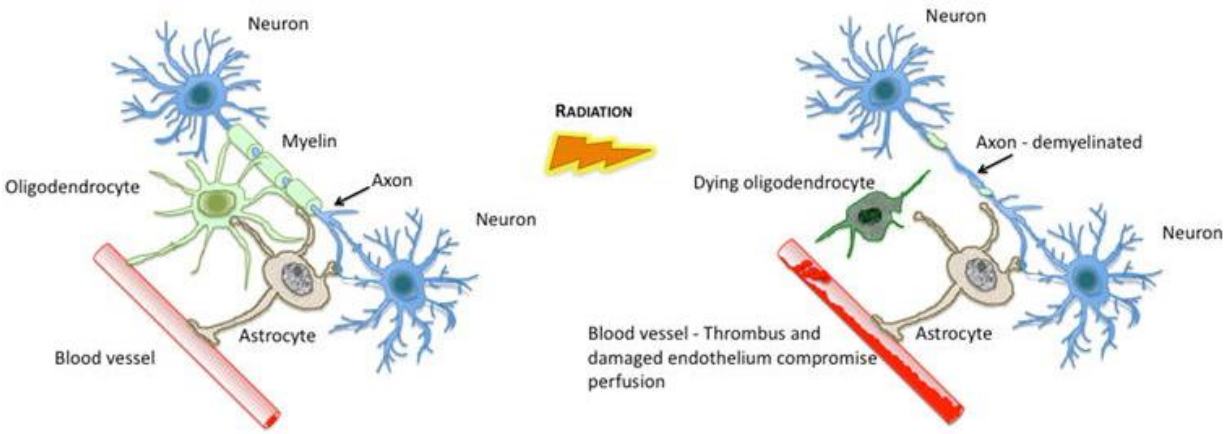

Figure 5.1: Illustration of radiation-induced white matter damage [85]. As seen in this figure, the radiation causes oligodendrocytes depletion which demyelinates the axons.

5.2 Published models used to estimate change in intelligence quotient score

When assessing the general neurocognitive functioning of patients undergoing brain tumor treatment, the full-scale intelligence quotient (FSIQ) is commonly used [87]. This measure labels several intellectual skills, i. e. working memory, processing speed, verbal comprehension, and perceptual reasoning. In clinical settings, estimated intelligence quotient (IQ) is also commonly used. However, the estimated IQ does not take into account the processing speed, which is one of the main contributors to the decline estimate in FSIQ for pediatric brain tumor patients [87].

There have been multiple previous attempts to model the effect of radiation therapy treatment on IQ scores [10, 19, 21, 88]. A prior study found that patients receiving > 43.2 Gy to a threshold volume of 13 % to the left temporal lobe were of particular risk of experiencing a decline of more than 10 % in FSIQ score.

Merchant et al. endeavored to model the outcome of treatment dosimetry on IQ score, based on a group of central nervous system (CNS) embryonal tumor patients [19]. The patients in this study were treated with craniospinal irradiation and conformal primary-site irradiation. From this study, several models were proposed, both dose/volume intervals and mean dose to five different volumes of brain tissue, i.e., total brain volume, supratentorial brain, infratentorial brain, left temporal lobe and right temporal lobe.

Conceptually similar IQ score models, utilizing similar methods as the previously mentioned study, was suggested by two studies by Merchant et al. [10, 88]. One of these studies was based on pediatric craniopharyngioma patients receiving conformal photon radiation therapy [88]. From the suggested models by this study, three partitions of dose intervals (low, intermediate, and high) to the total brain, supratentorial brain, and left temporal lobe could be used to estimate IQ scores. The other study compared the clinical advantages of proton over photon therapy in terms of IQ decline [10]. In this study, 10 of 40 patients were pediatric patients with craniopharyngioma. The group modeled a craniopharyngioma-specific model, which estimates the IQ score with respect to radiation mean dose to the supratentorial brain. Further explanation of these models will be given in methods sub-chapter 6.5.2.

5.3 Endpoint-specific cognitive impairment

When investigating cognitive impairment, it is furthermore relevant to look at more specific endpoints beyond the more comprehensive IQ measure. Pulsifer et al. indicated that the IQ score in pediatric patients receiving proton therapy treatment remained stable up to three years after treatment; however, the processing of speed was negatively affected [11]. A more recent study by the same group also reported considerable impairment in processing speed, in addition to a small negative change in IQ score [89]. Results of domain-specific impairment may potentially stress an underestimation of cognitive impairment if exclusive use of IQ score is used [87].

Substructures are connected to cognitive abilities in various ways. Recent studies have investigated the association between smaller substructures and cognitive decline. For instance, Redmond et al. demonstrated a significant correlation between the mean dose to the hippocampus and the decline in some neurocognitive skills [90]. Zureick et al. suggested that the radiation dose to the left hippocampus might lead to more cognitive impairment in terms of memory score than the left temporal lobe [23]. Zureick et al. modeled the dosimetric correlation of verbal and visual memory outcomes after proton radiation treatment for pediatric brain tumor patients. The hippocampus structures are connected to learning and memory domains and are suggested to be particularly sensitive to radiation [91]. Preservation of these structures might have a positive effect on memory function and, thereby, also on patients quality of life [92].

6 Materials and methods

6.1 Patient data

Ten anonymized pediatric patients with craniopharyngioma, previously treated at the University of Florida Health Proton Therapy Institute (UFHPTI), were included in this thesis. Intensity-modulated proton therapy (IMPT) plans with a three-field beam configuration optimized with RBE 1.1 were available for the set of patients, identical to the setup of the double scattering proton plans (DSPT) they were treated with. The beam set-up and dose distribution are illustrated in Figure 6.1. The clinically delivered DSPT plans typically used a right and left superior anterior oblique fields as well as a superior posterior oblique field [13]. The prescribed dose to the tumor volume was 54 Gy(RBE) with a constant RBE of 1.1 in 30 fractions. The clinically approved structure sets were used for treatment planning, while BCSs (identified and defined by Toussaint et al. [81]) were originally delineated from the registered CT- and T1/T2 MRI-scans. The delineated BSCs are illustrated in Figure 6.2 and listed in Table 6.1, and are categorized into structure subgroups, as in the publications by Toussaint et al. [13, 81]. The median (range) primary planning target volume (PTV) was 31 cm^3 [18 – 63] across all patients.

Table 6.1: BSCs analyzed in this thesis categorized into structure subgroups (left column). The column to the right shows the median and corresponding range of the volume of each BSC [13, 81].

Subgroups	**Structures**	**Volume [cm^3] Median [range]**	
Posterior fossa substructures	Cerebellum	125.0 [89.6, 137.0]	
	Cerebellum Anterior	20.7 [15.6, 30.9]	
	Cerebellum Posterior	99.5 [73.2, 113.6]	
		Left	Right
Temporal lobe substructures	Hippocampus Head	0.9 [0.7, 1.1]	0.6 [0.4, 1.5]
	Hippocampus	2.0 [1.0, 2.9]	1.9 [1.0, 3.0]
	Hippocampus Tail	1.0 [0.7, 1.4]	1.0 [0.6, 1.5]
	Amygdala	0.6 [0.3, 0.8]	0.6 [0.4, 0.6]
	Entorhinal Cortex	1.5 [1.3, 2.0]	1.5 [1.3, 1.9]
		Left	Right
Ventricular substructures	Subventricular zone	6.3 [3.6 8.3]	5.8 [3.2, 14.1]
	Cingulum	1.1 [0.7, 1.2]	1.1 [0.7, 1.4]
	Fornix	0.9 [0.3, 1.4]	
	Corpus callosum	8.7 [6.6, 11.6]	
		Left	Right
Other supratentorial substructures	Frontal Lobe	207.5 [154.5, 228.0]	222.4 [157.7, 237.1]
	Parietal Lobe	103.5 [83.9, 136.7]	106.0 [80.5, 123.9]
	Temporal Lobe	93.1 [65.9, 126.0]	104.5 [67.5, 135.9]
	Thalamus	5.8 [4.8, 6.9]	5.6 [4.9, 7.2]
	Left frontal white matter	8.6 [7.3, 10.5]	

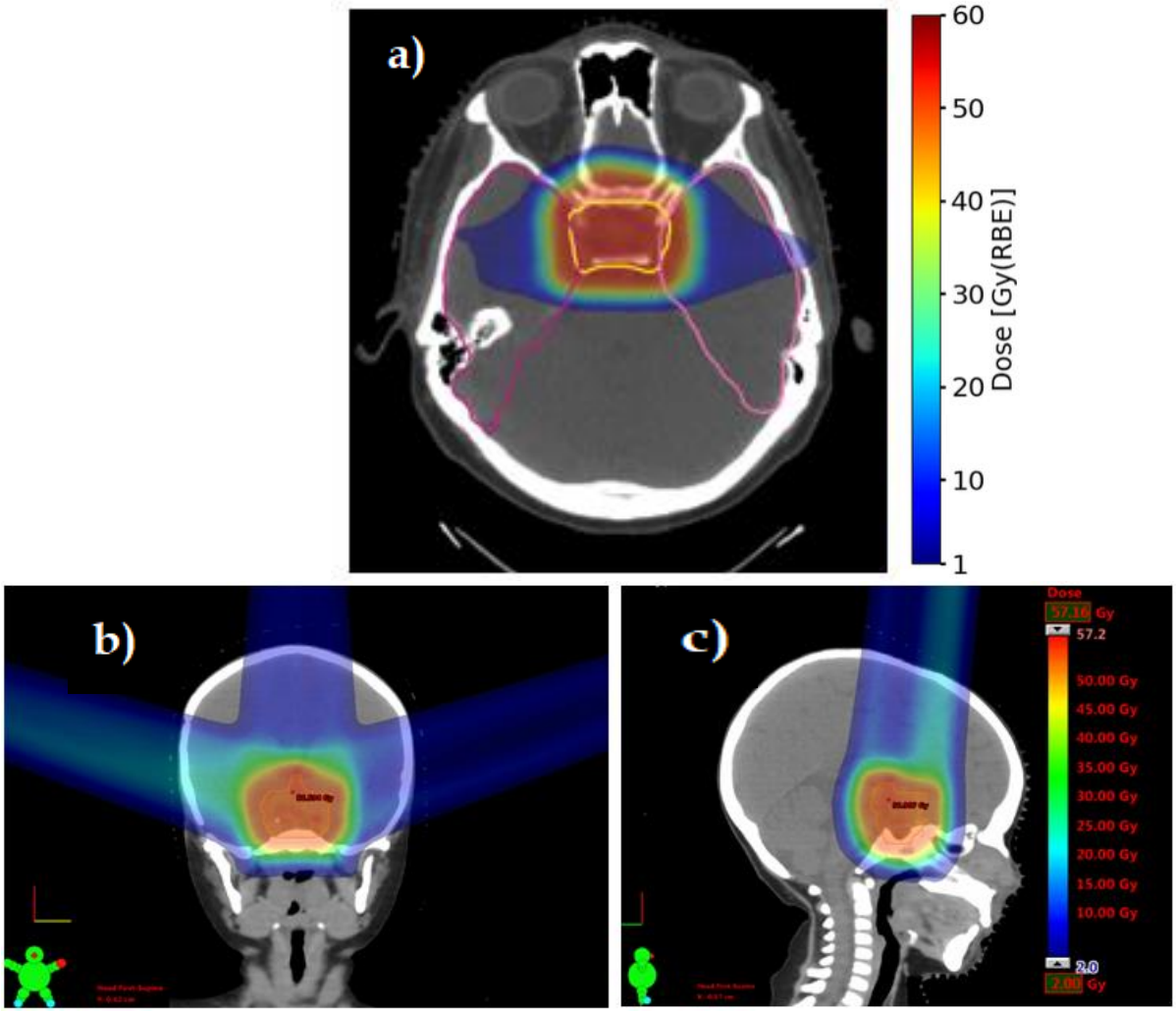

Figure 6.1: RBE-weighted dose (RBE = 1.1) distributions for the patient with a target volume closest to the median value. CTV is shown in yellow and temporal lobes are shown in pink for a), whereas the CTV is shown in orange for b) and c). Panel b) illustrates the right and left superior anterior oblique field whereas c) illustrates the superior posterior oblique field. The dose bar in panel c) is shared by both b) and c).

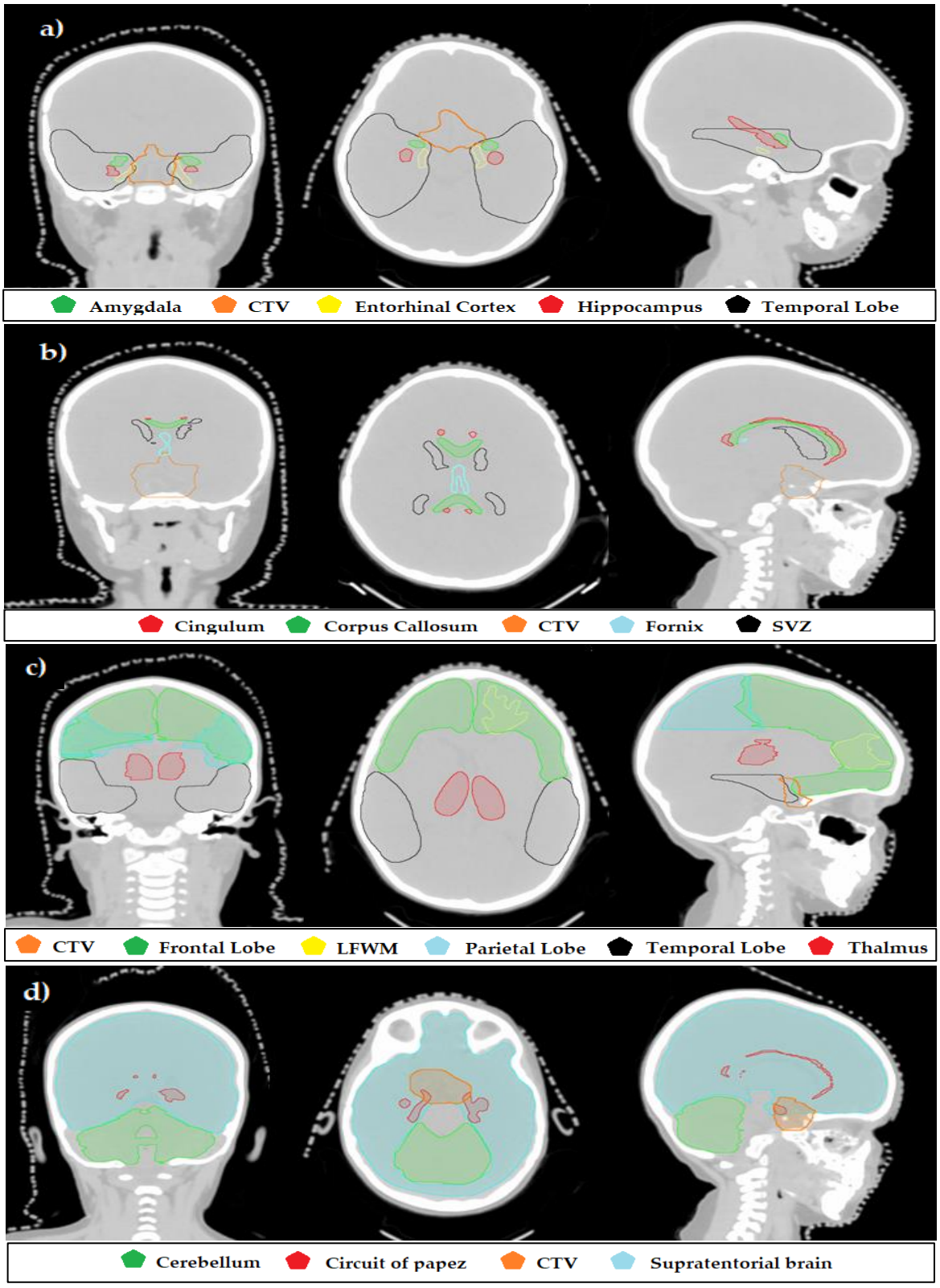

Figure 6.2: Frontal (left column), transversal (middle column), and sagittal (right column) slice view of the delineated BSCs. The temporal substructures are shown in a), the ventricular substructures are shown in b), and the supratentorial brain substructures are shown in c). d) shows the cerebellum, Circuit of Papez and the supratentorial brain. The slices were chosen to best illustrate the position and volume of each BSCs. Abbreviations: CTV = clinical target volume, LFWM = left frontal white matter, SVZ = subventricular zone

6.2 Monte Carlo simulations

The LET and the dose distributions from variable RBE models were calculated on the planning CT using the FLUKA MC code together with its interface, FLAIR [93, 94]. Through in-house python scripts provided by Fjæra (2016) [95], the treatment plan data was converted into FLUKA-input files. The scoring files from the simulation, which contains the dose and LET_d data, were converted to Digital Imaging and Communications in Medicine (DICOM)-format. The DICOM files were further imported to the Eclipse treatment planning system (Varian Medical Systems, Palo Alto, CA, USA), and the biological dose from the variable RBE models were calculated.

For all of the tissue-dependent models, with the exception of CHD, $(\alpha/\beta)_x$ of both 2 and 3 Gy were applied in order to reflect a probable range of $(\alpha/\beta)_x$ values reported in the brain [6, 7]. For the CHD model, $(\alpha/\beta)_x$ of 1.83 Gy and 8.71 Gy were used, as this model is derived from separate fits to two different cell lines with $(\alpha/\beta)_x$ values corresponding to the two input parameters used. In terms of the non-tissue dependent models, we applied a constant $(\alpha/\beta)_x$ of 3.76 Gy for the WIL model and a constant $(\alpha/\beta)_x$ of 3.33 Gy for the CHE model. The input parameter of 3.76 Gy applied to the WIL model is the ratio of the intermediate value of α_x and β_x in the V79 cell line found by Tilly et al. [96]. An in-house script was used to extract data from dose-volume histograms in Eclipse.

6.3 Model selection

The variable RBE models differ from each other in terms of assumption, regression technique, and database [8]. Key values in the experimental database are found in Table 7.1 along with the abbreviations used in this thesis, whereas the mathematical formulation of each model is shown in Appendix A. A more extensive comparison of the models is found in Rørvik et al. [76]. A set of selection criteria was defined to identify the most suitable models for the endpoint of cognitive impairment to brain tissue while also covering relevant LET values. In addition we set a lower limit for data points used to fit each model. The criteria were:

- Range of radiation fractionation sensitivity $(\alpha/\beta)_x$ data point values covering 2 – 3 Gy, which reflects the probable range in BSCs [6, 7].

- LET_d data point values covering a range up to 20 keV μm^{-1}. The cut-off value mirrors clinically relevant LET_d values.

- > 20 data points in the experimental database.

In order to demonstrate how the range of RBE estimates differed between models fulfilling the selection criteria as compared to the full model collection, all models (summarized in Table 7.1) were also applied to one of the patients. Two additional plan-based models were also used; FRE and UNK.

6.4 Relative biological effectiveness

Discrete RBE values for each structure were calculated by dividing the mean physical dose by the RBE-weighted mean dose from each model. The equation for the dose-weighted mean RBE (RBE_d) is shown below:

$$\mathrm{RBE_d} = \frac{\text{Physical mean dose (Gy)}}{\text{RBE}-\text{weighted mean dose (Gy(RBE))}} \tag{6.1}$$

First, we analyzed the RBE_d across all BSCs for all variable RBE models mentioned in section 4.3.2. This was done for the patient with target volume closest to the median value. We analyzed how the variable RBE models differed in terms of RBE_d value across all BSCs and estimated a potential range of RBE_d within each BSC according to all variable RBE model.

Further, we analyzed RBE_d values with a selected set of models chosen from the method explained in section 6.3. In order to evaluate to which extent the estimated range of RBE_d differed across the selected models and all models, we calculated the range across all BSCs for the selected set of models for the same patient, which all models were applied to. We further applied the selected set of variable RBE models to the full patient cohort and evaluated the differences between patients, BSCs and variable RBE models.

6.5 Cognitive impairment

We investigated the fraction of volume receiving 10 and 40 Gy(RBE) for their association with white matter damage (%V40Gy) and reduction of neural stem cell number (%V10Gy) from data extracted from DVHs [86]. The two dose/volume parameters were first analyzed across all

variable RBE models for the patient with the target volume closest to the median value. Further, we analyzed the dose/volume parameters across all patients for the selected set of models.

6.5.1 Estimated endpoint-specific cognitive decline

The risk of memory impairment was calculated by a model proposed by Blomstrand et al. [97] (Eq. 6.13), which is fitted to odds ratios of memory impairment at different temporal doses published by Armstrong et al. [22]. Toussaint et al. derived the proposed model to better match the function with craniopharyngioma patients [13, 22]. The model calculates the risk of impairment, p_d, using the odds ratio at 10 Gy, OR_{10}, the baseline risk of memory impairment at zero dose, p_o, and the dose to the temporal lobe, d. The values used for OR_{10} and p_o are 1.14 and 0.246, respectively.

Zureick et al. proposed a model for memory impairment after radiation therapy with protons, based on the dose to the left hippocampus [17] (Eq. 6.14). This model correlates the volume of the left hippocampus receiving 20 Gy to delayed verbal memory (DVeM) score at a time, t, after radiation therapy. The covariates (age = 7, sex = female, neurological symptoms at baseline) used in this thesis are the same as in another publication based on the same patient group [13]. These values were set to constant across the whole patient group to observe the specific impact of dose and RBE on the memory score estimates. We calculated the DVeM score 24 months after radiation therapy and compared the score to the baseline value.

6.5.2 Estimated IQ score decline

A total number of ten equations from three publications from Merchant et al. were used to estimate the change in IQ score after radiation therapy treatment (Eq. (6.2 - 6.11) in Table 6.2) [10, 19, 88]. Of these, six models were based on patient age at radiation therapy treatment and fraction of volume of the brain, supratentorial brain, and left temporal lobe receiving doses in low, intermediate, and high dose/volume intervals. The four remaining models were based on the patient age at radiation therapy treatment and the mean doses to the same brain volumes as above. The IQ models were rewritten to estimate the change in IQ compared to the baseline 24 months after radiation therapy treatment.

Merchant et al., hereby referred to as CNS models, developed both dose/volume interval and mean dose IQ score models (Eq. 6.5 – 6.10) [98]. We utilized both approaches and compared

the results. Both 2 - and 3-term equations were suggested for the whole brain and supratentorial dose/volume interval models. The 3-dose-interval models were chosen for this thesis as the high dose-interval was considered to have a significantly more adverse effect than the other intervals.

Three other dose/volume interval models by Merchant et al. were used (Eq. 6.2 – 6.4). These models are hereby referred to as craniopharyngioma models. Also, one model based on the mean dose to the supratentorial brain by Merchant et al. was used to estimate the decline in IQ score (Eq. 6.11). This model is derived from patients receiving proton therapy and is hereby referred to as the craniopharyngioma proton model. The proposed threshold of 13 % of the left temporal lobe volume receiving 43.2 Gy proposed by Jalali et al. was also investigated.

Table 6.2: Models used to estimate cognitive impairment, listed by year of publication. The column to the far right shows the corresponding number of each equation. For equation 6.2 – 6.10, time (t) is measured in months, mean dose is measured in Gy, and the volume terms represent the fraction of volume which receives the dose over the specified interval. For equation 6.14, time (t) is measured in years. Abbreviations: L = left, Temp. = Temporal, Supra = Supratentorial

Reference	**Equation**	**Structure**	**End-point**	**#**
Merchant et al. 2006a	$IQ_{change} = (-0.0044 \text{ x } V_{0-25\text{ Gy}} + 0.0313 \text{ x } V_{25-45\text{ Gy}} - 0.0253 \text{ x } V_{45-60\text{ Gy}}) \text{ x t}$	Brain	IQ decline	(6.2)
	$IQ_{change} = (-0.00401 \text{ x } V_{0-30\text{ Gy}} + 0.0464 \text{ x } V_{30-45\text{ Gy}} - 0.0278 \text{ x } V_{45-60\text{ Gy}}) \text{ x t}$	Supra Brain	IQ decline	(6.3)
	$IQ_{change} = (-0.00415 \text{ x } V_{0-30\text{ Gy}} + 0.0155 \text{ x } V_{30-45\text{ Gy}} - 0.0127 \text{ x } V_{45-60\text{ Gy}}) \text{ x t}$	Temp. Lobe. L	IQ decline	(6.4)
Merchant et al. 2006b	$IQ_{change} = (-0.41\text{x } V_{20-35\text{ Gy}} - 0.43 \text{ x } V_{35-65\text{ Gy}} - 0.36 \text{ x } V_{45-65\text{ Gy}}) \text{ x t}$	Brain	IQ decline	(6.5)
	$IQ_{change} = (-0.38 \text{ x } V_{20-30\text{ Gy}} - 0.31 \text{ x } V_{30-55\text{ Gy}} - 1.37 \text{ x } V_{55-65\text{ Gy}}) \text{ x t}$	Supra Brain	IQ decline	(6.6)
	$IQ_{change} = (-0.40 \text{ x } V_{15-40\text{ Gy}} - 0.44 \text{ x } V_{40-65\text{ Gy}}) \text{ x t}$	Temp. Lobe. L	IQ decline	(6.7)
	$IQ_{change} = (-0.0095 \text{ x Mean Dose}) \text{ x t}$	Brain	IQ decline	(6.8)
	$IQ_{change} = (-0.0091 \text{ x Mean Dose}) \text{ x t}$	Supra Brain	IQ decline	(6.9)
	$IQ_{change} = (-0.0092 \text{ x Mean Dose}) \text{ x t}$	Temp. Lobe. L	IQ decline	(6.10)
Merchant et al. 2008	$IQ_{change} = (-0.0002 \text{ x Mean Dose}) \text{ x t}$	Supra Brain	IQ decline	(6.11)
Jalali et al. 2010	$V43.2\text{ Gy} > 13\ \%$	Temp. Lobe. L	FSIQ decline	(6.12)
Blomstrand et al. 2012	$p_d = \frac{OR_{10}^{\frac{D}{10\text{ Gy}}}}{\left(\frac{1}{p_o} - 1\right) + OR_{10}^{\frac{D}{10\text{ Gy}}}}$	Temp. Lobe. L	Memory impair-ment	(6.13)
Zureick et al. 2018	$DVeM_{change} = 0.05 \text{ x t} - 0.01 \text{ x } V20Gy_{\text{left hippocampus}} - 0.46$	Left hippocampus	Delayed verbal memory	(6.14)

6.5.3 Statistical analysis

In terms of the statistical uncertainties for the FLUKA MC code, the uncertainty decrease with $1/\sqrt{N}$, where N is the number of particles. Each field was simulated separately for every patient, and two simulation cycles with $2.5x10^7$ primaries were used for each subscribed field.

Wilcoxon signed-rank tests for paired samples were used to analyze the relationship between RBE 1.1 and proton RBE models in terms of IQ score. In addition, we evaluated if the different IQ score models within each publication differed significantly from each other. The Wilcoxon signed-rank test is commonly used to compare paired data when the data is not assumed normally distributed [99]. A p-value < 0.05 were considered significant. In order to evaluate statistical significance, the absolute value of the difference between two groups of data from lowest to highest were ranked, where the lowest difference between the values ranks 1. The test statistics, W, is the sum of ranks for positive or negative differences and is given by the equation below:

$$W = \sum_{i=1}^{n} Z_i R_i \tag{6.15}$$

where R_i is the rank and Z_i is an indicator of a positive or negative value. The standard deviation, σ_w, and the mean value of the test statistics, μ_w, are found by the following equations:

$$\sigma_W = \sqrt{\frac{n(n+1)(2n+1)}{24}} \tag{6.16}$$

$$\mu_W = \frac{n(n+1)}{4} \tag{6.17}$$

where n is the total number of observations. For $n \geq 10$, the unit of normal distribution, z, can be calculated directly as seen in the equation below:

$$z = \frac{W-\mu_W}{\sigma_W} \tag{6.18}$$

We further obtained the p-values using a two-tailed test. The equation used for the p-value is shown below:

$$p = 2 \text{ x } (1 - \text{Normal distribution } (|z|)) \tag{6.19}$$

7 Results

Chapter 7.1 shows the results from the model selection method explained in chapter 6.3. Further, chapter 7.2 presents results for the one patient where all RBE models were utilized, and chapter 7.3 presents the results across all ten patients.

7.1 Model selection

Among the eleven phenomenological models, five fulfilled the criterion for data points, four for $(\alpha/\beta)_x$ and five for LET_d, as seen in Table 7.1. Four models (CHE, TIL, WED, WIL) failed on all criteria, whereas two models failed on two (PLR, MAI), and two models (CAR, CHD) failed by one criterion. The two plan-based models, UNK and FRE, were excluded as these are not fitted to in vitro data. The models selected for further calculations of risk of cognitive impairment, still accounting for variable biological effectiveness, were the models by ROR, MCN, and JON. The weighted version (RORW) of the ROR models was chosen for the set of models as experiments of high quality are weighted more in regression analysis.

Table 7.1: Overview of data point values in experimental databases used to fit the variable RBE models along with model dependencies. Cut-off values of the criteria are given in parenthesis. Numbers in bold green fall within the cut-off values.

Models	**Abbre-viation**	**Data points (> 20)**	**$(\alpha/\beta)_x$ range [Gy] (2 – 3)**	**LET_d range [keV µm^{-1}] (Up to 20)**	**Depend -encies**
Carabe et al (2012) [74]	**CAR**	**44**	2.0 – 2.8	**1.0 – 20.0**	LET_d, $(\alpha/\beta)_x$
Chaudary et al (2014) [64]	**CHD**	12	**1.8 – 22.7**	**1.1 – 25.9**	LET_d, $(\alpha/\beta)_x$
Chen and Ahmad (2012) [65]	**CHE**	14	2.2 – 2.8	7.7 – 37.8	LET_d
Jones (2015) [67]	**JON**	**28**	**0.5 - ∞**	**0.5 - 33-0**	LET_d, α_x, β_x
Mairani et al (2017) [75]	**MAI**	**25**	7.7 – 37.8	2.7-69.5	LET_d, $(\alpha/\beta)_x$
McNamara et al (2015) [71]	**MCN**	**285**	**0.1 – 29.5**	**0.2 – 20.0**	LET_d, $(\alpha/\beta)_x$
Peeler (2016) [68]	**PLR**	**48**	2.6 – 5.1	0.9 – 19.0	LET_d, $(\alpha/\beta)_x$
Rørvik et al (2017) [66]	**RORW/RORUW**	**85**	**1.2 – 18.4**	**0.4 – 37.8**	d(L), $(\alpha/\beta)_x/LET_d$, $(\alpha/\beta)_x$
Tilly et al (2005) [69]	**TIL**	7	2.7 – 2.8	7.7 – 20.0	LET_d, $(\alpha/\beta)_x$
Wedenberg et al (2013) [70]	**WED**	19	2.7 – 69.5	7.7 – 30.0	LET_d, $(\alpha/\beta)_x$
Wilkens and Oelfke (2004)[73]	**WIL**	19	2.1 – 3.7	2.3 - 30	LET_d

7.2 Relative biological effectiveness and dose/volume parameter estimation across all models

Across the thirteen different variable RBE models, there were significant variations in RBE-weighted doses and RBE in the BSCs in the selected patient, as seen in Figure 7.1. The large variations can also be seen in Figure 7.2, where RBE distribution for all variable RBE models is shown. Only the PLR model estimated RBE_d to be less than 1.1 consistently across all BSCs. All BSCs considered, the lowest (1.14) and highest (1.65) median RBE_d across all variable RBE models were observed for the left parietal lobe and cerebellum, respectively. The corresponding RBE_d ranges across all models were 0.82 – 1.29 for the left parietal lobe and 0.85 – 2.26 for the cerebellum structure. The CHE model provided the highest values of RBE_d across all structures apart from the cerebellum, parietal lobes, and left hippocampus tail, where the unweighted version of the ROR model provided the highest values. The model by PLR systematically resulted in the lowest RBE_d values.

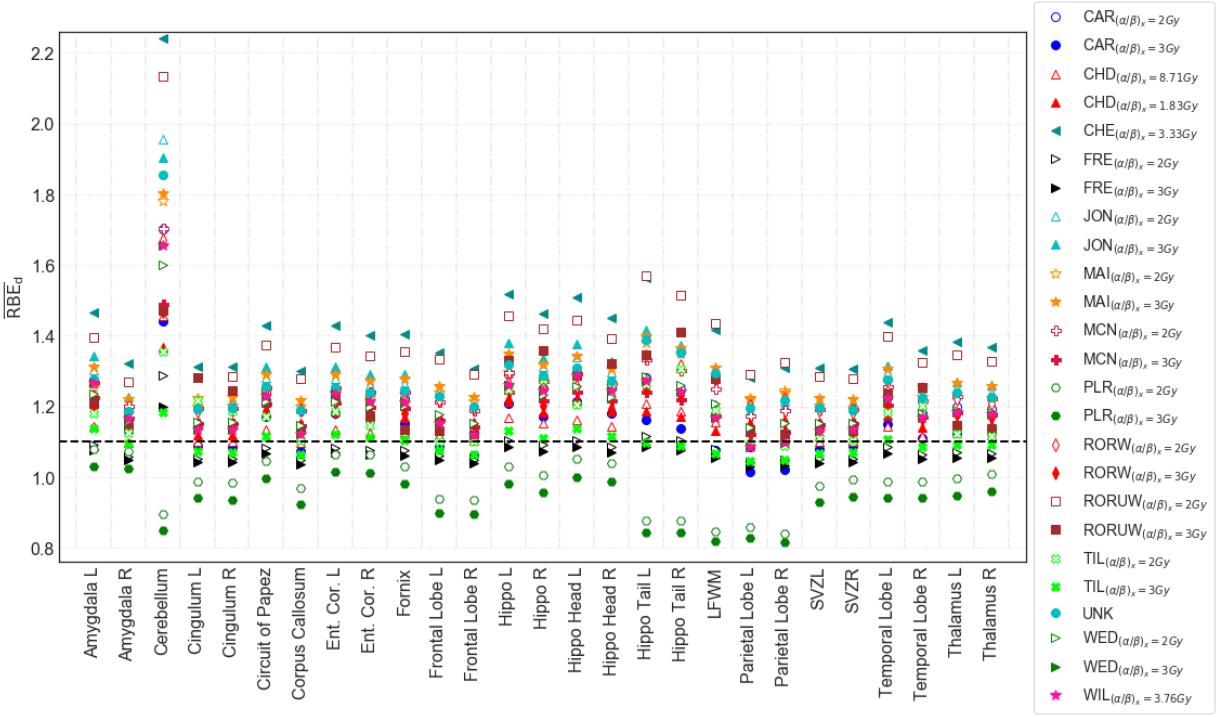

Figure 7.1: Scatter plot of the calculated RBE_d of the analyzed BSCs across all models. The horizontal solid line shows RBE of 1.1. Open and closed symbols indicate $(\alpha/\beta)_x$ of 2 and 3 Gy, respectively. Abbreviations: Ent. Cor. = Entorhinal Cortex, L = left, R = right, LFWM = Left frontal white matter, Hippo = Hippocampus, SVZ = Subventricular zone

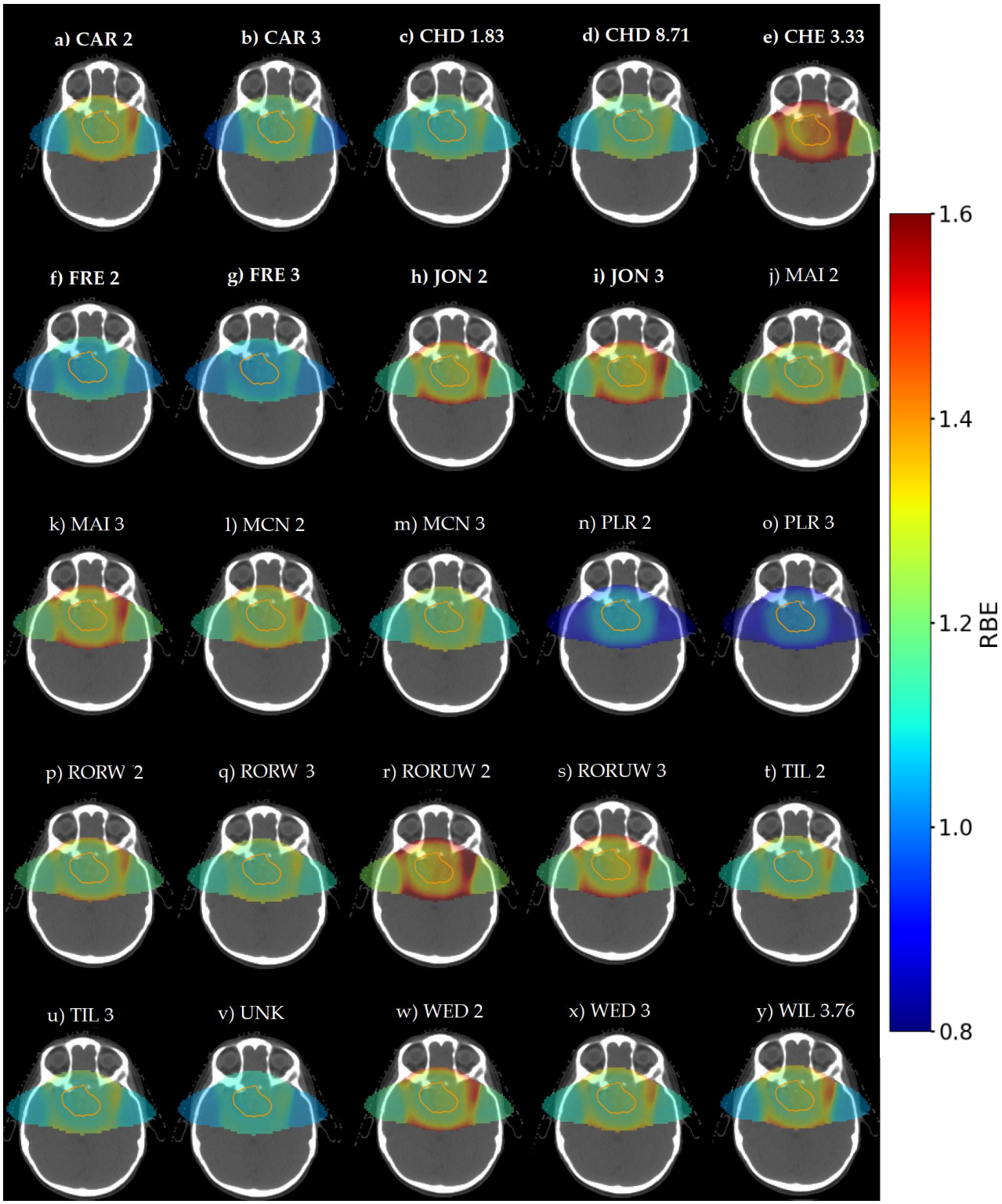

Figure 7.2: RBE distribution for all variable RBE model used in the thesis. The number following each model represents the input parameter of $(\alpha/\beta)_x$. The orange delineated structure is the CTV.

All RBE_d values within each structure subgroup for all variable RBE models for the selected patients are included in Appendix B. In Figure 7.3, the LET_d for the selected patient is shown along with delineation of the temporal lobes. The temporal lobe substructures resulted in a higher median RBE_d than the supratentorial and ventricular substructures for all variable RBE models. Table 7.2 presents median RBE_d across all BSCs and median RBE_d within each structure subgroup for all variable RBE models. As seen in Table 7.2, three models (PLR, FRE, and UNK) estimated a lower median RBE_d across all BSCs than 1.1.

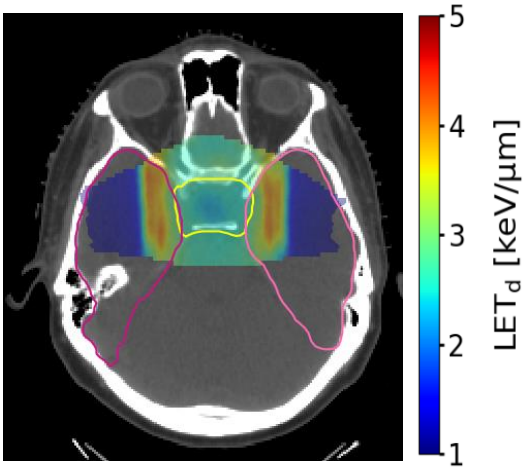

Figure 7.3: LET_d distributions for the patient with target volume closest to the median value. The delineated volumes are CTV (yellow) and temporal lobes (pink).

Table 7.2: Median RBE_d across all BSCs (second column) and median RBE_d values with range in brackets across different structure subgroups (three columns to the far right). The models are arranged by ascending order by median RBE_d across all BSCs. For the tissue-dependent models, both input parameters have been analyzed. Numbers in bold green shows RBE_d values for the three selected models.

Models	Median across all BSCs	Supratentorial substructures	Ventricular substructures	Temporal lobe substructures
PLR	0.96 [0.81 – 1.08]	0.93 [0.81 – 1.01]	0.97 [0.92 – 1.03]	1.01 [0.84 – 1.08]
FRE	1.07 [1.02 – 1.37]	1.05 [1.03 – 1.08]	1.05 [1.04 – 1.08]	1.08 [1.05 – 1.12]
UNK	1.09 [1.04 – 1.22]	1.08 [1.05 – 1.11]	1.11 [1.10 – 1.17]	1.11 [1.09 – 1.14]
CHD	1.14 [1.09 – 1.59]	1.12 [1.10 – 1.22]	1.11 [1.10 – 1.17]	1.17 [1.11 – 1.22]
TIL	1.16 [1.08 – 1.41]	1.13 [1.09 – 1.28]	1.14 [1.10 – 1.23]	1.21 [1.13 – 1.36]
CAR	1.17 [1.01 – 1.91]	1.13 [1.01 – 1.23]	1.14 [1.07 – 1.22]	1.21 [1.14 – 1.29]
WIL	1.20 [1.09 – 1.84]	1.17 [1.09 – 1.22]	1.13 [1.12 – 1.21]	1.24 [1.16 – 1.29]
RORW	**1.20 [1.14 – 1.83]**	**1.20 [1.15 – 1.28]**	**1.18 [1.15 – 1.22]**	**1.22 [1.14 – 1.34]**
MCN	**1.21 [1.12 – 1.90]**	**1.18 [1.12 – 1.26]**	**1.19 [1.15 – 1.24]**	**1.24 [1.17 – 1.33]**
WED	1.24 [1.14 – 2.09]	1.20 [1.14 – 1.29]	1.19 [1.16 – 1.24]	1.26 [1.16 – 1.39]
MAI	1.26 [1.18 – 2.01]	1.24 [1.21 – 1.31]	1.22 [1.20 – 1.28]	1.29 [1.18 – 1.40]
JON	**1.27 [1.18 – 2.23]**	**1.24 [1.18 – 1.31]**	**1.21 [1.19 – 1.29]**	**1.33 [1.20 – 1.42]**
RORUW	1.32 [1.21 – 2.43]	1.32 [1.21 – 1.43]	1.28 [1.22 – 1.35]	1.38 [1.23 – 1.57]
CHE	1.40 [1.28 – 2.46]	1.36 [1.28 - 1.44]	1.31 [1.30 – 1.40]	1.46 [1.32 – 1.56]

In terms of the three selected models (JON, MCN, and RORW), the JON model provided the highest median RBE_d value, whereas RORW resulted in the lowest for the selected patient. As seen in Figure 7.4, the estimated RBE_d range across the investigated structures from the three selected models was narrower and thereby more consistent as compared to the RBE_d estimates from the excluded models. The median RBE_d (range in brackets) across all models and structures for the one patient was 1.20 [0.81, 2.61], whereas it was 1.22 [1.12, 2.23] for the selected set of models.

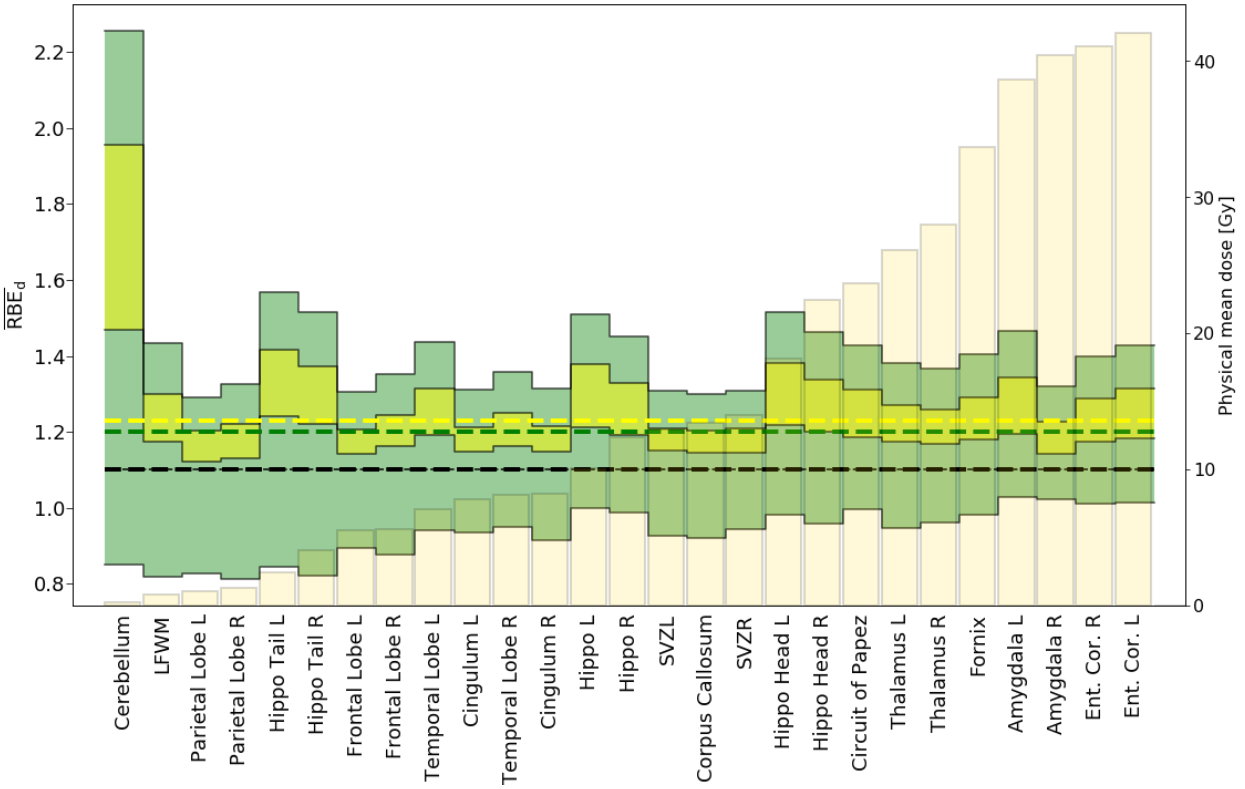

Figure 7.4: Illustration of minimum and maximum RBE_d values for all models (filled green) and the selected set of models (filled yellow) calculated for the patient with target volume closest to the median value. Both input parameters of $(\alpha/\beta)_x$ were applied to the tissue-dependent models. The beige bars show the physical mean dose of each structure. Black dashed line show RBE 1.1, and the two other dashed lines show median values across all structures for all models (green) and the selected set (yellow). Abbreviations: Ent. Cor. = Entorhinal Cortex, L = left, R = right, LFWM = Left frontal white matter, Hippo = Hippocampus, SVZ = Subventricular zone

Following the results for the RBE_d estimates, large variations were also seen in the dose/volume parameter (%V10Gy and %V40Gy). Figure 7.5 shows DVH for the left hippocampus head for all variable models for the selected patient. Estimates for the left hippocampus head resulted in the most extensive range across all variable RBE models in %V40 Gy(RBE) [38 – 90%]. The corpus callosum showed the largest range across all models in %V10 Gy(RBE) [42 – 65%].

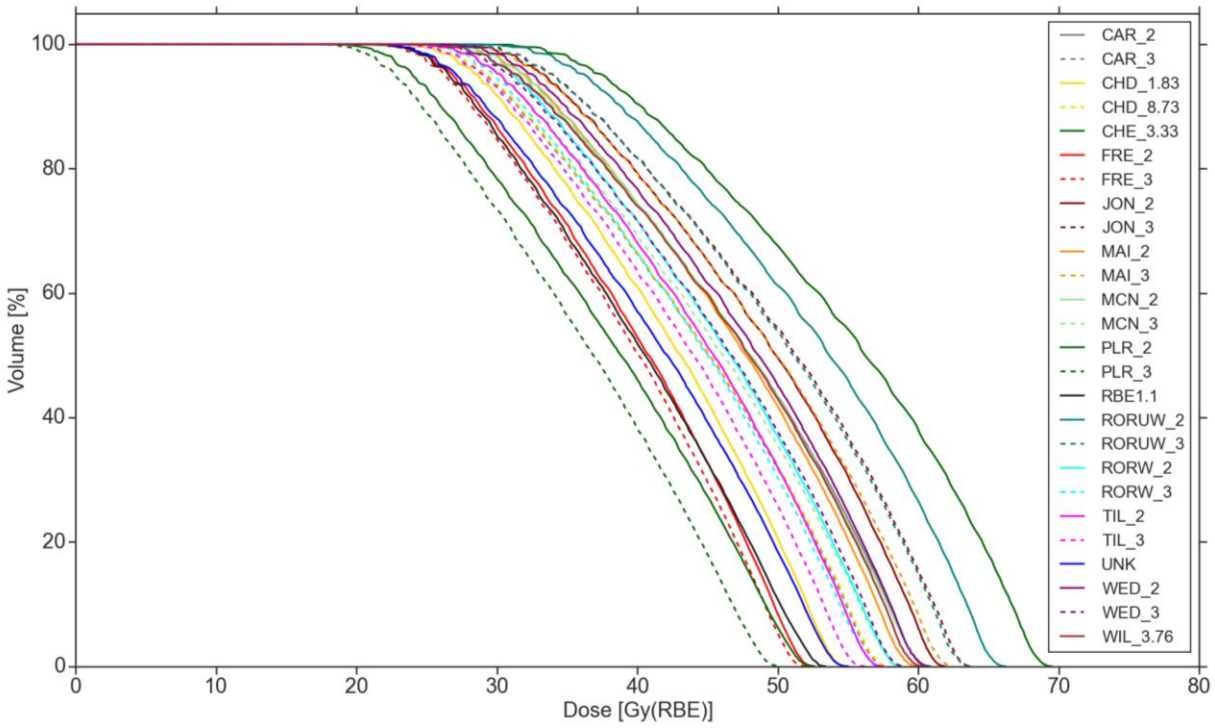

Figure 7.5: DVH of the left hippocampus head, which showed the largest difference across all models for %V40Gy(RBE). The number following each model represents the input parameter of $(\alpha/\beta)_x$. Solid and dashed lines indicate $(\alpha/\beta)_x$ of 2 and 3 Gy, respectively. The non-tissue dependent models are all represented by solid lines.

Figure 7.6 presents the fraction of BSC volume receiving 10 and 40 Gy(RBE). Interestingly, the RORUW model presented the highest volumes receiving 10 Gy(RBE) for all structures, whereas the CHE model provided the highest RBE_d values and highest volume receiving 40 Gy(RBE) across all structures. PLR systematically resulted in the lowest values for both %V10Gy(RBE) and %V40Gy(RBE).

Figure 7.6: Fraction of BSC volume receiving 10 Gy(RBE) (upper) and 40 Gy(RBE) (lower) across all variable RBE models used in this thesis. The number following each model represents the input parameter of $(\alpha/\beta)_x$. Abbreviations: Ent. Cor. = Entorhinal Cortex, L = left, R = right, LFWM = Left frontal white matter, Hippo = Hippocampus, SVZ = Subventricular zone

7.3 Results across the selected set of models

7.3.1 Relative biological effectiveness and dose/volume parameter estimation across the selected set of models

Considering only the selected models (JON, MCN and RORW), the estimated RBE_d range across all the studied BSCs and patients was 1.11 - 3.31. RBE_d values across both input parameters of $(\alpha/\beta)_x$ (2 and 3 Gy) for each model along with the median physical dose across all patients are presented in Figure 7.7. The JON model estimated the highest median RBE_d at 1.30 [1.15 – 3.31] across all structures and patients, whereas the RORW and MCN models resulted in median values of 1.22 [1.12 – 2.46] and 1.23 [1.11 – 2.62], respectively.

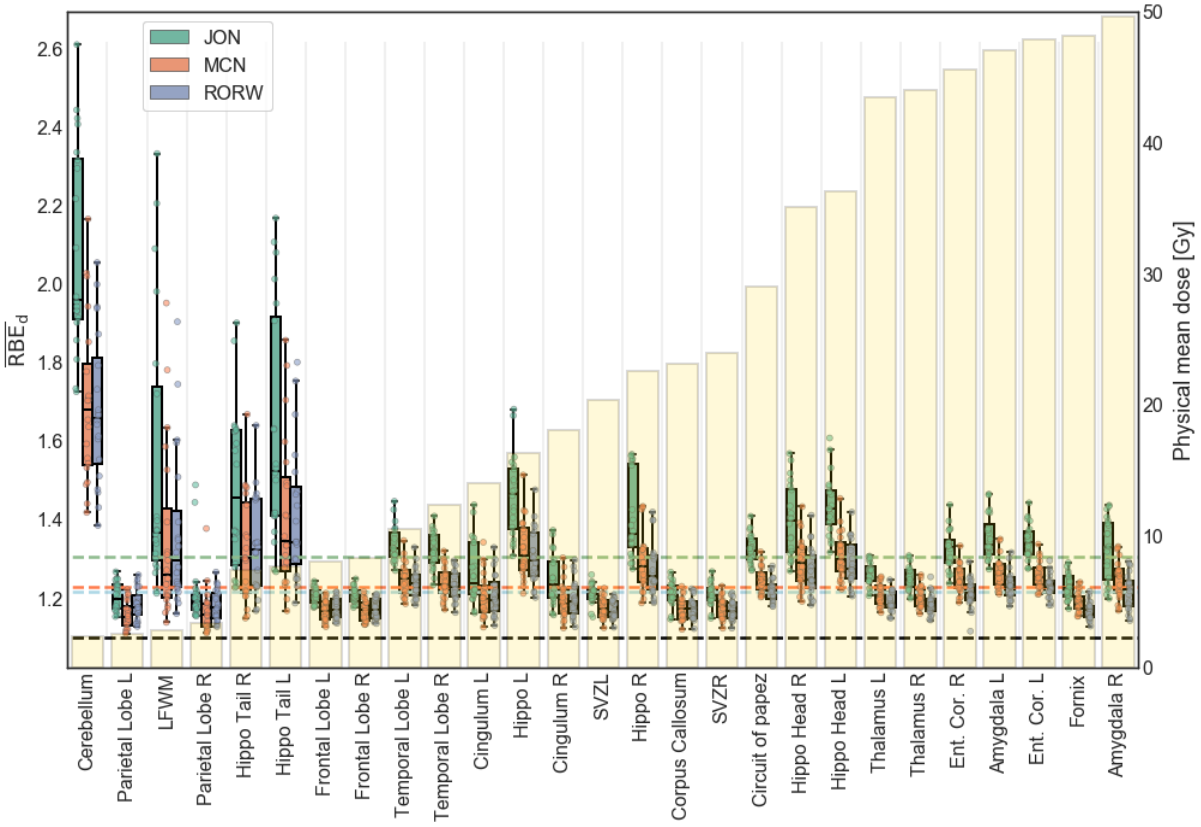

Figure 7.7: RBE_d values of the studied BSCs, arranged in ascending order by the median physical mean dose (yellow bars) across all patients and both input parameters of $(\alpha/\beta)_x$. The horizontal dashed lines represents the median values for JON (green), MCN (red) and RORW (blue) across all BSCs. The box attaches the inner two quartiles, while the line in the middle of the box represents the median value to each BSC. Abbreviations Ent. Cor. = Entorhinal Cortex, L = left, R = right, LFWM = Left frontal white matter, Hippo = Hippocampus, SVZ = Subventricular zone

Following the results from all models, estimates of the cerebellum structure resulted in the highest median RBE_d value of 1.79 [1.39 – 2.61] across all patients also for the selected models. As seen in the previous figure (Fig. 7.7), the cerebellum structure were, however, exposed to low physical doses. The estimated median RBE_d for the anterior part of the cerebellum was 1.69 [1.36 – 2.48], whereas the median RBE_d for the posterior part was 2.11 [1.56 – 3.31] across the selected models. The structure with the lowest range across all patients for the selected set of models was the right frontal lobe, with RBE_d ranging from 1.14 – 1.25. Compared to other BSCs, the estimated RBE_d were low for both the frontal and parietal lobes.

A comparison of the RBE distributions for $(\alpha/\beta)_x$ of both 2 and 3 Gy for JON, MCN and RORW is shown in Figure 7.8. As seen in this figure, RORW and MCN resulted in higher RBE with decreasing $(\alpha/\beta)_x$, whereas the opposite trend was shown for JON. Across the three selected models, the median RBE_d was 1.26 [1.41, 3.11] and 1.22 [1.11, 3.11] for $(\alpha/\beta)_x$ of 2 and 3 Gy, respectively.

The estimated RBE_d for both $(\alpha/\beta)_x$ of 2 and 3 Gy across all BSCs are presented in Figure 7.9. As seen in this figure, the difference in RBE_d values from the two $(\alpha/\beta)_x$ input parameters was less prominent for the JON model than for RORW and MCN. Across all BSCs for the full patient cohort, the JON model estimated a median value of 1.29 [1.15, 3.31] and 1.31 [1.16, 3.1] for $(\alpha/\beta)_x$ of 2 and 3 Gy, respectively. The difference in the median value was larger for MCN and RORW, as seen in Figure 7.9. For the MCN model, the estimated median value was 1.26 [1.15, 2.62] for 2 Gy and 1.20 [1.11, 2.11] for 3 Gy as input parameter of $(\alpha/\beta)_x$. For RORW, the estimated median value was 1.24 [1.15, 2.46] and 1.19 [1.11, 2.01] for $(\alpha/\beta)_x$ of 2 and 3 Gy, respectively.

The estimated RBE_d range between $(\alpha/\beta)_x$ of 2 Gy and 3 Gy for MCN and RORW appeared to be lower for BSCs generally exposed to high dose levels, e.g., amygdala, thalamus, and entorhinal cortex, whereas the model by JON showed the opposite trend.

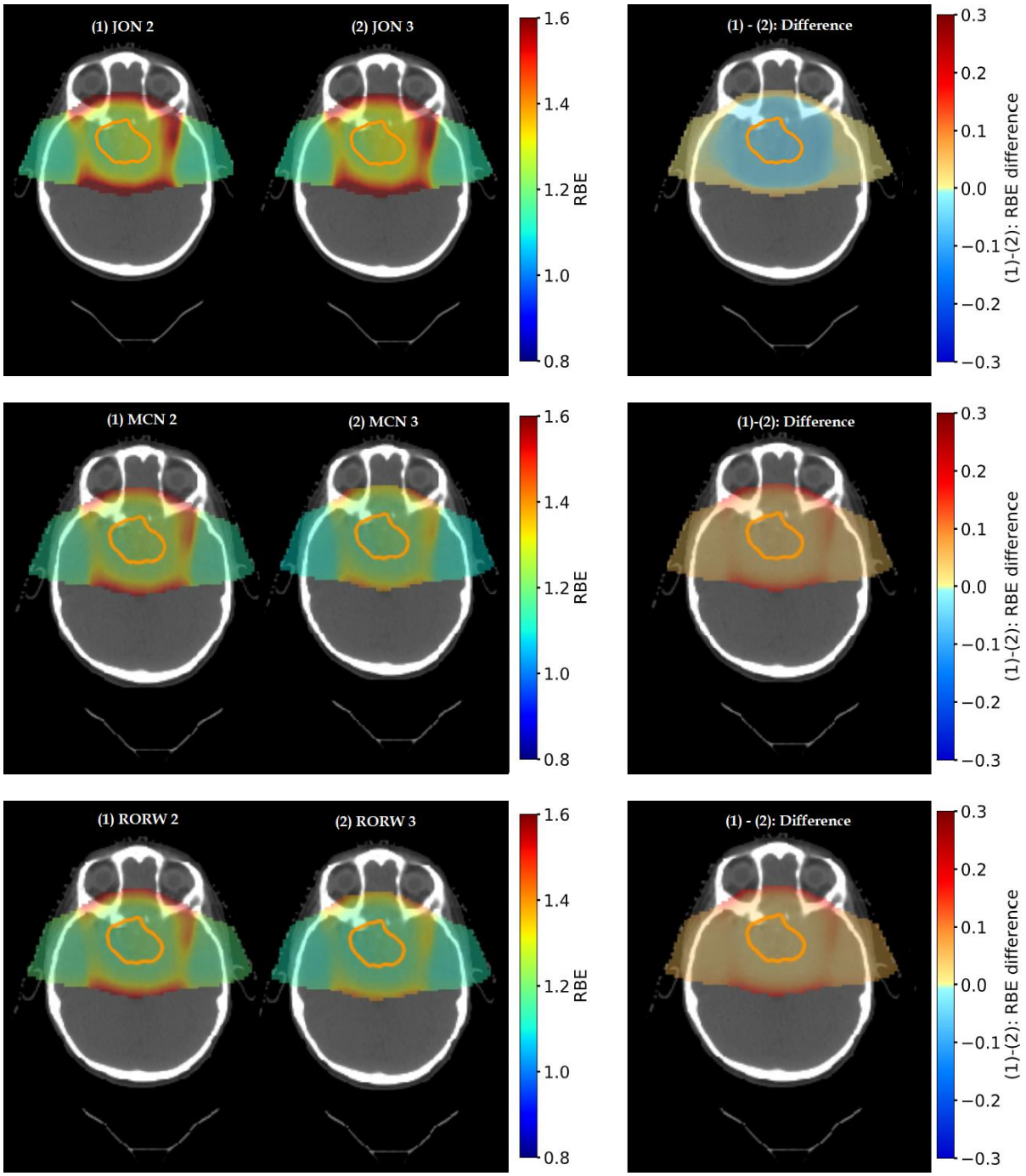

Figure 7.8: RBE distributions for the models by RORW (a), MCN (b), and JON (c) with both $(\alpha/\beta)_x$ of 2 (left) and 3 Gy (middle) as input parameter. The column to the right illustrates the difference in RBE distribution between the two input parameters. CTV is shown in orange.

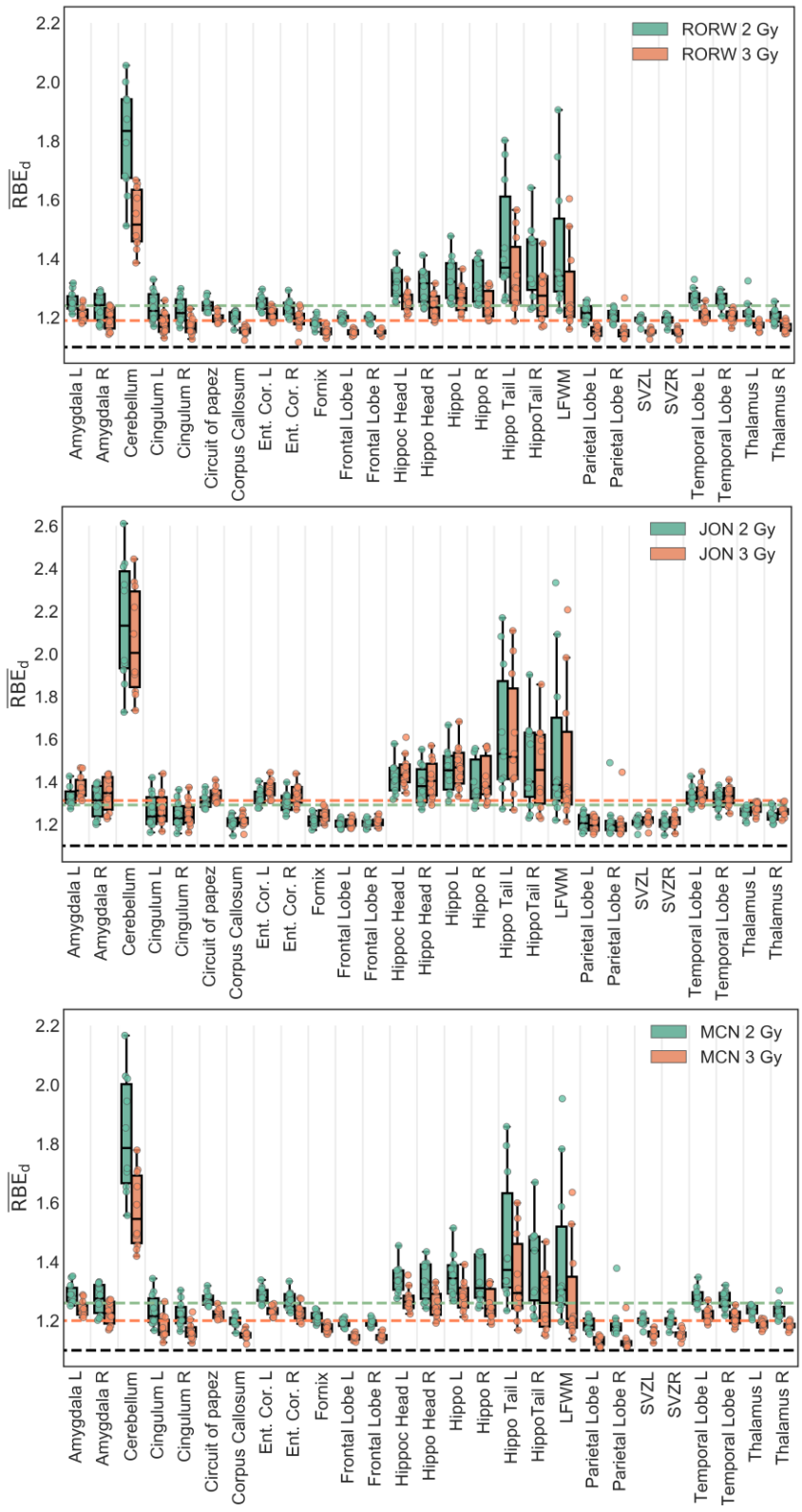

Figure 7.9: RBE_d values of the studied BSCs for the two input parameters of $(\alpha/\beta)_x$ for the RORW (upper), JON (middle) and MCN (lower) models. Green boxes and points indicate $(\alpha/\beta)_x$ of 2 Gy, whereas the red boxes and points indicate $(\alpha/\beta)_x$ of 3 Gy. The horizontal dashed lines represent the median value for $(\alpha/\beta)_x$ of 2 (green) and 3 Gy (red) across all BSCs, and the black horizontal dashed line represents RBE 1.1. The box attaches the inner two quartiles, while the line in the middle of the box represents the median value to each BSC. Abbreviations: Ent. Cor. = Entorhinal Cortex, L = left, R = right, LFWM = Left frontal white matter, Hippo = Hippocampus, SVZ = Subventricular zone

A comparison of the calculated RBE_d values within each structure subgroups are presented in Figure 7.10 & 7.11. Figure 7.10 also shows the inter-patient differences between the estimated RBE_d values. As seen in Figure 7.10, JON provided the highest values for the RBE_d across all structures and patients except the parietal lobes, where the model by RORW provided the highest values for some patients. JON estimated higher RBE_d values with an $(\alpha/\beta)_x$ of 2 Gy compared to 3 Gy for this structure. For the JON model, this trend only appeared for the parietal lobes and some patient cases in the cingulum structure.

Among the supratentorial structures, the highest RBE_d values were found in the temporal lobes, with a median RBE_d across the selected set of models of 1.27 [1.18 – 1.45] and 1.26 [1.16 – 1.41] for the left and right, respectively. Compared to the parietal and frontal lobes, estimates for the thalamus structure resulted in high RBE_d values with a median value of 1.22 [1.15 – 1.31] (left) and 1.20 [1.14 – 1.31] (right).

As seen in Figure 7.11, all the selected models estimated high RBE_d values for the temporal lobe BSCs when compared to the other structure subgroups. The amygdala and entorhinal cortex were in addition exposed to the high physical dose. The highest RBE_d values were found in the hippocampus structures, where estimates of RBE_d for the left hippocampus tail resulted in a median value of 1.41 [1.17 – 2.21] across all patients.

Estimates of the RBE_d for the left and right cingulum resulted in the highest RBE_d amid the ventricular substructures, with median values of 1.21 [1.13 – 1.44] and 1.20 [1.12 – 1.37], respectively.

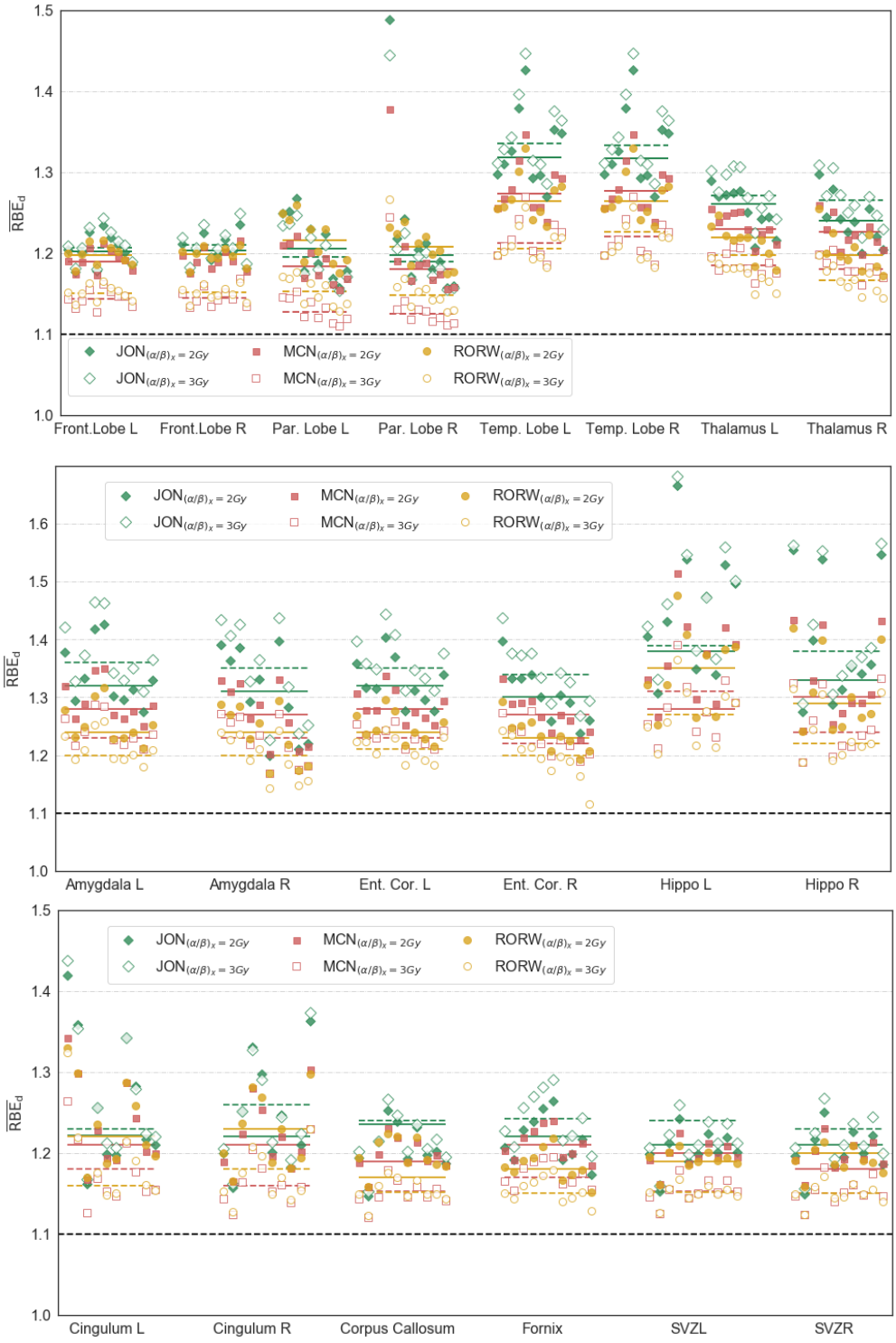

Figure 7.10: RBE_d values for the selected set of models for the supratentorial brain substructures (upper), temporal lobe substructures (middle) and ventricular substructures (lower). The black horizontal dashed line show RBE 1.1. Horizontal lines associated to each structure shows the median value across all patients of the RBE_d from selected models, with solid lines representing $(\alpha/\beta)_x$ = 2 Gy and dashed line shows $(\alpha/\beta)_x$ = 3 Gy. Green lines show median values of JON, yellow lines illustrate the median values of ROR and median values from the MCN model are shown in red. Patients are sorted in ascending order by CTV volume. Abbreviations: Ent. Cor. = Entorhinal Cortex, Front = Frontal, L = left, R = right, Par = Parietal, Temp = Temporal, SVZ = Subventricular zone.

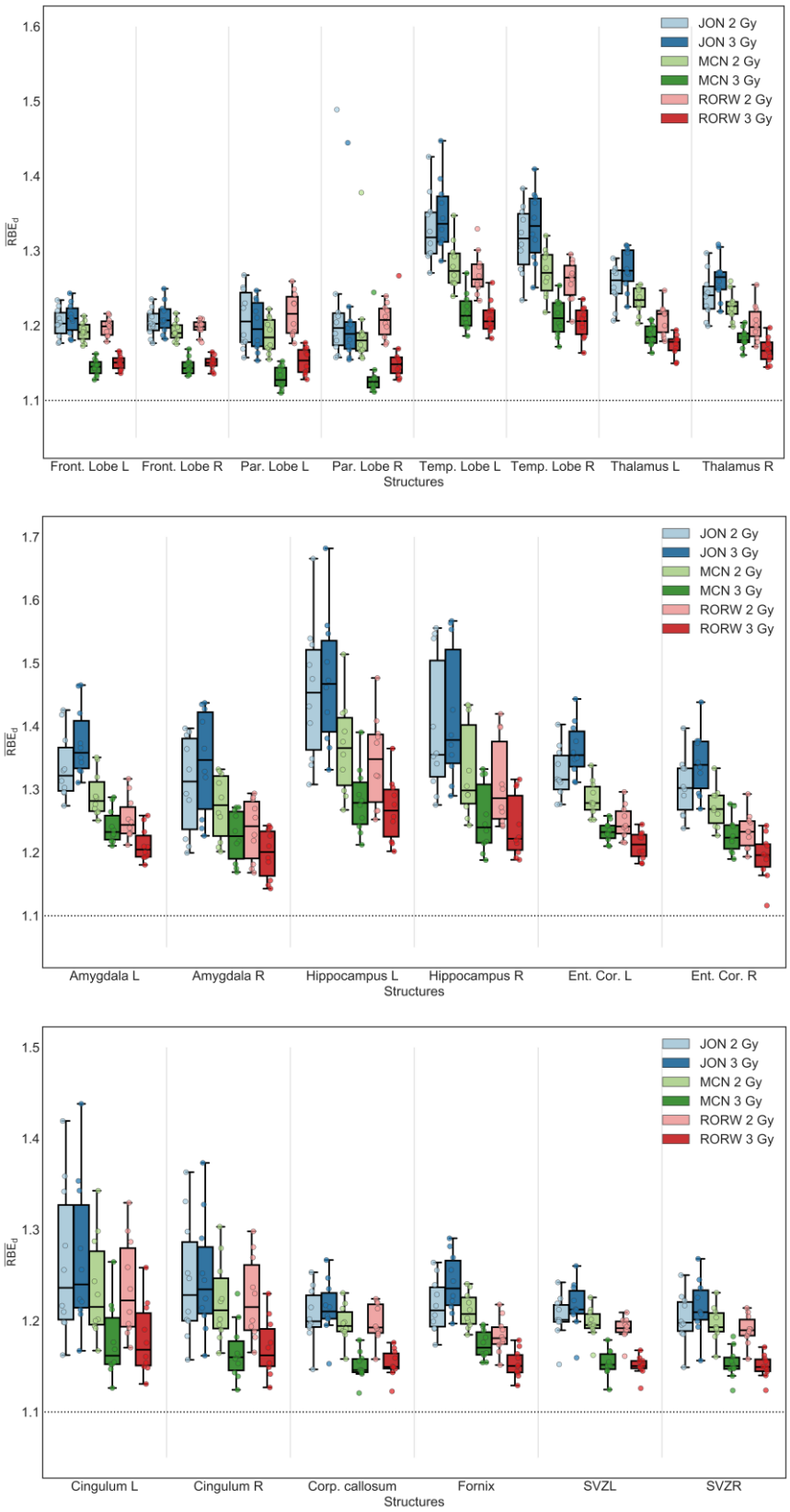

Figure 7.11: RBE_d values for the selected set of models in the supratentorial substructures (upper), temporal lobe substructures (middle), and ventricular substructures (lower). The box attaches the inner two quartiles, while the line in the middle of the box represents the median value. Abbreviations: Corp. = Corpus, Ent. Cor. = Entorhinal Cortex, Front = Frontal, L = left, R = right, Par = Parietal, Temp = Temporal, SVZ = Subventricular zone.

Figure 7.12 shows a DVH of the right thalamus. Estimates for the thalamus resulted in the highest variation between all patients for the studied dose/volume parameters, all models considered. Across all patients, the estimated range for the right thalamus was 41% - 100 and 2% – 93% for %V10Gy(RBE) and %V40Gy(RBE), respectively.

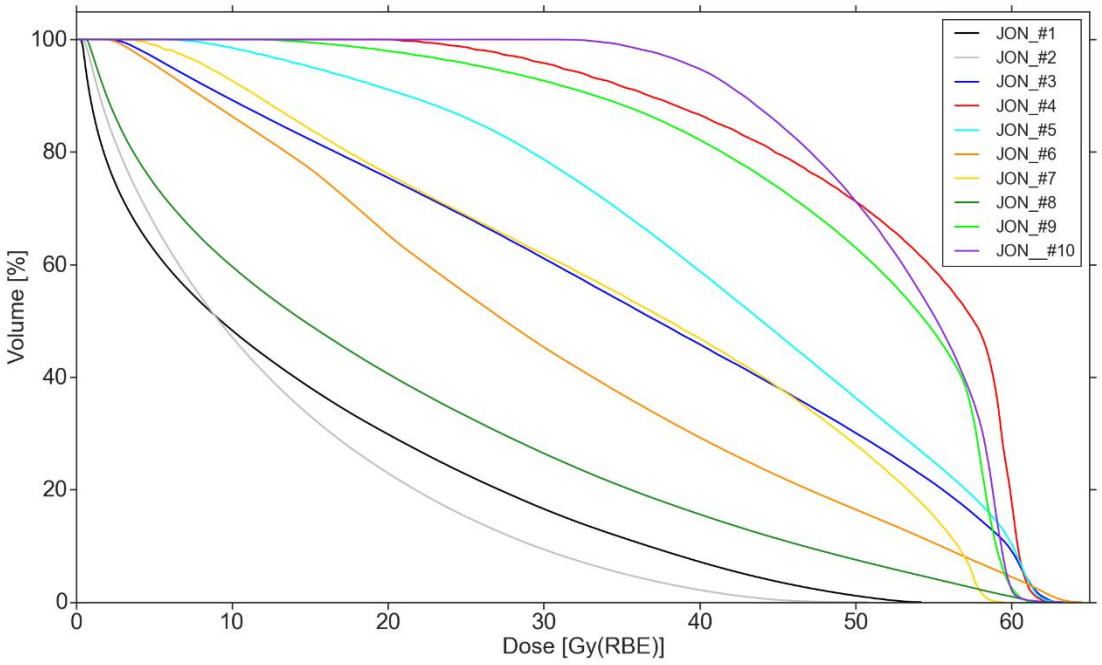

Figure 7.12: DVH of the right thalamus for the full patient cohort for the JON model with 2 Gy as input parameter of $(\alpha/\beta)_x$, illustrating the large inter-patient differences found for %V10 and %V40 Gy(RBE) for this structure. The patients are sorted in ascending order by CTV, and the number following the model name in the legend indicates the patient number.

The estimated range in dose/volume parameters was considerably narrower for the set of models within each patient compared to the range across all models; however, considerable variations were seen between patients, as seen in Figure 7.13 & 7.14. Median value and corresponding range across all patients for the two dose/volume parameters for the set of models are presented in Appendix C. As with the RBE_d calculation, the RORW model led to the highest median values of %V10Gy(RBE) for the parietal lobes. None of the models from the selected set presented a lower volume than the RBE-weighted dose of 1.1 for any of the structures within the two studied dose/volume parameters. Especially for the %V40Gy(RBE) parameter, the variable RBE models resulted in considerably higher volumes than RBE-weighted dose of 1.1. In terms of target volume dependency, a higher volume of the BSCs receiving 10 and 40 Gy(RBE) was generally observed in patients with large target volume. The correlation coefficient of median volume across all structures for %V10Gy(RBE) and %V40Gy(RBE) was 0.77 and 0.79, respectively.

Figure 7.13: Fraction of BSC volume receiving 10 Gy(RBE) across the selected set of variable RBE models for the full patient cohort. The number following each model represents the input parameter of $(\alpha/\beta)_x$. The number to the far left shows the patient number. The patients are sorted in ascending order by CTV volume. Abbreviations: L = left, R = right, Ent. Cor. = Entorhinal Cortex, Hippo = Hippocampus, LFWM = Left frontal white matter, SVZ = Subventricular zone

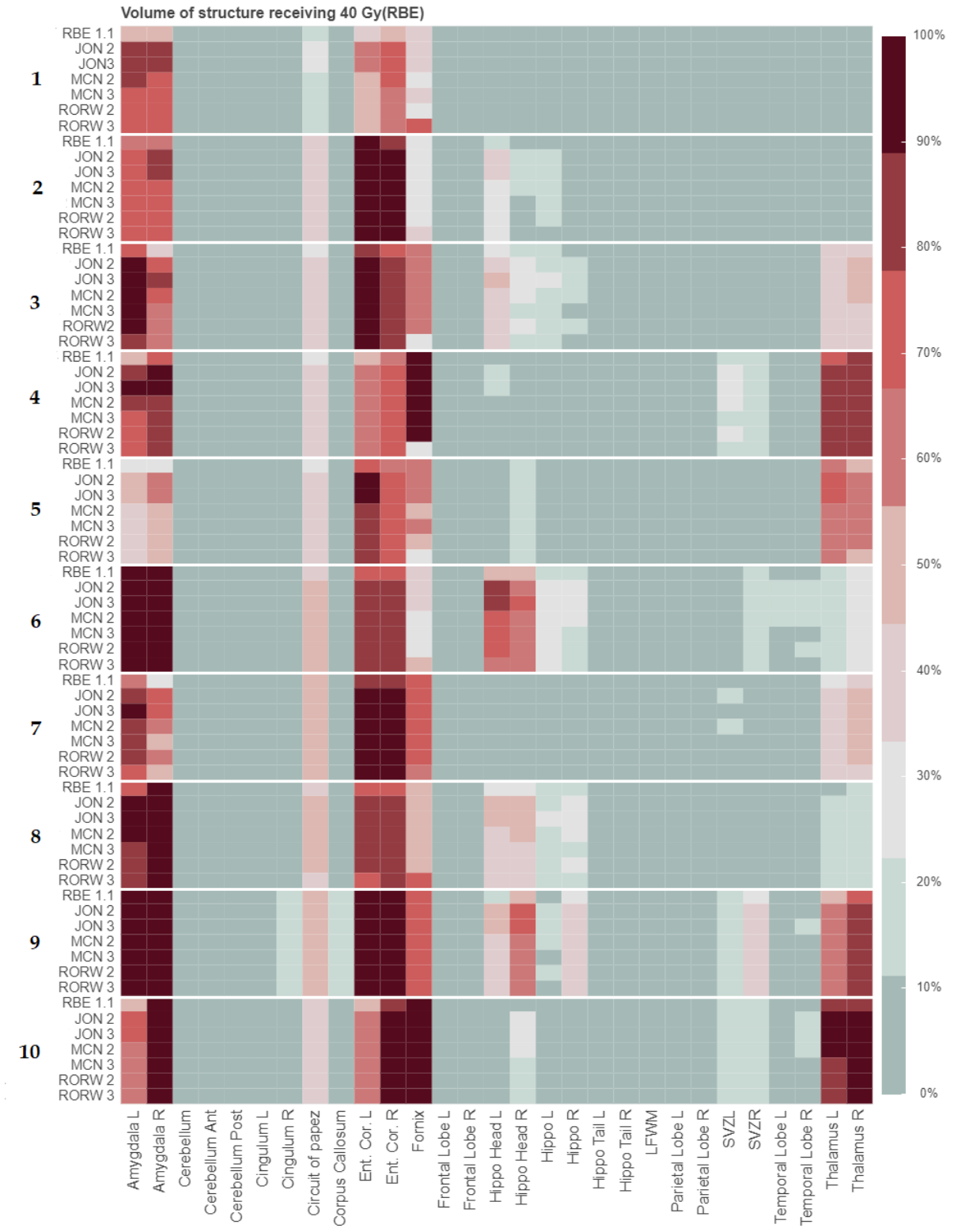

Figure 7.14: Fraction of BSC volume receiving 40 Gy(RBE) across the selected set of variable RBE models for the full patient cohort. The number following each model represents the input parameter of $(\alpha/\beta)_x$. The number to the far left shows the patient number. The patients are sorted in ascending order by CTV volume. Abbreviations: L = left, R = right, Ent. Cor. = Entorhinal Cortex, Hippo = Hippocampus, LFWM = Left frontal white matter, SVZ = Subventricular zone

7.3.2 Estimated cognitive impairment

The current sub-chapter will present the results of the estimated cognitive impairment. The results are summarized in Table 7.3, whereas discrete values are found in Appendix D. In general, variable RBE models which led to the highest values of $RBE_{d,}$ also reported a higher estimated IQ score decline, a higher decline in DVeM score and a higher risk of memory impairment compared to RBE 1.1. DVHs comparing the different variable RBE models to RBE 1.1 for the brain volumes used to estimate cognitive impairment are shown in Figure 7.15.

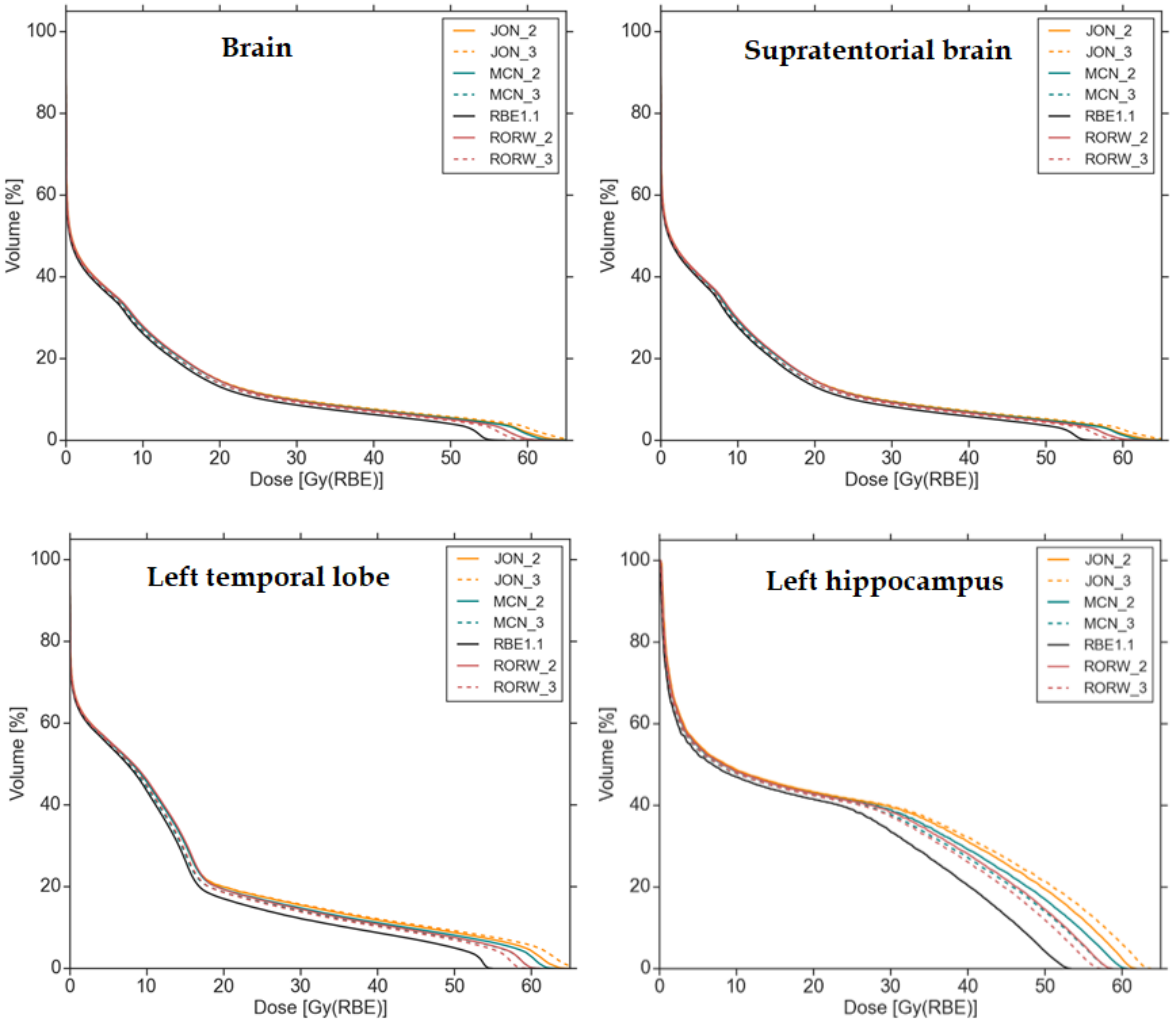

Figure 7.15: DVHs of the brain volumes used to estimate cognitive impairment for the patient with a target volume closest to the median value. Solid and dashed lines indicate $(\alpha/\beta)_x$ of 2 and 3 Gy, respectively. The numbers following each input parameter represent input parameter of $(\alpha/\beta)_x$.

All utilized IQ models estimated a decline in IQ scores, as seen in Figure 7.16 & 7.17. However, the results varied significantly across the models from the three different publications. At 24 months after radiation therapy, the median and range across all IQ score models for the set of proton RBE models was -1.7 [-10, 0.0]. For each variable RBE model, the median was -1.9 [-9.3, 0.0] for JON, -1.8 [-9.9, 0] for RORW, and -1.8 [-10, 0.0] for MCN. For RBE 1.1, the median was -1.6 [-9.5, 0.0]. The craniopharyngioma proton model indicated the lowest values in IQ change of the IQ models. The estimated IQ score change was close to zero across all the selected proton RBE models and RBE 1.1 for all patients.

The median IQ score change across all CNS models (Eq. 6.5 – 6.10) was -1.6 [-3.4, -0.7] considering all the selected variable RBE models (Fig. 7.16). Interestingly, the CNS models presented significantly different results for the two IQ estimate approaches (mean dose and dose/volume interval) for RBE 1.1. When comparing the two approaches across the selected models, a significant difference was seen for the brain and left temporal lobe volume, whereas the difference in the supratentorial brain volume model was not significant at the $p = 0.05$ level for any of the variable RBE models. Overall, the median value of the IQ score decline was lower with the dose/volume interval models. Across all variable RBE models, the median value of the change in IQ score was -1.5 [-3.4, -0.7] for the dose/volume interval models, whereas the mean dose models resulted in the median value of -1.7 [-3.1, -1.2].

Common for all CNS models was that RBE 1.1 consistently estimated lower IQ score decline than the selection of RBE models, as seen in Figure 7.16. Median across all models for the supratentorial model was -1.7 [-2.6, -1.2], -1.9 [-3.1, -1.2] for the left temporal lobe and -1.7 [-2.6, -1.2] for the brain volume. When comparing RBE 1.1 with the selected set of models, the largest differences were seen for the supratentorial brain dose/volume interval model. For this brain volume, the median value was -0.9 [-1.8, -0.6] for RBE 1.1, and -1.7 [-3.4, -1.0] for the selected variable proton RBE models. In terms of target volume-dependency, patients with a large target volume tended to be more vulnerable to IQ decline scores for the brain – and supratentorial brain model, which can be observed in Figure 7.16. In terms of the two input parameters, the patterns were comparable to those presented in the previous section; a higher input parameter of $(\alpha/\beta)_x$ led to a higher decline in IQ score for MCN and RORW for the CNS models.

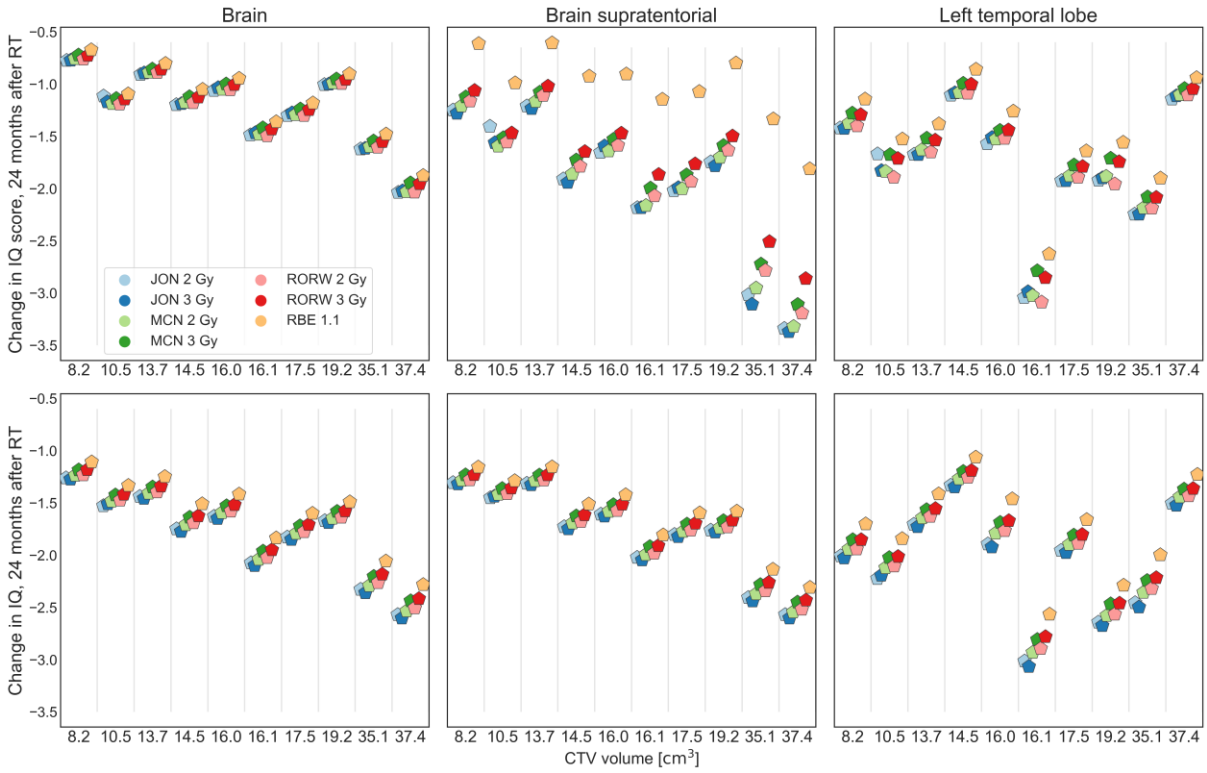

Figure 7.16: Estimated change in IQ scores 24 months after radiation therapy (RT) treatment calculated from equation (6.4 – 6.9). The upper row shows calculation from dose/volume models, whereas the lower row represents models based on mean dose. The patients are sorted in ascending order by CTV.

The craniopharyngioma models (Eq. 6.2 – 6.4) resulted in the highest IQ score change of all IQ models with a median value of -8.9 [-10.0, -7.0] (Fig. 7.17). The trend with lower IQ score decline with RBE 1.1 compared to the variable RBE models seen be the CNS models were not seen for the craniopharyngioma models. Across all craniopharyngioma models, the median value was -8.1 [-9.3, -7.0] for JON, -9 [-9.9, -7.6] for RORW and -8.9 [-10, -7.2] for MCN. For RBE 1.1, the median was -8.9 [-9.5, -8.1]. RORW with an $(\alpha/\beta)_x$ of 2 Gy as input parameter did not result in a statistically significant difference compared with RBE 1.1 for any of the craniopharyngioma models. Variations were seen across the three different craniopharyngioma models, and the supratentorial brain model differed significantly from both the other models. The model based on the brain dose/volume intervals estimated the largest change with a median value of -9.1 [-10, -7.0]. The left temporal lobe and supratentorial brain models resulted in a median value of -9.0 [-9.6, -8.1] and -8.7 [-9.8, -7.3], respectively.

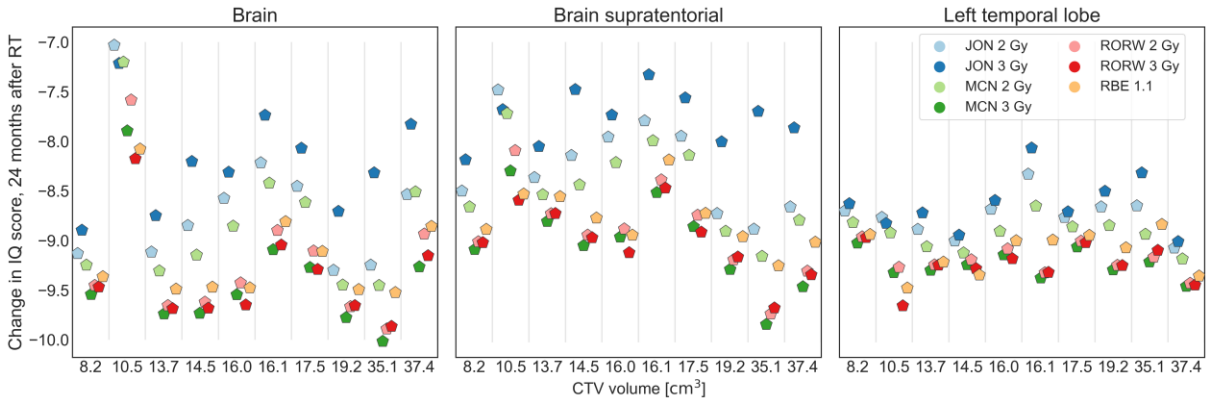

Figure 7.17: Estimated change in IQ scores 24 months after radiation therapy (RT) treatment calculated from equation (6.1 – 6.3). The patients are sorted in ascending order by CTV.

In terms of the investigated 13 % threshold for the left temporal lobes 43.2 Gy, no values above 13 % were found for any of the patients, as shown in Figure 7.18. However, some of the temporal lobe substructures, e. g. amygdala and entorhinal cortex showed values above the threshold across all models and patients.

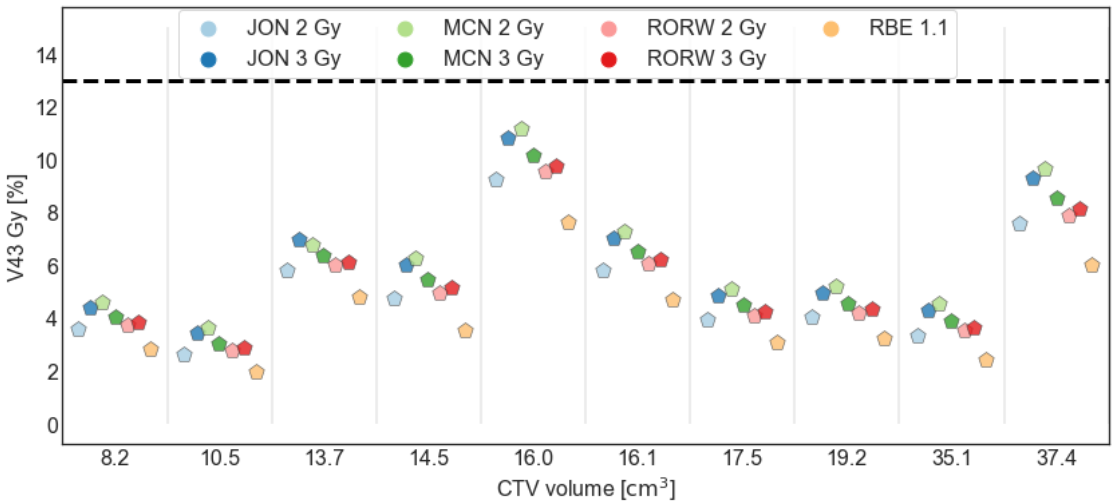

Figure 7.18: Volume of the left temporal lobe receiving 43.2 Gy(RBE). The patients are sorted in ascending order by CTV.

Overall, elevated RBE led to a higher risk of memory impairment, as shown in Figure 7.19. At 24 months after radiation therapy treatment, the median risk of memory impairment across the selected models was 40 % [34 % - 49 %], slightly higher than RBE 1.1, which resulted in the median value of 38 % [33 % - 45 %]. The difference in the estimated risk of memory impairment between the three selected models was not significant. Across all patients, the median and range in impairment risk were 40% [35%, 49%] for JON, and 39% [34%, 48%] for both RORW and MCN.

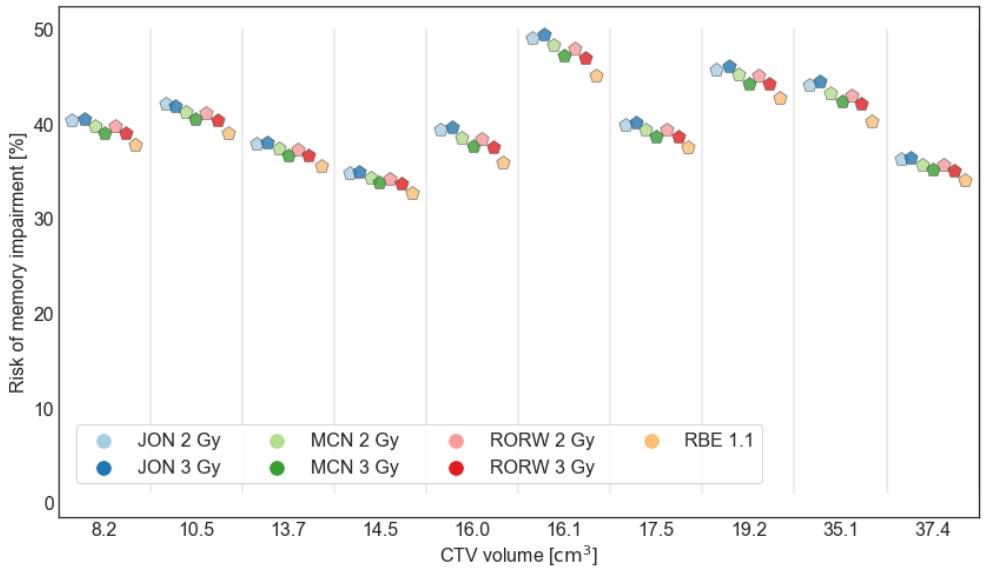

Figure 7.19: Estimated risk of memory impairment 24 months after radiation therapy (RT) treatment calculated from equation (6.13). The patients are sorted in ascending order by CTV.

Compared to the variable RBE models, changes in DVeM scaled score was consistently lower for RBE 1.1, as seen in Figure 7.20. The model by JON systematically resulted in the highest change of the selected set of models, whereas the model by RORW and MCN resulted in the same median value and range. Across all patients, the median changes in DVeM scaled score were –0.77 [-0.97, -0.58] for RBE 1.1, -0.85 [-1.02, -0.63] for JON, and -0.83 [-1.01, -0.60] for both RORW and MCN.

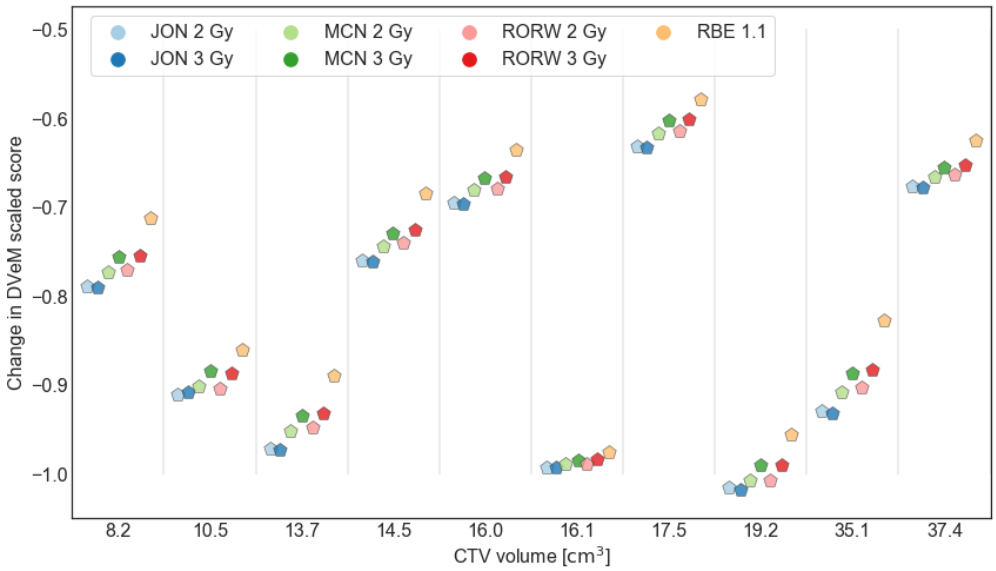

Figure 7.20: Changes in delayed verbal memory scores 24 months after radiation therapy (RT) treatment calculated from equation (6.14). The patients are sorted by ascending order by CTV.

Table 7.3: This table presents the median value and corresponding range calculated from equations 6.2 – 6.14 across all patients. Column to the far left shows the number of the equation used. The numbers in the cells below each variable RBE model represents the input parameter of $(\alpha/\beta)_x$. Cells colored grey indicate statistically significant ($p < 0.05$) compared to RBE 1.1 all patients considered by the Wilcoxon Signed-Rank Test, whereas cells colored pink indicate a trend to significance ($0.05 < p < 0.1$).

#	Median [range]						
	RBE 1.1	**JON**		**MCN**		**RORW**	
		Input parameter of $(\alpha/\beta)_x$					
		2	3	2	3	2	3
Merchant et al. (2006a): Estimated change in IQ scores							
(6.2)	-9.4 [-9.5, -8.1]	-8.7 [-9.3, -7.0]	-8.3 [-8.9, -7.2]	-9.0 [-9.5, -7.2]	-9.5 [-10.0, -7.9]	-9.4 [-9.9, -7.6]	-9.6 [-9.9, -8.2]
(6.3)	-8.8 [-9.2, -8.2]	-8.2 [-8.9, -7.5]	-7.7 [-8.2, -7.3]	-8.5 [-9.1, -7.7]	-9.0 [-9.8, -8.3]	-8.9 [-9.7, -8.1]	-9.0 [-9.7, -8.5]
(6.4)	-9.0 [-9.5, -8.8]	-8.7 [-9.1, -8.3]	-8.7 [-9.0, -8.1]	-8.9 [-9.2, -8.6]	-9.2 [-9.4, -9.0]	-9.2 [-9.4, -8.9]	-9.2 [-9.6, -9.0]
Merchant et al. (2006b): Estimated change in IQ scores							
(6.5)	-1.1 [-1.9, -0.7]	-1.2 [-2.0, -0.8]	-1.2 [-2.0, -0.8]	-1.2 [-2.0, -0.8]	-1.1 [-1.9, -0.7]	-1.2 [-2.0, -0.8]	-1.1 [-2.0, -0.7]
(6.6)	-0.9 [-3.3, -0.6]	-1.8 [-3.4, -1.2]	-1.8 [-3.3, -1.2]	-1.8 [-3.1, -1.1]	-1.6 [-3.2, -1.0]	-1.7 [-2.9, -1.1]	-1.5 [-2.9, -1.0]
(6.7)	-1.5 [-2.6, -0.9]	-1.7 [-3.0, -1.1]	-1.8 [-3.0, -1.1]	-1.7 [-3.0, -1.1]	-1.6 [-2.8, -1.0]	-1.8 [-3.1, -1.1]	-1.6 [-2.9, -1.0]
(6.8)	-1.5 [-2.3, -1.1]	-1.7 [-2.6, -1.3]	-1.7 [-2.6, -1.3]	-1.7 [-2.5, -1.2]	-1.6 [-2.4, -1.2]	-1.7 [-2.5, -1.2]	-1.6 [-2.4, -1.2]
(6.9)	-1.5 [-2.3, -1.2]	-1.7 [-2.6, -1.3]	-1.8 [-2.6, -1.3]	-1.7 [-2.5, -1.3]	-1.6 [-2.4, -1.2]	-1.7 [-2.5, -1.3]	-1.6 [-2.4, -1.2]
(6.10)	-1.7 [-2.6, -1.1]	-2.0 [-3.0, -1.3]	-2.0 [-3.1, -1.3]	-1.9 [-2.9, -1.3]	-1.8 [-2.8, -1.2]	-1.9 [-2.9, -1.3]	-1.8 [-2.8, -1.2]
Merchant et al. (2008): Estimated change in IQ scores							
(6.11)	0.0 [0.0, 0.0]	0.0 [0.0, 0.0]	0.0 [0.0, 0.0]	0.0 [0.0, 0.0]	0.0 [0.0, 0.0]	0.0 [0.0, 0.0]	0.0 [0.0, 0.0]
Jalali et al. (2010): Risk of FSIQ score decline							
(6.12)	< 13 %	< 13 %	< 13 %	< 13 %	< 13 %	< 13 %	< 13 %
Armstrong et al. (2010): Risk of memory impairment [%]							
(6.13)	38 [33, 45]	40 [35 , 49]	40 [35 , 49]	40 [34, 48]	39 [34, 47]	40 [34 , 48]	39 [34, 47]
Zureick et al. (2018): Delayed verbal memory score							
(6.14)	-0.77 [-0.97, -0.58]	-0.85 [-1.02, -0.63]	-0.85 [-1.02, -0.63]	-0.84 [-1.01, -0.62]	-0.82 [-0.99, -0.60]	-0.84 [-1.01, -0.61]	-0.82 [-0.99, -0.60]

8 Discussion

In this thesis, a large number of BSCs were investigated in terms of cognitive impairment and RBE related to proton therapy of pediatric brain tumors. The results of this project illustrated that estimated proton RBE values to BSCs differ considerably when a large number of variable RBE models are utilized. By the inclusion of several variable RBE models, some of the uncertainties regarding the biological effectiveness of protons can be integrated into cognitive decline estimates. As the concept of variable RBE is known, a range of values might better reflect cognitive decline estimates in proton therapy than using the universal constant of 1.1.

The results of the RBE_d, when applying all models, showed more variations as compared to using the selected models only. The criteria for further model selectivity accounted for both physical and biological factors by including $(\alpha/\beta)_x$ and LET as selection criterion; however, the criteria-based method with the same cut-off values is limited to similar patient groups. In the case of other endpoints, e.g. tumor control, the $(\alpha/\beta)_x$ cut-off values should be adjusted accordingly, and preferably also include $(\alpha/\beta)_x$ intervals to account for the uncertainties in this factor which alone represents complex biological factors. Compared to the phenomenological models, the plan-based model by Unkelbach et al. presented lower scores for RBE_d across all structures than the associated median RBE_d values, which demonstrates the extension of tissue dependence, and the potential for underestimating biological effects when omitting tissue dependence.

The cut-off value for the total number of data points was based on the assumption that models based on a limited set of data may be more susceptible to uncertainties. Of the excluded models, the CHD model was the only model that would be included in the selected set if the data point criterion was neglected. In addition, the relative frequency of data point values is not accounted for through the criteria that were set. For instance, the WIL and CAR models came short in terms of the cut-off value of $(\alpha/\beta)_x$; however, the models have a high frequency of data point values of LET_d within the clinical region [73, 74, 76]. These models provided values relatively close to the median value for most structures across all models, and therefore including these would have made modest differences to the estimated biological dose and RBE_d range resulting from the selected set of models. As most clinical LET_d values are within the range of 2 – 5 keV μm^{-1} [59], the LET-range could have been set narrower. However, the outcome of the LET

selection criteria would not have been affected by narrowing this span of values, as most of the models not fulfilling the LET criterion lacked data point values in the lower region. The lack of datapoint values in the lower region for the CHE, TIL and WED models are accounted for by extrapolation from high LET_d data; although, this may not be a sufficient assumption if regions with low LET_d should be non-linear [76, 100].

The increasing RBE with decreasing $(\alpha/\beta)_x$ shown in the work of Paganetti et al. [59] was prominent for the RORW and MCN model, as excepted [66, 71, 76]. This tendency is most prominent for low $(\alpha/\beta)_x$ values, e.g. those utilized in this study, especially for large LET_d values [76]. An increase of RBE with increasing $(\alpha/\beta)_x$ generally appeared for the JON model. This is in agreement with results from Rørvik et al. [76]. Furthermore, the JON model resulted in the highest RBE_d combined with the lowest difference between input parameters ($(\alpha/\beta)_x$ of 2 and 3 Gy). As mentioned by Rørvik et al., the model which resulted in the highest RBE_d values in this project of the selected set, the JON model, is derived from experimental data based on heavier particles (e.g., helium and carbon) as well as protons. These heavier ions have, in general, higher RBE than protons for the same LET values [67, 76]. The presence of data from heavier particles in model estimation may lead to an overestimate of proton RBE. As the RBE increases with decreasing $(\alpha/\beta)_x$ for RORW and MCN contrary to JON, the span of estimated RBE values would increase if a higher $(\alpha/\beta)_x$ values were applied for the set of models.

BSCs exposed to high doses and elevated RBE_d are more vulnerable to toxicity. Compared to the whole temporal lobes, high mean doses and elevated RBE_d was predicted in some of the temporal lobe substructures. This highlights the significance of variable RBE to smaller substructures. The amygdala and entorhinal cortex, both among the temporal lobe substructures, were in general exposed to high doses and predicted high RBE_d values.

The cerebellum has recently been suggested as a structure related to cognition [101], and both its posterior and anterior parts are correlated to IQ decline [20]. Even though BSCs exposed to high biological doses were of particular interest, low doses to the brain in pediatric patients has also been reported to affect intellectual development [102]. All of the cerebellum substructures resulted in high RBE_d for all patients across all variable RBE models, combined with low physical doses. The cerebellum is located beneath the cerebral hemisphere and near the target volume. Similar to previous studies, our results support the elevated RBE in high LET-regions

[59], bearing in mind that both the dose- and LET dependency are likely to explain the high RBE values found.

The supratentorial region is one of the suggested larger volumes of the brain connected to cognitive impairment [19]. Among the supratentorial structures, estimates of the RBE_d values for the left and right thalamus predicted high values and were exposed to high doses. The parietal and frontal lobes, also among the supratentorial structures, were spared of high RBE_d compared to other structures. These structures are located in the entrance region of the beams. A closer agreement across the set of models was generally seen for BSCs located in low LET_d regions. The entrance region is generally exposed to lower LET values [59], which might explain the relatively low RBE_d values found in the parietal and frontal lobes compared to other studied BSCs.

In the matter of the dose/volume parameters analyzed, the most considerable difference to the biological dose with RBE of 1.1 was seen for the %V40Gy parameter. As no values across the selected set of models resulted in values below the biological dose with RBE of 1.1 for either %V10Gy or %V40Gy, white matter damage and higher reduction of neural stem cell numbers are expected to occur considering the selected variable RBE models.

Significant discrepancies were seen in IQ estimates, both across IQ score models and variable proton RBE models. The somewhat inconsistent results of IQ decline across the utilized models could be explained by several reasons. Firstly, two of the publications developed models from 3D conformal radiation therapy (photon), where the dose patterns differ considerably from proton treatments. The transferability of these models to proton therapy treatment, therefore, needs to be questioned. Due to the potential inadequacy of photon technique models in determining potential cognitive impairment, the results need to be interpreted with caution. In general, some of the volumes of brain tissue are likely to receive a smaller amount of low to intermediate doses, due to the higher conformity achieved by proton therapy.

Secondly, the patient groups used in model fitting also varied between the publications. The number of patients used to develop the models were 10 for the craniopharyngioma proton model, 28 for the craniopharyngioma models, and 39 for the CNS models, which overall is a small number of patients in model fitting.

In general, both increased volume fraction and radiation dose will result in lower IQ scores [103]. Considering the IQ models, both low and high doses contribute to a decline in IQ scores. Common for most equations is that the volume which receives the highest dose has a superior impact on the IQ decline [97].

In terms of the craniopharyngioma proton model, Merchant et al. demonstrated a smaller decline in IQ scores 24 months after radiation therapy treatment with protons compared to photons. However, the results for the craniopharyngioma model in this thesis indicated a noticeably small decline in IQ score, also when compared to results from Merchant et al. [10]. One significant drawback of this model is that there is no clear explanation of how the model was fitted.

Of the CNS models, the supratentorial brain model was considered as the best by the authors, due to the level of significance of each dose/volume term in addition to the difference in comparative dose-effect [98]. In whole-brain irradiation cases, all of the structures are expected to receive more significant fractions of low to intermediate doses. Of the cohort of 39 patients, 14 patients received whole-brain irradiation with posterior fossa boost. The temporal lobes might have received parts of this boost, as seen from Figure 1 in Merchant et al. [98]. Craniopharyngioma patients are usually treated with focal irradiation, and the temporal lobes are in close vicinity to the target volume. The dose distribution to the temporal lobes were reasonably comparable to the patients used in developing the model, whereas the dose distribution to the brain and supratentorial brain differed.

The CNS models systematically resulted in higher estimates of IQ decline for the proton RBE models compared to RBE 1.1. This was not the case for the craniopharyngioma model, where RBE 1.1 estimated IQ decline above the median value for all patients. One noticeable difference between the CNS dose/volume models and the craniopharyngioma dose/volume models is the intermediate term, which has opposite signs [88, 98]. For the CNS models, all dose/volume interval terms are expected to have a negative impact on the IQ decline, whereas the intermediate-term is expected to have a positive impact on the craniopharyngioma models. This might be a possible explanation for the contradictory results when comparing the IQ score decline for the RBE 1.1 and the variable RBE models.

The results found for the craniopharyngioma models in this thesis were comparable to those of Toussaint et al., who also found high values of IQ decline scores using the same models for the

same patient group [13]. It is unsurprising to find that there is a considerable variation between the IQ score models due to the dissimilarities in the patient group, treatment method, and fitting of the model. Considering the set of IQ-models chosen for this thesis, elevated RBE is not necessarily associated with a higher decline in IQ score. Obviously, linear models based on the mean dose will result in higher IQ decline with elevated RBE. However, the craniopharyngioma dose/volume models did not show a clear correlation between elevated RBE and higher decline in IQ score. Due to the differences in dose distribution between photons and protons, one might argue that the D_{mean} are more transferable to proton dose distributions than the dose/volume intervals.

As seen from the results in section 7.3, estimates of the hippocampus resulted in elevated RBE for all patients. The hippocampus is located in close vicinity to the target, and the differences of RBE-weighted dose of 1.1 and the variable proton RBE models were expected to result in large variations in delayed verbal memory scores. It can be seen from the equation that the dose/volume term has a reasonably low impact on the overall change in delayed verbal memory score compared to other covariates. This might explain the small differences between the proton RBE models.

The publications by Merchant et al. were based on estimated the IQ score, which, as aforementioned, does not include the processing of speed. Even though the volumes of the temporal lobe receiving 43.2 Gy were below the threshold of 13% across all variable RBE models for all patients, the elevated doses to the left temporal lobe according to the models still might lead to a higher likelihood of cognitive impairment.

9 Conclusion

This study showed that there was a large and systematic model-dependent variation in RBE across the cognitive structures. The broad span of values of resulting RBE and dose/volume parameter values, especially seen by the use of all models mirrors the uncertainty associated with the biological effects of protons. Through a criteria-based approach, it was possible to select a set of models that may provide a more accurate estimate of RBE-weighted dose ranges to BSCs. The three selected models systematically predicted RBE and dose/volume parameter values above the generic RBE constant of 1.1 for all BSCs investigated. These results suggest that the biological dose is underestimated in the BSCs for this patient group when using the clinically applied RBE of 1.1. As a result of the underestimated dose, the potential cognitive impairment might also be underestimated. As seen in this study, the smaller cognitive substructures may be susceptible to elevated RBE and biological dose. It could therefore be beneficial to assess smaller substructures when interpreting cognitive impairment after proton therapy as these may provide more detailed information compared to analysis of exclusively larger brain structures or regions.

10 Bibliography

1. Kreftregisteret.no, *Kreftstatistikk.* 2018.
2. Ward, E., et al., *Childhood and adolescent cancer statistics, 2014.* CA Cancer J Clin, 2014. **64**(2): p. 83-103.
3. Drapeau, A., et al., *Pediatric craniopharyngioma.* 2019.
4. Stripp, D.C., et al., *Surgery with or without radiation therapy in the management of craniopharyngiomas in children and young adults.* Int J Radiat Oncol Biol Phys, 2004. **58**(3): p. 714-20.
5. Habrand, J.L., et al., *The role of radiation therapy in the management of craniopharyngioma: a 25-year experience and review of the literature.* Int J Radiat Oncol Biol Phys, 1999. **44**(2): p. 255-63.
6. Reimers, T.S., et al., *Cognitive deficits in long-term survivors of childhood brain tumors: Identification of predictive factors.* Med Pediatr Oncol, 2003. **40**(1): p. 26-34.
7. Wilson, R.R., *Radiological use of fast protons.* Radiology, 1946. **47**(5): p. 487-91.
8. Baumert BG, N.I., Lomax AJ et al (2004) *Dose conformation of intensity-modulated stereotactic photon beams, proton beams and intensity modulated proton beams for intracranial lesions.* 2004. **60**(4): p. 10.
9. Durante, M. and H. Paganetti, *Nuclear physics in particle therapy: a review.* Rep Prog Phys, 2016. **79**(9): p. 096702.
10. Merchant, T.E., et al., *Proton versus photon radiotherapy for common pediatric brain tumors: comparison of models of dose characteristics and their relationship to cognitive function.* Pediatr Blood Cancer, 2008. **51**(1): p. 110-7.
11. Pulsifer, M.B., et al., *Early Cognitive Outcomes Following Proton Radiation in Pediatric Patients With Brain and Central Nervous System Tumors.* Int J Radiat Oncol Biol Phys, 2015. **93**(2): p. 400-7.
12. Kahalley, L.S., et al., *Comparing Intelligence Quotient Change After Treatment With Proton Versus Photon Radiation Therapy for Pediatric Brain Tumors.* J Clin Oncol, 2016. **34**(10): p. 1043-9.
13. Toussaint, L., et al., *Temporal lobe sparing radiotherapy with photons or protons for cognitive function preservation in paediatric craniopharyngioma.* Radiotherapy and Oncology, 2019.
14. Ajithkumar, T., et al., *Proton Therapy for Craniopharyngioma - An Early Report from a Single European Centre.* Clin Oncol (R Coll Radiol), 2018. **30**(5): p. 307-316.
15. Mohan, R., et al., *Radiobiological issues in proton therapy.* Acta Oncol, 2017. **56**(11): p. 1367-1373.
16. Haas-Kogan, D., et al., *National Cancer Institute Workshop on Proton Therapy for Children: Considerations Regarding Brainstem Injury.* Int J Radiat Oncol Biol Phys, 2018. **101**(1): p. 152-168.
17. Paganetti, H., *Relating proton treatments to photon treatments via the relative biological effectiveness-should we revise current clinical practice?* Int J Radiat Oncol Biol Phys, 2015. **91**(5): p. 892-4.
18. Carabe, A., et al., *Clinical consequences of relative biological effectiveness variations in proton radiotherapy of the prostate, brain and liver.* Phys Med Biol, 2013. **58**(7): p. 2103-17.
19. Merchant, T.E.e.a., *Modeling radiation dosimetry to predict cognitive outcomes in paediatric patients with CNS embryonal tumours including medulloblastoma.* Int J Radiat Oncol, 2006. **65**: p. 210-221.

20. Merchant, T.E., et al., *Effect of cerebellum radiation dosimetry on cognitive outcomes in children with infratentorial ependymoma.* Int J Radiat Oncol Biol Phys, 2014. **90**(3): p. 547-53.
21. Jalali, R., et al., *Factors influencing neurocognitive outcomes in young patients with benign and low-grade brain tumors treated with stereotactic conformal radiotherapy.* Int J Radiat Oncol Biol Phys, 2010. **77**(4): p. 974-9.
22. Armstrong, G.T., et al., *Region-specific radiotherapy and neuropsychological outcomes in adult survivors of childhood CNS malignancies.* Neuro Oncol, 2010. **12**(11): p. 1173-86.
23. Zureick, A.H., et al., *Left hippocampal dosimetry correlates with visual and verbal memory outcomes in survivors of pediatric brain tumors.* Cancer, 2018. **124**(10): p. 2238-2245.
24. Doger de Speville, E., et al., *Relationships between Regional Radiation Doses and Cognitive Decline in Children Treated with Cranio-Spinal Irradiation for Posterior Fossa Tumors.* Front Oncol, 2017. **7**: p. 166.
25. Redmond, K.J., et al., *Association of Neuronal Injury in the Genu and Body of Corpus Callosum After Cranial Irradiation in Children With Impaired Cognitive Control: A Prospective Study.* Int J Radiat Oncol Biol Phys, 2018. **101**(5): p. 1234-1242.
26. Mohan, R. and D. Grosshans, *Proton therapy - Present and future.* Adv Drug Deliv Rev, 2017. **109**: p. 26-44.
27. Paganetti, H. and P. van Luijk, *Biological considerations when comparing proton therapy with photon therapy.* Semin Radiat Oncol, 2013. **23**(2): p. 77-87.
28. Jermann, M., *PTCOG - Patient Statistics.* https://ptcog.ch/index.php/patient-statistics, 2018.
29. Khan, F.M. and J.P. Gibbons, *Khan's the physics of radiation therapy*. 2014.
30. Stokkevåg, C.H., *Model-based predictions of secondary cancer and late effect risks following particle therapy.* Ph.D thesis. University of Bergen, 2016.
31. Olive, K.A., *Review of Particle Physics.* Chinese Physics C, 2014. **38**(9): p. 090001.
32. Lomax, A.J., *Charged particle therapy: the physics of interaction.* Cancer J, 2009. **15**(4): p. 285-91.
33. Bragg, W.H. and R. Kleeman, *LXXIV. On the ionization curves of radium.* The London, Edinburgh, and Dublin Philosophical Magazine and Journal of Science, 1904. **8**(48): p. 726-738.
34. Newhauser, W.D. and R. Zhang, *The physics of proton therapy.* Phys Med Biol, 2015. **60**(8): p. R155-209.
35. Leeman, J.E., et al., *Proton therapy for head and neck cancer: expanding the therapeutic window.* Lancet Oncol, 2017. **18**(5): p. e254-e265.
36. Eric J. Hall, A.J.G., *Radiobiology for the radiologist.* 2006. 6th edition.
37. Paganetti, H., *Proton Therapy Physics.* CRC Press, 2011.
38. International Commission on Radiation, U. and Measurements, *Prescribing, recording, and reporting photon beam therapy (supplement to ICRU report 50)*. 1999, Bethesda, Md.: International Commission on Radiation Units and Measurements.
39. Jones, D., *ICRU Report 50—Prescribing, Recording and Reporting Photon Beam Therapy.* 1994. **21**(6): p. 833-834.
40. Deluca, P., A. Wambersie, and G. Whitmore, *Prescribing, recording, and reporting proton-beam therapy.* Journal of the ICRU, 2007. **7**: p. 1-210.
41. Joiner, M. and A.v.d. Kogel, *Basic clinical radiobiology*. 2009, London: Hodder Arnold.
42. Brizel, D.M., *Pharmacologic approaches to radiation protection.* J Clin Oncol, 2007. **25**(26): p. 4084-9.

43. Schwarz, M., *Treatment planning in proton therapy.* The European Physical Journal Plus, 2011. **126**: p. 1-10.
44. Ma, C.M., et al., *Monte Carlo verification of IMRT dose distributions from a commercial treatment planning optimization system.* Physics in Medicine and Biology, 2000. **45**(9): p. 2483-2495.
45. Bauer, J., et al., *Integration and evaluation of automated Monte Carlo simulations in the clinical practice of scanned proton and carbon ion beam therapy.* Phys Med Biol, 2014. **59**(16): p. 4635-59.
46. Paganetti, H., et al., *Clinical implementation of full Monte Carlo dose calculation in proton beam therapy.* Phys Med Biol, 2008. **53**(17): p. 4825-53.
47. Paganetti, H., *Proton Beam Therapy*. 2017, IOP Publishing.
48. Girdhani, S., R. Sachs, and L. Hlatky, *Biological effects of proton radiation: what we know and don't know.* Radiat Res, 2013. **179**(3): p. 257-72.
49. Hall, E.J. and A.J. Giaccia, *Radiobiology for the radiologist*. 2012, Philadelphia: Wolters Kluwer Health/Lippincott Williams & Wilkins.
50. Jones, B., *Why RBE must be a variable and not a constant in proton therapy.* Br J Radiol, 2016. **89**(1063): p. 20160116.
51. Zirkle, R.E., D.F. Marchbank, and K.D. Kuck, *Exponential and sigmoid survival curves resulting from alpha and x irradiation of Aspergillus spores.* J Cell Physiol Suppl, 1952. **39**(Suppl. 1): p. 78-85.
52. *Report 85: Fundamental quantities and units for ionizing radiation.* J icru, 2011.
53. Romano, F., et al., *A Monte Carlo study for the calculation of the average linear energy transfer (LET) distributions for a clinical proton beam line and a radiobiological carbon ion beam line.* Phys Med Biol, 2014. **59**(12): p. 2863-82.
54. Guan, F., et al., *Analysis of the track- and dose-averaged LET and LET spectra in proton therapy using the geant4 Monte Carlo code.* Med Phys, 2015. **42**(11): p. 6234-47.
55. Jones, B., et al., *The Role of Biologically Effective Dose (BED) in Clinical Oncology.* Clinical Oncology, 2001. **13**(2): p. 71-81.
56. Jones, B., S.J. McMahon, and K.M. Prise, *The Radiobiology of Proton Therapy: Challenges and Opportunities Around Relative Biological Effectiveness.* Clin Oncol (R Coll Radiol), 2018. **30**(5): p. 285-292.
57. International Commission on Radiation, U. and Measurements, *The 2007 Recommendations of the International Commission on Radiological Protection. ICRP publication 103.* Ann ICRP, 2007. **37**(2-4): p. 1-332.
58. Paganetti, H., et al., *Relative biological effectiveness (RBE) values for proton beam therapy.* Int J Radiat Oncol Biol Phys, 2002. **53**(2): p. 407-21.
59. Paganetti, H., *Relative biological effectiveness (RBE) values for proton beam therapy. Variations as a function of biological endpoint, dose, and linear energy transfer.* Phys Med Biol, 2014. **59**(22): p. R419-72.
60. Paganetti, H., *Significance and implementation of RBE variations in proton beam therapy.* Technol Cancer Res Treat, 2003. **2**(5): p. 413-26.
61. Barendsen, G.W., *Responses of cultured cells, tumours, and normal tissues to radiations of different linear energy transfer*. 1968: p. Medium: X.
62. Paganetti, H. and D. Giantsoudi, *Relative Biological Effectiveness Uncertainties and Implications for Beam Arrangements and Dose Constraints in Proton Therapy.* Semin Radiat Oncol, 2018. **28**(3): p. 256-263.
63. Unkelbach, J., et al., *Reoptimization of Intensity Modulated Proton Therapy Plans Based on Linear Energy Transfer.* Int J Radiat Oncol Biol Phys, 2016. **96**(5): p. 1097-1106.

64. Chaudhary, P., et al., *Relative Biological Effectiveness Variation Along Monoenergetic and Modulated Bragg Peaks of a 62-MeV Therapeutic Proton Beam: A Preclinical Assessment.* International Journal of Radiation Oncology*Biology*Physics, 2014. **90**(1): p. 27-35.
65. Chen, Y. and S. Ahmad, *Empirical model estimation of relative biological effectiveness for proton beam therapy.* Radiat Prot Dosimetry, 2012. **149**(2): p. 116-23.
66. Rorvik, E., et al., *A phenomenological biological dose model for proton therapy based on linear energy transfer spectra.* Med Phys, 2017. **44**(6): p. 2586-2594.
67. Jones, B., *Towards Achieving the Full Clinical Potential of Proton Therapy by Inclusion of LET and RBE Models.* Cancers (Basel), 2015. **7**(1): p. 460-80.
68. Peeler, C.R., et al., *Clinical evidence of variable proton biological effectiveness in pediatric patients treated for ependymoma.* Radiother Oncol, 2016. **121**(3): p. 395-401.
69. Tilly, N., et al., *The influence of RBE variations in a clinical proton treatment plan for a hypopharynx cancer.* Phys Med Biol, 2005. **50**(12): p. 2765-77.
70. Wedenberg, M., B.K. Lind, and B. Hardemark, *A model for the relative biological effectiveness of protons: the tissue specific parameter alpha/beta of photons is a predictor for the sensitivity to LET changes.* Acta Oncol, 2013. **52**(3): p. 580-8.
71. McNamara, A.L., J. Schuemann, and H. Paganetti, *A phenomenological relative biological effectiveness (RBE) model for proton therapy based on all published in vitro cell survival data.* Phys Med Biol, 2015. **60**(21): p. 8399-416.
72. Frese, M.C., et al., *Application of constant vs. variable relative biological effectiveness in treatment planning of intensity-modulated proton therapy.* Int J Radiat Oncol Biol Phys, 2011. **79**(1): p. 80-8.
73. Wilkens, J.J. and U. Oelfke, *A phenomenological model for the relative biological effectiveness in therapeutic proton beams.* Phys Med Biol, 2004. **49**(13): p. 2811-25.
74. Carabe, A., et al., *Range uncertainty in proton therapy due to variable biological effectiveness.* Phys Med Biol, 2012. **57**(5): p. 1159-72.
75. Mairani, A., et al., *A phenomenological relative biological effectiveness approach for proton therapy based on an improved description of the mixed radiation field.* Phys Med Biol, 2017. **62**(4): p. 1378-1395.
76. Rorvik, E., et al., *Exploration and application of phenomenological RBE models for proton therapy.* Phys Med Biol, 2018. **63**(18): p. 185013.
77. Carabe-Fernandez, A., R.G. Dale, and B. Jones, *The incorporation of the concept of minimum RBE (RbEmin) into the linear-quadratic model and the potential for improved radiobiological analysis of high-LET treatments.* Int J Radiat Biol, 2007. **83**(1): p. 27-39.
78. Dale, R.G. and B. Jones, *The assessment of RBE effects using the concept of biologically effective dose.* Int J Radiat Oncol Biol Phys, 1999. **43**(3): p. 639-45.
79. Belli, M., A. Campa, and I. Ermolli, *A semi-empirical approach to the evaluation of the relative biological effectiveness of therapeutic proton beams: the methodological framework.* Radiat Res, 1997. **148**(6): p. 592-8.
80. Frost, M.H. and J.A. Sloan, *Quality of life measurements: a soft outcome--or is it?* Am J Manag Care, 2002. **8**(18 Suppl): p. S574-9.
81. Toussaint, L., et al., *Radiation doses to brain substructures associated with cognition in radiotherapy of pediatric brain tumors.* Acta Oncol, 2019: p. 1-6.
82. Grill, J., et al., *Long-term intellectual outcome in children with posterior fossa tumors according to radiation doses and volumes.* Int J Radiat Oncol Biol Phys, 1999. **45**(1): p. 137-45.
83. Lawrence, Y.R., et al., *Radiation dose-volume effects in the brain.* Int J Radiat Oncol Biol Phys, 2010. **76**(3 Suppl): p. S20-7.

84. Ailion, A.S., K. Hortman, and T.Z.J.N.R. King, *Childhood Brain Tumors: a Systematic Review of the Structural Neuroimaging Literature.* 2017. **27**(3): p. 220-244.
85. Makale, M.T., et al., *Mechanisms of radiotherapy-associated cognitive disability in patients with brain tumours.* Nat Rev Neurol, 2017. **13**(1): p. 52-64.
86. Peiffer, A.M., et al., *Neuroanatomical target theory as a predictive model for radiation-induced cognitive decline.* Neurology, 2013. **80**(8): p. 747-53.
87. Burgess, L., et al., *Estimated IQ Systematically Underestimates Neurocognitive Sequelae in Irradiated Pediatric Brain Tumor Survivors.* Int J Radiat Oncol Biol Phys, 2018. **101**(3): p. 541-549.
88. Merchant, T.E., et al., *Phase II trial of conformal radiation therapy for pediatric patients with craniopharyngioma and correlation of surgical factors and radiation dosimetry with change in cognitive function.* J Neurosurg, 2006. **104**(2 Suppl): p. 94-102.
89. Pulsifer, M.B., et al., *Cognitive and Adaptive Outcomes After Proton Radiation for Pediatric Patients With Brain Tumors.* Int J Radiat Oncol Biol Phys, 2018. **102**(2): p. 391-398.
90. Redmond, K.J., et al., *Association between radiation dose to neuronal progenitor cell niches and temporal lobes and performance on neuropsychological testing in children: a prospective study.* Neuro Oncol, 2013. **15**(3): p. 360-9.
91. Gondi, V., et al., *Hippocampal dosimetry predicts neurocognitive function impairment after fractionated stereotactic radiotherapy for benign or low-grade adult brain tumors.* Int J Radiat Oncol Biol Phys, 2013. **85**(2): p. 348-54.
92. Gondi, V., et al., *Preservation of memory with conformal avoidance of the hippocampal neural stem-cell compartment during whole-brain radiotherapy for brain metastases (RTOG 0933): a phase II multi-institutional trial.* J Clin Oncol, 2014. **32**(34): p. 3810-
93. Ferrari, A., et al., *FLUKA: a multi-particle transport code.* CERN Yellow report, 2005. **2005-10**.
94. Böhlen, T.T., et al., *The FLUKA Code: Developments and Challenges for High Energy and Medical Applications.* Nuclear Data Sheets, 2014. **120**: p. 211-214.
95. Fjæra, L.F., *Development of a Monte Carlo Based Treatment Planning Verification Tool for Particle Therapy.* Master thesis, 2016. UiB.
96. Tilly, N., et al., *Comparison of cell survival models for mixed LET radiation.* Int J Radiat Biol, 1999. **75**(2): p. 233-43.
97. Blomstrand, M., et al., *Estimated clinical benefit of protecting neurogenesis in the developing brain during radiation therapy for pediatric medulloblastoma.* Neuro-Oncology, 2012. **14**(7): p. 882-889.
98. Merchant, T.E., et al., *Modeling radiation dosimetry to predict cognitive outcomes in pediatric patients with CNS embryonal tumors including medulloblastoma.* Int J Radiat Oncol Biol Phys, 2006. **65**(1): p. 210-21.
99. Rey, D. and M. Neuhäuser, *Wilcoxon-Signed-Rank Test*, in *International Encyclopedia of Statistical Science*, M. Lovric, Editor. 2011, Springer Berlin Heidelberg: Berlin, Heidelberg. p. 1658-1659.
100. Paganetti, H., et al., *Report of the AAPM TG-256 on the relative biological effectiveness of proton beams in radiation therapy.* 2019. **46**(3): p. e53-e78.
101. Eekers, D.B.P., et al., *The posterior cerebellum, a new organ at risk?* Clin Transl Radiat Oncol, 2018. **8**: p. 22-26.
102. Hall, P., et al., *Effect of low doses of ionising radiation in infancy on cognitive function in adulthood: Swedish population based cohort study.* Bmj, 2004. **328**(7430): p. 19.
103. Padovani, L., et al., *Neurocognitive function after radiotherapy for paediatric brain tumours.* Nature Reviews Neurology, 2012. **8**(10): p. 578-588.

Appendix A

This chapter presents the mathematical formulation of the variable RBE models used in this thesis. All models with the exception of CHD is identical to the reformulation done by Rørvik et al. (2018). The CHD model is also parametrized and described as functions of RBE_{min} and RBE_{max}.

In summary, CHE, CHD, MAI, ROR, TIL, WED and WIL all assume RBE_{min} equals 1, whereas CAR, JON, MCN and PLR assumes that RBE_{min} varies. All models with the exception of CHE, UNK and WIL are tissue-dependent. Of the eleven phenomenological models, all models with the exception of CHE, ROR and PLR assume a linear relationship of RBE as a function of LET_d. The models are listed alphabetically.

CAR:

$$\mathrm{RBE_{max}}(\mathrm{LET_d}, (\alpha/\beta)_x) = 0.843 + 0.154\,\frac{2.686\ \mathrm{Gy(keV\ \mu m)^{-1}}}{(\alpha/\beta)_x}\,\mathrm{LET_d} \tag{A.1}$$

$$\mathrm{RBE_{min}}(\mathrm{LET_d}, (\alpha/\beta)_x) = 1.09 + 0.006\,\frac{2.686\ \mathrm{Gy(keV\ \mu m)^{-1}}}{(\alpha/\beta)_x}\,\mathrm{LET_d} \tag{A.2}$$

CHD:

The CHD model is made of two separate fits into two different cell lines. We used both fits in this thesis. The U87 cell line has an approximate $(\alpha/\beta)_x$ of 1.83 Gy, and the equation is shown below:

$$\mathrm{RBE_{max}} = \alpha_x + \frac{0.0451(\mathrm{keV\ \mu m})^{-1}}{\alpha_x}\,\mathrm{LET_d} \tag{A.3}$$

$$\mathrm{RBE_{min}} = 1$$

The AG01522 cell line has an approximate $(\alpha/\beta)_x$ of 8.73 Gy, and the equation for this fit is shown below:

$$\mathrm{RBE_{max}} = \alpha_x + \frac{0.00127(\mathrm{keV\ \mu m})^{-1}}{\alpha_x}\,\mathrm{LET_d} \tag{A.4}$$

$$\mathrm{RBE_{min}} = 1$$

CHE:

The CHE model is not tissue-dependent. We used an $(\alpha/\beta)_x$ of 3.33. The equation used is presented below:

$$\mathrm{RBE_{max}}(\mathrm{LET_d}) = 1 + \frac{1-\mathrm{e}^{-0.0013\ (\mathrm{keV\ \mu m})^{-2}\mathrm{LET_d^2}}}{0.045\ (\mathrm{keV\ \mu m})^{-1}\mathrm{LET_d}} \quad \text{(A.5)}$$

$$\mathrm{RBE_{min}} = 1$$

FRE:

The FRE model is tissue dependent on $\alpha_{x,}$ as seen in the equation below:

$$\mathrm{RBE_{max}}(\mathrm{LET_d}, \alpha_x) = 1 + \frac{0.008\ \mathrm{Gy\ (keV\ \mu m)^{-3}}}{\alpha_x}(\mathrm{LET_d} - 0.5\ \mathrm{keV\ \mu m^{-1}}), \quad \text{(A.6)}$$

$$\mathrm{RBE_{min}} = 1$$

JON:

The JON model is tissue dependent on α_x and β_x. The equations used is shown below:

$$\mathrm{RBE_{max}}(\mathrm{LET_d}, \alpha_x) = 1 + \frac{\mathrm{LET_d} - 0.22\ (\mathrm{keV\ \mu m^{-1}})}{30.28\ \mathrm{keV\ \mu m^{-1}}}\mathrm{LET_d}(\frac{a_u}{a_x} - 1) \quad \text{(A.7)}$$

$$\mathrm{RBE_{min}}(\mathrm{LET_d}, \beta_x) = \sqrt{1 + \frac{\mathrm{LET_d} - 0.22\ (\mathrm{keV\ \mu m^{-1}})}{30.28\ \mathrm{keV\ \mu m^{-1}}}\mathrm{LET_d}(\frac{\beta_u}{a_x} - 1)}, \quad \text{(A.8)}$$

Where $\alpha_u = 2.696\ \mathrm{Gy^{-1}}$ x $(1 - \mathrm{e_x^{-3.92Gy^{-1}a_x}})$ and $\beta_u = 0.06\ \mathrm{Gy^{-2}}$ x $(1 - \mathrm{e^{-50Gy^{-2}\beta_x}})$

MAI:

$$\mathrm{RBE_{max}}(\mathrm{LET_d}, (\alpha/\beta)_x) = 1 + \frac{0.377\ \mathrm{Gy}}{(\alpha/\beta)_x}\mathrm{LET_d} \quad \text{(A.9)}$$

$$\mathrm{RBE_{min}} = 1$$

MCN:

$$\mathrm{RBE_{max}}(\mathrm{LET_d}, (\alpha/\beta)_x) = 0.99064 + \frac{0.35605\ \mathrm{Gy\ (keV\ \mu m)^{-1}}}{(\alpha/\beta)_x}\mathrm{LET_d} \quad \text{(A.10)}$$

$$\mathrm{RBE_{min}}(\mathrm{LET_d}, (\alpha/\beta)_x) = 1.1012 - 0.0038703\ \mathrm{Gy^{-\frac{1}{2}}(keV\ \mu m)^{-1}}\sqrt{(\alpha/\beta)_x}\,\mathrm{LET_d} \quad \text{(A.11)}$$

PLR:

$$\mathrm{RBE_{max}}(\mathrm{LET_d}, (\alpha/\beta)_x) = 0.75 + \frac{0.00143\ \mathrm{Gy\ (keV\ \mu m)^{-3}}}{(\alpha/\beta)_x}\mathrm{LET_d^3} \quad \text{(A.12)}$$

$$\mathrm{RBE_{min}}(\mathrm{LET_d}, (\alpha/\beta)_x) = 1.24 + 0.00074\ \mathrm{Gy^{-1}\ (keV\ \mu m)^{-3}}\ (\alpha/\beta)_x\ \mathrm{LET_d^3} \quad \text{(A.13)}$$

ROR:

Rørvik et al. developed two variable RBE models, using different statistical weighting for the two suggested models. The RORW model uses a quadratic weighted fit, whereas RORUW is based on a linear unweighted fit.

Weighted:

$$\mathrm{RBE_{max}}(\mathrm{d(L)}, (\alpha/\beta)_x) = \int_0^\infty \mathrm{r_{max}}(\mathrm{L}, (\alpha/\beta)_x)\, \mathrm{d(L)}\, \mathrm{dL} \tag{A.14}$$

Where

$$\mathrm{r_{max}}(\mathrm{L}, (\alpha/\beta)_x) = \begin{cases} 1 + \frac{\mathrm{Gy}}{(\alpha/\beta)_x} \left(0.578\ (\mathrm{keV\ \mu m})^{-1}\mathrm{L} - 0.0808\ (\mathrm{keV\ \mu m})^{-2}\mathrm{L}^2 + \right. \\ \left. 0.00564 \left(\frac{\mathrm{keV}}{\mu\mathrm{m}}\right)^{-3} \mathrm{L}^3 - 9.92\ \mathrm{x}\ 10^{-5} (\mathrm{keV\ \mu m})^4 \mathrm{L}^4\right) & \mathrm{L} < 37.0\ \mathrm{keV\ \mu m^{-1}}, \\ 1 + \frac{10.5\ \mathrm{Gy}}{(\alpha/\beta)_x}, & \mathrm{L} \geq 37.0\ \mathrm{keV\ m^{-1}}, \end{cases} \tag{A.15}$$

$$\mathrm{RBE_{min}} = 1$$

Unweighted:

$$\mathrm{RBE_{max}}(\mathrm{LET_d}, (\alpha/\beta)_x) = 1 + \frac{0.645\ \mathrm{Gy\ (keV\ \mu m)^{-1}}}{(\alpha/\beta)_x} \mathrm{LET_d} \tag{A.16}$$

$$\mathrm{RBE_{min}} = 1$$

TIL:

The Tilly model consists of two different fits that correspond to low and high $(\alpha/\beta)_x$. The equation used in this thesis is the fit to low $(\alpha/\beta)_x$, which is presented below;

$$\mathrm{RBE_{max}}(\mathrm{LET_d}) = 1 + \frac{0.309\ \mathrm{Gy\ (keV\ \mu m)^{-1}}}{(\alpha/\beta)_x} \mathrm{LET_d} \tag{A.17}$$

$$\mathrm{RBE_{min}} = 1$$

UNK:

The model by Unkelbach et al. is mainly a model for LET optimization, and is thereby not fitted to in vitro data. The equation for the UNK model is shown below:

$$\mathrm{RBE_{min}} = \mathrm{RBE_{max}} = 1 + 0.04\ (\mathrm{keV\ \mu m})^{-1} \mathrm{LET_d} \tag{A.18}$$

WIL:

As seen in the equation below, the WIL model is not tissue-dependent. We applied an $(\alpha/\beta)_x$ of 3.76 Gy.

$$\mathrm{RBE}_{\max}(\mathrm{LET}_\mathrm{d}) = 0.892 + 0.179\ (\mathrm{keV\ \mu m})^{-1}\ \mathrm{LET}_\mathrm{d} \qquad \text{(A.19)}$$

$$\mathrm{RBE}_{\min} = 1$$

WED:

$$\mathrm{RBE}_{\max}(\mathrm{LET}_\mathrm{d}, (\alpha/\beta)_\mathrm{x}) = 1 + \frac{0.434\ \mathrm{Gy\ (keV\ \mu m)^{-1}}}{(\alpha/\beta)_\mathrm{x}}\mathrm{LET}_\mathrm{d} \qquad \text{(A.20)}$$

$$\mathrm{RBE}_{\min} = 1$$

Appendix B

Discrete RBE_d values across all variable models for the different subgroups are presented in Table B.1 - B.3. Table B.4 shows the median value and corresponding range to each BSC across the selected set of models.

Table B.1 Discrete RBE_d values for the temporal lobe substructures across all variable RBE models. The models are shown in the column to the far left. The numbers following each model name indicate the input parameter of $(\alpha/\beta)_x$. Abbreviations: Amyg = Amygdala, Hippo = Hippocampus, L = left, R = right, Ent. Cor. = Entorhinal Cortex

Model	Structures					
	Amyg. L	**Amyg. R**	**Ent. Cor. L**	**Ent. Cor. R**	**Hippo L**	**Hippo R**
CAR 2	1.27	1.19	1.25	1.23	1.29	1.25
CAR 3	1.21	1.13	1.18	1.17	1.21	1.17
CHD 1.83	1.14	1.10	1.13	1.12	1.17	1.15
CHD 8.73	1.21	1.14	1.19	1.17	1.21	1.18
CHE 3.33	1.46	1.32	1.43	1.40	1.52	1.46
FRE 2	1.09	1.06	1.08	1.08	1.10	1.09
FRE 3	1.08	1.05	1.07	1.06	1.08	1.07
JON 2	1.30	1.20	1.28	1.26	1.35	1.31
JON 3	1.34	1.23	1.31	1.29	1.38	1.34
MAI 2	1.25	1.18	1.24	1.22	1.30	1.27
MAI 3	1.31	1.22	1.29	1.27	1.35	1.32
MCN 2	1.27	1.20	1.25	1.24	1.30	1.27
MCN 3	1.23	1.17	1.21	1.20	1.24	1.22
PLR 2	1.08	1.07	1.06	1.06	1.03	1.01
PLR 3	1.03	1.02	1.01	1.01	0.98	0.96
RORW 2	1.23	1.17	1.22	1.21	1.27	1.25
RORW 3	1.19	1.14	1.18	1.17	1.22	1.20
RORUW 2	1.39	1.27	1.37	1.34	1.46	1.42
RORUW 3	1.34	1.23	1.31	1.29	1.38	1.34
TIL 2	1.25	1.15	1.23	1.21	1.28	1.23
TIL 3	1.23	1.14	1.21	1.20	1.26	1.21
UNK	1.14	1.09	1.12	1.11	1.13	1.11
WED 2	1.27	1.19	1.25	1.24	1.32	1.29
WED 3	1.23	1.16	1.21	1.20	1.26	1.23
WIL 3.76	1.27	1.16	1.24	1.21	1.29	1.24

Table B.2 Discrete RBE_d values for the ventricular substructures across all variable RBE models. The models are shown in the column to the far left. The numbers following each model name indicate the input parameter of $(\alpha/\beta)_x$. Abbreviations: Cing = Cingulum, Corp. = Corpus, L = left, R = right, SVZ = Subventricular zone

Model	RBE_d					
	Cing. L	**Cing. R**	**Corp. Col.**	**Fornix**	**SVZL**	**SVZR**
CAR 2	1.15	1.15	1.14	1.22	1.15	1.15
CAR 3	1.09	1.09	1.07	1.15	1.08	1.09
CHD 1.83	1.10	1.10	1.10	1.13	1.10	1.10
CHD 8.73	1.12	1.12	1.11	1.17	1.12	1.12
CHE 3.33	1.31	1.31	1.30	1.40	1.31	1.31
FRE 2	1.05	1.05	1.05	1.08	1.05	1.05
FRE 3	1.04	1.04	1.04	1.06	1.04	1.04
JON 2	1.20	1.20	1.19	1.26	1.20	1.20
JON 3	1.21	1.21	1.20	1.29	1.21	1.21
MAI 2	1.20	1.20	1.20	1.24	1.20	1.20
MAI 3	1.22	1.22	1.22	1.28	1.22	1.22
MCN 2	1.19	1.20	1.19	1.24	1.19	1.19
MCN 3	1.15	1.15	1.15	1.20	1.15	1.15
PLR 2	0.99	0.98	0.97	1.03	0.98	0.99
PLR 3	0.94	0.94	0.92	0.98	0.93	0.94
RORW 2	1.19	1.19	1.19	1.22	1.19	1.18
RORW 3	1.15	1.15	1.15	1.18	1.15	1.15
RORUW 2	1.28	1.29	1.28	1.35	1.28	1.28
RORUW 3	1.23	1.23	1.22	1.29	1.22	1.22
TIL 2	1.14	1.14	1.13	1.18	1.13	1.13
TIL 3	1.12	1.12	1.12	1.7	1.11	1.12
UNK	1.07	1.07	1.06	1.11	1.07	1.07
WED 2	1.19	1.20	1.19	1.24	1.19	1.19
WED 3	1.15	1.16	1.15	1.20	1.15	1.15
WIL 3.76	1.13	1.13	1.12	1.21	1.13	1.13

Table B.3 Discrete RBE_d values for the supratentorial substructures across all variable RBE models. The models are shown in the column to the far left. The numbers following each model name indicate the input parameter of $(\alpha/\beta)_x$. Abbreviations: Front. = Frontal, Par. = Parietal, Thal. = Thalamus, L = left, R = right

Model	RBE_d						
	Front. L	**Front. R**	**LFWM**	**Par. L**	**Par. R**	**Thal. L**	**Thal. R**
CAR 2	1.16	1.13	1.17	1.09	1.10	1.20	1.19
CAR 3	1.09	1.06	1.08	1.01	1.02	1.13	1.12
CHD 1.83	1.12	1.10	1.16	1.10	1.12	1.12	1.12
CHD 8.73	1.13	1.11	1.13	1.09	1.09	1.15	1.15
CHE 3.33	1.35	1.31	1.42	1.28	1.31	1.38	1.37
FRE 2	1.06	1.05	1.08	1.04	1.05	1.07	1.07
FRE 3	1.05	1.04	1.05	1.03	1.03	1.06	1.05
JON 2	1.23	1.20	1.30	1.19	1.21	1.25	1.24
JON 3	1.24	1.21	1.29	1.18	1.20	1.27	1.26
MAI 2	1.24	1.21	1.31	1.22	1.24	1.23	1.22
MAI 3	1.26	1.23	1.31	1.22	1.24	1.27	1.26
MCN 2	1.21	1.19	1.25	1.17	1.19	1.23	1.22
MCN 3	1.16	1.14	1.17	1.12	1.13	1.18	1.18
PLR 2	0.94	0.93	0.85	0.86	0.84	1.00	1.01
PLR 3	0.90	0.89	0.82	0.83	0.81	0.95	0.96
RORW 2	1.22	1.19	1.28	1.20	1.22	1.22	1.21
RORW 3	1.17	1.15	1.20	1.15	1.16	1.18	1.17
RORUW 2	1.33	1.29	1.43	1.29	1.32	1.35	1.33
RORUW 3	1.26	1.22	1.31	1.21	1.23	1.28	1.27
TIL 2	1.17	1.11	1.20	1.12	1.12	1.21	1.18
TIL 3	1.15	1.10	1.18	1.1	1.10	1.19	1.15
UNK	1.08	1.06	1.07	1.05	1.05	1.09	1.09
WED 2	1.23	1.20	1.29	1.20	1.22	1.24	1.23
WED 3	1.18	1.15	1.21	1.14	1.15	1.19	1.18
WIL 3.76	1.15	1.12	1.17	1.09	1.10	1.18	1.18

Table B.4 Median RBE_d values (range in brackets) across the three selected variable RBE models (JON, MCN, RORW) for all analyzed BSCs. Both input parameters of $(\alpha/\beta)_x$ are included. Abbreviations: L = left, R = right, Ent. Cor. = Entorhinal Cortex, Hippo = Hippocampus, LFWM = Left frontal white matter, SVZ = Subventricular zone

Structure	RBE_d Median [range]		
	JON	MCN	RORW
Amygdala L	1.34 [1.27. 1.47]	1.26 [1.21. 1.35]	1.23 [1.18. 1.32]
Amygdala R	1.33 [1.20. 1.44]	1.26 [1.17. 1.33]	1.22 [1.14. 1.29]
Cerebellum	2.19 [1.73. 2.61]	1.71 [1.42. 2.17]	1.66 [1.39. 2.06]
Cingulum L	1.24 [1.16. 1.44]	1.20 [1.13. 1.30]	1.19 [1.13. 1.30]
Cingulum R	1.23 [1.16. 1.37]	1.19 [1.12. 1.28]	1.19 [1.13. 1.28]
Circuit of Papez	1.32 [1.27. 1.41]	1.25 [1.20. 1.32]	1.22 [1.18. 1.28]
Corpus Callosum	1.20 [1.15. 1.37]	1.17 [1.12. 1.23]	1.17 [1.12. 1.22]
Ent. Cor. L	1.34 [1.28. 1.41]	1.25 [1.21. 1.34]	1.23 [1.18. 1.30]
Ent. Cor. R	1.33 [1.24. 1.27]	1.24 [1.19. 1.339	1.21 [1.12. 1.29]
Fornix	1.22 [1.17. 1.44]	1.19 [1.15. 1.24]	1.17 [1.13. 1.22]
Frontal Lobe	1.21 [1.18. 1.44]	1.17 [1.13. 1.21]	1.17 [1.14. 1.22]
Frontal Lobe	1.21 [1.18. 1.29]	1.17 [1.13. 1.22]	1.17 [1.14. 1.21]
Hippo Head L	1.43 [1.32. 1.24]	1.30 [1.22. 1.45]	1.28 [1.21. 1.42]
Hippo Head R	1.40 [1.27. 1.25]	1.27 [1.19. 1.43]	1.25 [1.18. 1.41]
Hippo L	1.47 [1.31. 1.61]	1.31 [1.21. 1.51]	1.30 [1.20. 1.48]
Hippo R	1.36 [1.28. 1.57]	1.28 [1.19. 1.43]	1.26 [1.19. 1.42]
Hippo Tail L	1.53 [1.27. 2.17]	1.35 [1.17. 1.86]	1.34 [1.19. 1.80]
Hippo Tail R	1.46 [1.23. 1.90]	1.30 [1.15. 1.67]	1.32 [1.17. 1.64]
LFWM	1.37 [1.21. 2.33]	1.26 [1.14. 1.95]	1.30 [1.16. 1.90]
Parietal Lobe L	1.20 [1.15. 1.27]	1.15 [1.11. 1.22]	1.18 [1.13. 1.26]
Parietal Lobe R	1.19 [1.15. 1.49]	1.16 [1.11. 1.38]	1.18 [1.13. 1.40]
SVZL	1.21 [1.15. 1.26]	1.17 [1.12. 1.23]	1.16 [1.13. 1.21]
SVZR	1.21 [1.15. 1.27]	1.18 [1.12. 1.23]	1.17 [1.12. 1.21]
Temporal Lobe L	1.33 [1.27. 1.45]	1.25 [1.19. 1.35]	1.24 [1.18. 1.33]
Temporal Lobe R	1.32 [1.23. 1.41]	1.24 [1.17. 1.30]	1.23 [1.16. 1.29]
Thalamus L	1.27 [1.21. 1.31]	1.21 [1.16. 1.25]	1.19 [1.15. 1.25]
Thalamus R	1.25 [1.20. 1.31]	1.20 [1.26. 1.26]	1.18 [1.14. 1.25]

Appendix C

Median (range in brackets) across all patients of %V10Gy (Table C.1) and %V40Gy (Table C.2) for all BSCs for the selected set of models and RBE 1.1.

Table C.1 Median (range in brackets) values for %V10Gy(RBE) for the three selected models and RBE 1.1. Both input parameters of $(\alpha/\beta)_x$ are included. Abbreviations: L = left, R = right, Ent. Cor. = Entorhinal Cortex, Hippo = Hippocampus, LFWM = Left frontal white matter, SVZ = Subventricular zone

Structure	%V10 Gy (RBE) Median [range] [%]			
	RBE 1.1	**JON**	**MCN**	**RORW**
Amygdala L	100 [100, 100]	100 [100, 100]	100 [100, 100]	100 [100, 100]
Amygdala R	100 [100, 100]	100 [100, 100]	100 [100, 100]	100 [100, 100]
Cerebellum	0 [0, 4]	1 [0, 6]	0 [0, 5]	0 [0, 5]
Cingulum L	35 [13, 67]	38 [14, 67]	37 [13, 67]	37 [13, 67]
Cingulum R	35 [14, 77]	38 [16, 77]	37 [15, 77]	37 [15, 77]
Circuit of Papez	64 [58, 78]	66 [61, 80]	66 [60, 79]	65 [60, 79]
Corpus Callosum	55 [36, 90]	58 [40, 90]	56 [38, 90]	57 [38, 91]
Ent. Cor. L	100 [88, 100]	100 [92, 100]	100 [91, 100]	100 [91, 100]
Ent. Cor. R	100 [97, 100]	100 [99, 100]	100 [98, 100]	100 [98, 100]
Fornix	86 [51, 100]	87 [54, 100]	87 [52, 100]	87 [50, 100]
Frontal Lobe	22 [17, 38]	24 [18, 40]	23 [18, 40]	24 [17, 41]
Frontal Lobe	21 [16, 38]	22 [17, 41]	21 [16, 41]	22 [16, 41]
Hippo Head L	82 [10, 100]	90 [19, 100]	88 [14, 100]	88 [14, 100]
Hippo Head R	91 [58, 100]	100 [74, 100]	99 [67, 100]	99 [67, 100]
Hippo L	42 [17, 61]	47 [24, 62]	46 [21, 62]	46 [21, 62]
Hippo R	47 [18, 68]	55 [24, 76]	53 [21, 74]	53 [21, 74]
Hippo Tail L	6 [0, 28]	10 [0, 37]	8 [0, 35]	8 [0, 35]
Hippo Tail R	17 [0, 31]	26 [0, 50]	24 [0, 45]	24 [0, 44]
LFWM	0 [0, 11]	0 [0, 13]	0 [0, 12]	0 [0, 13]
Parietal Lobe L	3 [0, 13]	3 [0, 14]	3 [0, 14]	3 [0, 15]
Parietal Lobe R	4 [0, 16]	4 [0, 17]	4 [0, 17]	4 [0, 17]
SVZL	49 [42, 70]	51 [44, 75]	51 [43, 74]	51 [43, 75]
SVZR	56 [31, 69]	57 [34, 71]	56 [32, 71]	57 [33, 71]
Temporal Lobe L	26 [15, 47]	29 [18, 49]	28 [16, 49]	28 [16, 49]
Temporal Lobe R	26 [23, 49]	30 [26, 51]	29 [24, 50]	29 [25, 51]
Thalamus L	76 [37, 100]	79 [42, 100]	78 [39, 100]	78 [36, 100]
Thalamus R	87 [42, 100]	91 [47, 100]	90 [44, 100]	90 [41, 100]

Table C.2 Median (range in brackets) values for %V40Gy(RBE) for the three selected models and RBE 1.1. Both input parameters of $(\alpha/\beta)_x$ are included. Abbreviations: L = left, R = right, Ent. Cor. = Entorhinal Cortex, Hippo = Hippocampus, LFWM = Left frontal white matter, SVZ = Subventricular zone

Structure	%V40 Gy (RBE) Median [range] [%]			
	RBE 1.1	**JON**	**MCN**	**RORW**
Amygdala L	60 [22, 98]	88 [46, 100]	79 [37, 100]	76 [35, 100]
Amygdala R	67 [32, 100]	90 [58, 100]	81 [48, 100]	78 [45, 100]
Cerebellum	0 [0, 0]	0 [0, 1]	0 [0, 1]	0 [0, 1]
Cingulum L	1 [0, 9]	3 [0, 10]	3 [0, 10]	3 [0, 10]
Cingulum R	0 [0, 13]	0 [0, 15]	0 [0, 14]	0 [0, 14]
Circuit of Papez	35 [17, 48]	41 [24, 54]	38 [21, 52]	38 [20, 52]
Corpus Callosum	0 [0, 13]	2 [0, 18]	1 [0, 17]	1 [0, 16]
Ent. Cor. L	75 [41, 97]	89 [57, 100]	84 [51, 100]	83 [49, 99]
Ent. Cor. R	75 [51, 94]	86 [71, 98]	83 [63, 97]	82 [61, 97]
Fornix	61 [27, 100]	61 [27, 100]	58 [26, 100]	55 [25, 99]
Frontal Lobe	2 [1, 5]	2 [1, 6]	2 [1, 5]	2 [1, 5]
Frontal Lobe	2 [1, 7]	3 [1, 9]	3 [1, 8]	3 [1, 8]
Hippo Head L	11 [0, 52]	25 [0, 82]	18 [0, 74]	17 [0, 72]
Hippo Head R	9 [0, 51]	23 [0, 69]	17 [0, 64]	16 [0, 62]
Hippo L	3 [0, 20]	9 [0, 32]	7 [0, 29]	6 [0, 28]
Hippo R	4 [0, 29]	9 [0, 39]	7 [0, 36]	7 [0, 35]
Hippo Tail L	0 [0, 0]	0 [0, 4]	0 [0, 2]	0 [0, 2]
Hippo Tail R	0 [0, 0]	0 [0, 2]	0 [0, 1]	0 [0, 1]
LFWM	0 [0, 0]	0 [0, 0]	0 [0, 0]	0 [0, 0]
Parietal Lobe L	0 [0, 0]	0 [0, 0]	0 [0, 0]	0 [0, 0]
Parietal Lobe R	0 [0, 0]	0 [0, 0]	0 [0, 0]	0 [0, 0]
SVZL	4 [0, 19]	7 [0, 25]	6 [0, 23]	6 [0, 22]
SVZR	3 [0, 33]	5 [0, 38]	5 [0, 37]	4 [0, 37]
Temporal Lobe L	4 [2, 9]	6 [4, 12]	5 [3, 11]	5 [3, 11]
Temporal Lobe R	5 [3, 9]	7 [4, 12]	6 [4, 12]	6 [4, 11]
Thalamus L	34 [0, 81]	41 [2, 92]	39 [1, 90]	38 [1, 89]
Thalamus R	39 [1, 86]	47 [2, 96]	45 [1, 94]	44 [1, 93]

Appendix D

Discrete IQ change scores obtained by Equation (6.2 – 6.10) are shown in Table D.1 – D.9. The calculated p-value (RBE 1.1 compared with each variable RBE model) is shown in the lowest row. If the variable RBE model systematically resulted in higher or lower values across all patients, the calculated p-value was 0.005. For all tables in Appendix D, the patient number is shown in the column to the far left.

Table D.10 presents discrete values of the change in delayed verbal memory score (Eq. 6.13), whereas table D.11 presents discrete values for the risk of memory impairment obtained by Eq. 6.14.

Table D.1 This table presents the IQ score change values obtained from Eq. (6.2). The equation estimates the change in IQ score based on the dose/volume intervals for the brain. The patient number is shown in the column to the far left. The p-values are shown in the row at the bottom.

#	IQ score change Brain						
	RBE 1.1	**JON**		**MCN**		**RORW**	
		Input parameter of $(\alpha/\beta)_x$					
		2	3	2	3	2	3
1	-8.9	-8.5	-7.8	-8.5	-9.3	-8.9	-9.2
2	-9.5	-8.8	-8.2	-9.1	-9.7	-9.6	-9.7
3	-8.1	-7.0	-7.2	-7.2	-7.9	-7.6	-8.2
4	-9.5	-8.6	-8.3	-8.9	-9.5	-9.4	-9.6
5	-8.8	-8.2	-7.7	-8.4	-9.1	-8.9	-9.0
6	-9.5	-9.3	-8.7	-9.4	-9.8	-9.7	-9.7
7	-9.1	-8.5	-8.1	-8.6	-9.3	-9.1	-9.3
8	-9.5	-9.1	-8.7	-9.3	-9.7	-9.7	-9.7
9	-9.4	-9.1	-8.9	-9.2	-9.5	-9.5	-9.5
10	-9.5	-9.2	-8.3	-9.5	-10.0	-9.9	-9.9
p-value		0.005	0.005	0.005	0.005	0.139	0.005

Table D.2 This table presents the IQ score change values obtained from Eq. (6.3). The equation estimates the change in IQ score based on the dose/volume intervals for the supratentorial brain. The patient number is shown in the column to the far left. The p-values are shown in the row at the bottom.

#	IQ score change Supratentorial brain						
	RBE 1.1	**JON**		**MCN**		**RORW**	
		Input parameter of $(\alpha/\beta)_x$					
		2	3	2	3	2	3
1	-9.0	-8.6	-7.9	-8.8	-9.4	-9.3	-9.3
2	-8.8	-8.1	-7.5	-8.4	-9.0	-8.9	-9.0
3	-8.5	-7.5	-7.7	-7.7	-8.3	-8.1	-8.6
4	-8.9	-7.9	-7.7	-8.2	-8.9	-8.9	-9.1
5	-8.2	-7.8	-7.3	-8.0	-8.5	-8.4	-8.5
6	-8.9	-8.7	-8.0	-8.9	-9.3	-9.2	-9.1
7	-8.7	-7.9	-7.6	-8.1	-8.8	-8.7	-8.9
8	-8.5	-8.4	-8.0	-8.5	-8.8	-8.7	-8.7
9	-8.9	-8.5	-8.2	-8.6	-9.1	-9.0	-9.0
10	-9.2	-8.9	-7.7	-9.1	-9.8	-9.7	-9.7
p-value		0.005	0.005	0.005	0.005	0.09	0.005

Table D.3 This table presents the IQ score change values obtained from Eq. (6.4). The equation estimates the change in IQ score based on the dose/volume intervals for the left temporal lobe. The patient number is shown in the column to the far left. The p-values are shown in the row at the bottom.

#	IQ score change Left temporal lobe						
	RBE 1.1	**JON**		**MCN**		**RORW**	
		Input parameter of $(\alpha/\beta)_x$					
		2	3	2	3	2	3
1	-9.3	-9.1	-9.0	-9.2	-9.4	-9.4	-9.4
2	-9.3	-9.0	-8.9	-9.1	-9.2	-9.2	-9.3
3	-9.5	-8.8	-8.8	-8.9	-9.3	-9.2	-9.6
4	-9.0	-8.7	-8.6	-8.9	-9.1	-9.1	-9.2
5	-9.0	-8.3	-8.1	-8.6	-9.4	-9.3	-9.3
6	-9.1	-8.6	-8.5	-8.8	-9.3	-9.2	-9.2
7	-8.9	-8.7	-8.7	-8.8	-9.0	-9.0	-9.0
8	-9.2	-8.9	-8.7	-9.0	-9.3	-9.2	-9.2
9	-8.9	-8.7	-8.6	-8.8	-9.0	-8.9	-9.0
10	-8.8	-8.6	-8.3	-8.9	-9.2	-9.1	-9.1
p-value		0.005	0.005	0.005	0.005	0.31	0.005

Table D.4 This table presents the IQ score change values obtained from Eq. (6.5). The equation estimates the change in IQ score based on the dose/volume intervals for the brain. The patient number is shown in the column to the far left. The p-values are shown in the row at the bottom.

#	IQ score change Brain						
	RBE 1.1	**JON**		**MCN**		**RORW**	
		Input parameter of $(\alpha/\beta)_x$					
		2	3	2	3	2	3
1	-1.9	-2.0	-2.0	-2.0	-1.9	-2.0	-2.0
2	-1.0	-1.2	-1.2	-1.2	-1.1	-1.2	-1.1
3	-1.1	-1.1	-1.2	-1.2	-1.1	-1.2	-1.1
4	-0.9	-1.1	-1.0	-1.0	-1.0	-1.1	-1.0
5	-1.4	-1.5	-1.5	-1.5	-1.4	-1.5	-1.4
6	-0.9	-1.0	-1.0	-1.0	-1.0	-1.0	-1.0
7	-1.2	-1.3	-1.3	-1.3	-1.2	-1.3	-1.2
8	-0.8	-0.9	-0.9	-0.9	-0.9	-0.9	-0.9
9	-0.7	-0.8	-0.8	-0.8	-0.7	-0.8	-0.7
10	-1.5	-1.6	-1.6	-1.6	-1.5	-1.6	-1.6
p-value		0.005	0.005	0.005	0.005	0.005	0.005

Table D.5 This table presents the IQ score change values obtained from Eq. (6.6). The equation estimates the change in IQ score based on the dose/volume intervals for the supratentorial brain. The patient number is shown in the column to the far left. The p-values are shown in the row at the bottom.

#	IQ score change Supratentorial brain						
	RBE 1.1	**JON**		**MCN**		**RORW**	
		Input parameter of $(\alpha/\beta)_x$					
		2	3	2	3	2	3
1	-1.8	-3.3	-3.4	-3.3	-3.1	-3.2	-2.9
2	-0.9	-1.9	-1.9	-1.8	-1.7	-1.8	-1.6
3	-0.9	-1.4	-1.5	-1.6	-1.5	-1.5	-1.4
4	-0.9	-1.6	-1.6	-1.6	-1.5	-1.6	-1.4
5	-1.1	-2.2	-2.2	-2.1	-2.0	-2.0	-1.8
6	-0.8	-1.7	-1.8	-1.7	-1.6	-1.6	-1.5
7	-1.0	-2.0	-2.0	-2.0	-1.8	-1.9	-1.7
8	-0.6	-1.2	-1.2	-1.1	-1.0	-1.1	-1.0
9	-0.6	-1.2	-1.2	-1.2	-1.1	-1.1	-1.0
10	-1.3	-3.0	-3.1	-2.9	-2.7	-2.8	-2.5
p-value		0.005	0.005	0.005	0.005	0.005	0.005

Table D.6 This table presents the IQ score change values obtained from Eq. (6.7). The equation estimates the change in IQ score based on the dose/volume intervals for the left temporal lobe. The patient number is shown in the column to the far left. The p-values are shown in the row at the bottom.

#	IQ score change Left temporal lobe						
	RBE 1.1	**JON**		**MCN**		**RORW**	
		Input parameter of $(\alpha/\beta)_x$					
		2	3	2	3	2	3
1	-0.9	-1.1	-1.1	-1.1	-1.0	-1.1	-1.0
2	-0.9	-1.1	-1.1	-1.1	-1.0	-1.1	-1.0
3	-1.5	-1.7	-1.8	-1.8	-1.7	-1.9	-1.7
4	-1.3	-1.6	-1.5	-1.5	-1.4	-1.5	-1.4
5	-2.6	-3.0	-3.0	-3.0	-2.8	-3.1	-2.9
6	-1.6	-1.9	-1.9	-1.9	-1.7	-2.0	-1.7
7	-1.6	-1.9	-1.9	-1.9	-1.8	-1.9	-1.8
8	-1.4	-1.7	-1.7	-1.6	-1.5	-1.7	-1.5
9	-1.1	-1.4	-1.4	-1.4	-1.3	-1.4	-1.3
10	-1.9	-2.2	-2.2	-2.2	-2.1	-2.2	-2.1
p-value		0.005	0.005	0.005	0.005	0.005	0.005

Table D.7 This table presents the IQ score change values obtained from Eq. (6.8). The equation estimates the change in IQ score based on the mean dose to the brain. The patient number is shown in the column to the far left. The p-values are shown in the row at the bottom.

#	IQ score change Brain						
	RBE 1.1	**JON**		**MCN**		**RORW**	
		Input parameter of $(\alpha/\beta)_x$					
		2	3	2	3	2	3
1	-2.3	-2.6	-2.6	-2.5	-2.4	-2.5	-2.4
2	-1.5	-1.7	-1.8	-1.7	-1.6	-1.7	-1.6
3	-1.3	-1.5	-1.5	-1.5	-1.4	-1.5	-1.4
4	-1.4	-1.6	-1.6	-1.6	-1.5	-1.6	-1.5
5	-1.8	-2.1	-2.1	-2.0	-2.0	-2.0	-1.9
6	-1.5	-1.7	-1.7	-1.6	-1.6	-1.6	-1.6
7	-1.6	-1.8	-1.8	-1.8	-1.7	-1.8	-1.7
8	-1.2	-1.4	-1.5	-1.4	-1.3	-1.4	-1.3
9	-1.1	-1.3	-1.3	-1.2	-1.2	-1.2	-1.2
10	-2.1	-2.3	-2.4	-2.3	-2.2	-2.3	-2.2
p-value		0.005	0.005	0.005	0.005	0.005	0.005

Table D.8 This table presents the IQ score change values obtained from Eq. (6.9). The equation estimates the change in IQ score based on the mean dose to the supratentorial brain. The patient number is shown in the column to the far left. The p-values are shown in the row at the bottom.

#	IQ score change Supratentorial brain						
	RBE 1.1	**JON**		**MCN**		**RORW**	
		Input parameter of $(\alpha/\beta)_x$					
		2	3	2	3	2	3
1	-2.3	-2.6	-2.6	-2.5	-2.4	-2.5	-2.4
2	-1.5	-1.7	-1.7	-1.7	-1.6	-1.7	-1.6
3	-1.3	-1.5	-1.4	-1.4	-1.4	-1.4	-1.4
4	-1.4	-1.6	-1.6	-1.6	-1.5	-1.6	-1.5
5	-1.8	-2.0	-2.0	-2.0	-1.9	-2.0	-1.9
6	-1.6	-1.8	-1.8	-1.7	-1.7	-1.7	-1.7
7	-1.6	-1.8	-1.8	-1.8	-1.7	-1.8	-1.7
8	-1.2	-1.3	-1.3	-1.3	-1.2	-1.3	-1.2
9	-1.2	-1.3	-1.3	-1.3	-1.2	-1.3	-1.2
10	-2.1	-2.4	-2.4	-2.4	-2.3	-2.3	-2.3
p-value		0.005	0.005	0.005	0.005	0.005	0.005

Table D.9 This table presents the IQ score change values obtained from Eq. (6.10). The equation estimates the change in IQ score based on the mean dose to the left temporal lobe. The patient number is shown in the column to the far left. The p-values are shown in the row at the bottom.

#	IQ score change Left temporal lobe						
	RBE 1.1	**JON**		**MCN**		**RORW**	
		Input parameter of $(\alpha/\beta)_x$					
		2	3	2	3	2	3
1	-0.9	-1.1	-1.1	-1.1	-1.0	-1.1	-1.0
2	-0.9	-1.1	-1.1	-1.1	-1.0	-1.1	-1.0
3	-1.5	-1.7	-1.8	-1.8	-1.7	-1.9	-1.7
4	-1.3	-1.6	-1.5	-1.5	-1.4	-1.5	-1.4
5	-2.6	-3.0	-3.0	-3.0	-2.8	-3.1	-2.9
6	-1.6	-1.9	-1.9	-1.9	-1.7	-2.0	-1.7
7	-1.6	-1.9	-1.9	-1.9	-1.8	-1.9	-1.8
8	-1.4	-1.7	-1.7	-1.6	-1.5	-1.7	-1.5
9	-1.1	-1.4	-1.4	-1.4	-1.3	-1.4	-1.3
10	-1.9	-2.2	-2.2	-2.2	-2.1	-2.2	-2.1
p-value		0.005	0.005	0.005	0.005	0.005	0.005

Table D.10 This table presents the estimated risk of memory impairment from Eq. (6.13). The patient number is shown in the column to the far left.

#	Risk of memory impairment						
	RBE 1.1	**JON**		**MCN**		**RORW**	
		Input parameter of $(\alpha/\beta)_x$					
		2	3	2	3	2	3
1	34 %	36 %	36 %	36 %	35 %	36 %	35 %
2	33 %	35 %	35 %	34 %	34 %	34 %	34 %
3	39 %	42 %	42 %	41 %	40 %	41 %	40 %
4	36 %	39 %	40 %	39 %	38 %	38 %	38 %
5	45 %	49 %	49 %	48 %	47 %	48 %	47 %
6	43 %	46 %	46 %	45 %	44 %	45 %	44 %
7	37 %	40 %	40 %	39 %	39 %	39 %	39 %
8	36 %	38 %	38 %	37 %	37 %	37 %	37 %
9	38 %	40 %	41 %	40 %	39 %	40 %	39 %
10	40 %	44 %	45 %	43 %	42 %	43 %	42 %

Table D.11 This table presents the estimated delayed verbal memory score from Eq. (6.14). The patient number is shown in the column to the far left.

#	Delayed verbal memory score						
	RBE 1.1	**JON**		**MCN**		**RORW**	
		Input parameter of $(\alpha/\beta)_x$					
		2	3	2	3	2	3
1	-0.62	-0.68	-0.68	-0.67	-0.66	-0.66	-0.65
2	-0.68	-0.76	-0.76	-0.74	-0.73	-0.74	-0.73
3	-0.86	-0.91	-0.91	-0.9	-0.88	-0.9	-0.89
4	-0.64	-0.7	-0.7	-0.68	-0.67	-0.68	-0.67
5	-0.97	-0.99	-0.99	-0.99	-0.98	-0.99	-0.98
6	-0.96	-1.02	-1.02	-1.01	-0.99	-1.01	-0.99
7	-0.58	-0.63	-0.63	-0.62	-0.6	-0.61	-0.6
8	-0.89	-0.97	-0.97	-0.95	-0.93	-0.95	-0.93
9	-0.71	-0.79	-0.79	-0.77	-0.76	-0.77	-0.75
10	-0.83	-0.93	-0.93	-0.91	-0.89	-0.9	-0.88